# Sources of Difference Frequency Sound in a Dual-Frequency Imaging System with Implications for Monitoring Thermal Surgery

by

Jonathan S. Thierman

S.B., Biomedical Engineering
Harvard University (1998)

M.S., Mechanical Engineering
Massachusetts Institute of Technology (2001)



SUBMITTED TO THE HARVARD-MIT DIVISION OF HEALTH SCIENCES AND TECHNOLOGY IN PARTIAL FULFILLMENT OF THE REQUIREMENTS FOR THE DEGREE OF

DOCTOR OF PHILOSOPHY IN MECHANICAL & MEDICAL ENGINEERING
AT THE
MASSACHUSETTS INSTITUTE OF TECHNOLOGY

SEPTEMBER 2004



Signature of Author_____
Harvard-MIT Division of Health Sciences and Technology
August 1, 2004

Certified by_____
Kullervo Hynynen, Ph.D.
Professor of Radiology, Brigham & Women's Hospital, Harvard Medical School
Research Head, Thesis Supervisor

Certified by_____
Nicholas Makris, Ph.D.
Professor of Ocean Engineering, Massachusetts Institute of Technology
Thesis Supervisor

Accepted by_____
Martha Gray, Ph.D.
Edward Hood Taplin Professor of Medical & Electrical Engineering, M.I.T.
Co-Director, Harvard-MIT Division of Health Sciences and Technology

# Sources of Difference Frequency Sound in a Dual-Frequency Imaging System with Implications for Monitoring Thermal Surgery

by

Jonathan S. Thierman

Submitted to the Harvard-MIT Division of Health Sciences and Technology on June 14th, 2004 in partial fulfillment of the requirements for the degree of

Doctor of Philosophy in Mechanical and Medical Engineering

at the

Massachusetts Institute of Technology

## Abstract

This thesis explores the nature of the ultrasound-stimulated vibro-acoustography (USVA) imaging method introduced by Fatemi and Greenleaf in 1998.[1] The USVA method relies upon the generation of a difference frequency signal from the interaction of two pressure fields with a target. A thorough understanding of USVA will be necessary to further advance this dual-frequency method. Prior studies demonstrate a correlation between difference frequency signal response and tissue temperature, and difference frequency signal response and tissue coagulation,[2,3] suggesting that USVA may be well suited for monitoring focused ultrasound surgery. This thesis explores three possible sources of the difference frequency signal: 1) the parametric effect, 2) linear reflection of the local difference frequency field, and 3) nonlinear interaction of linearly scattered waves. The research compares the relative significance of these three possible sources using mathematical analysis, computer simulations, and experimental results.

The results set forth in this thesis suggest that the parametric effect may be the most significant source of difference frequency signal, reaching pressures of 1-10 Pa and significantly overshadowing the other two enumerated effects. The second effect, the linear reflection of the local evanescent difference frequency field, is undetectable experimentally. Finally, the third effect, the nonlinear interaction of linearly scattered waves for a single bubble, contributes to the difference frequency signal only slightly, albeit detectably, reaching levels of .1-1 Pa. These results have a number of implications for future implementations of USVA. In order to utilize USVA as a successful imaging tool, one must take measures to avoid the signal from the parametric effect, which can be considered an imaging artifact. Additionally, it may be possible to use the nonlinear interaction of scattered waves to form images that rely on the presence of small

scatterers; a technique that may be enhanced with the use of contrast agents containing small scattering micro-bubbles *in vivo*. [4]

Thesis Supervisor: Kullervo Hynynen, Ph.D.
Professor of Radiology
Brigham & Women's Hospital, Harvard Medical School

Thesis Supervisor: Nicholas Makris, Ph.D.
Professor of Ocean Engineering
Massachusetts Institute of Technology

# Acknowledgements

I thank my thesis advisors, Drs. Kullervo Hynynen and Nicholas Makris, for their guidance, mentorship, and expertise over the years. Dr. Hynynen possesses an uncanny intuition for acoustics problems, experimental design, and medical ultrasound derived from his unparalleled experience in the field. He has taught me to be a scientist and an engineer. I am honored to have worked with, and learned from such a disciplined individual who has taught me the value of being ever a consummate professional. Dr. Makris commands an awe inspiring knowledge of linear and nonlinear acoustic theory and proposed many of the theoretical foundations for my graduate work. I am sincerely appreciative for his keen interest and relentless enthusiasm for my thesis project and my development. I will always fondly remember the many grueling, exhilarating, and even heated hours we spent discussing my doctorate work in his office at MIT. I thank him for the care and rigor with which he reviewed my written material. I also thank the chair of my thesis committee Dr. Fred Bowman. I am grateful for his advice, attitude, and support during the later phase of my thesis work.

I thank everyone in the Brigham & Women's Focused Ultrasound Laboratory as well as the MIT Ocean Engineering Group. They have been my greatest teachers and even better friends. In particular, I owe an enormous debt of gratitude to Dr. Greg Clement, Dr. Elisa Konofagou, Dr. Purnima Ratilal, Dr. Sham Sokka, and Sunwoong Lee for tutoring me in acoustics throughout the years and teaching me so much. Greg, Elisa, Sham, and Purnima have each contributed extensively to the experimental and theoretical development of my thesis. Their openness and patience with my questions was truly unparalleled. I also thank Dr. Nathan McDannold, Dr. Roger Brockett, Randy King, Jose Juste, Dr. Subha Maruvada, Jason White, Tonia Giesecke, Dr. Natalia Vykhodtseva, Christina Silcox, Dr. Chris Connor, Dr. Alex Zaitsev, Dr. Eric Osborn, Joel Sawady, and Lisa Treat for teaching me about so many things: professional, personal, and the eclectic. In addition, I greatly appreciate the help of Dr. Mark Ottensmeyer with building apparatus and using the silicone gel tissue phantoms.

I extend a special acknowledgement to Drs. Peter Westervelt and Harvey Woodsum with whom I was honored to engage in many thought-provoking discussions relating my current thesis work to their research from decades earlier. Their continued interest in the field and support for young researchers is greatly appreciated.

Finally, I would like to thank my sisters, Sara and Jessica, my parents, Mark and Ronnie, and my grandparents, Laura and Joe Beck and Corinne Thierman. They cultivated my curiosity from an early age and have encouraged me through their continued love and support. To my wife Melanie Glickson, who has seen me through almost my entire academic career to date, you are always there for me and inspire me not only to excel but also to love.

This work was supported by a Whitaker Foundation Fellowship and by NIH grant R21CA82275.

# Contents

# List of Figures

# List of Tables

# 1 Introduction

Focused Ultrasound Surgery (FUS) uses highly focused ultrasound radiation to cause thermal changes in tissue treatment volumes with little thermal effect in the near field. In this way, therapeutic ultrasound is proving to be an increasingly effective way to treat various cancers, as well as non-malignant pathologies in humans using coagulation necrosis[5] and hyperthermia[6]. In addition, studies have demonstrated that phased arrays may be effective as noninvasive surgical tools[7-11]. However, the real-time monitoring of the location and extent of tissue damage remains one of the greatest challenges in focused ultrasound treatment. Monitoring damaged tissue and temperature elevations during noninvasive procedures has traditionally been performed using Magnetic Resonance Imaging (MRI)[12-19]. However, difficulties with MRI monitoring of ultrasound therapy include the high cost and limited availability of MRI systems. Studies of other imaging techniques including diagnostic ultrasound[20,21] and CT imaging [22,23] demonstrate only marginal degrees of success at monitoring FUS. An ideal monitoring system would utilize the same transducer that applied the ultrasound therapy, thereby avoiding the large cost and limited availability of an MRI system.

Ultrasound-stimulated vibro-acoustography (USVA) refers to an imaging method proposed by M. Fatemi and J.F. Greenleaf[24,25] for use as a diagnostic imaging modality. Fatemi and Greenleaf theorize that intense ultrasound at two differing frequencies causes a local cyclical force, resulting in a mechanical tissue response that generates difference frequency sound. According to Fatemi and Greenleaf, "modulation of the energy density creates an oscillatory force, effectively vibrating the object at the selected region. The resulting vibration of the object produces an acoustic field that can be measured some distance away"[24]. Although the wavelength of the difference frequency sound generated may be many centimeters in length, Fatemi and Greenleaf's results suggest that the intersection of the two primary fields allows the acoustic energy incident on the imaging target to be localized to an area of much smaller dimension (millimeters). The wavelength of the primary frequency determines the dimension of the focused incident fields. Therefore, one unique feature of Fatemi and Greenleaf's dual-frequency method is the high spatial resolution obtained by the highly focused primary fields. In addition, the low-frequency response propagates with very little attenuation, resulting in the theoretical possibility of a high-resolution imaging method with high signal-to-noise ratio.

In prior studies, we tested the feasibility of the USVA system for monitoring thermal surgery. The studies demonstrated the correlation between difference frequency signal response and tissue temperature, and difference frequency signal response and tissue coagulation[2,26-29]. However, these results are difficult to reproduce and characterize in a quantitatively meaningful manner. In addition, as both we and Fatemi[30] observe, the difference frequency sound generation from the USVA system exhibits great sensitivity to the orientation of the target and the geometry of the experimental set-up. This suggests that the mechanisms involved in the generation of the difference frequency response may not be completely understood.

Understanding the physical mechanisms for the nonlinear production of difference frequency sound is a crucial first step in refining this imaging method and designing a more robust and clinically useful imaging system. This thesis explores three possible acoustic sources of the difference frequency signal: 1) the parametric effect, 2) linear reflection of the local difference frequency field, and 3) nonlinear interaction of linearly scattered waves. In addition, we present empirical measurements of tissue displacement and oscillatory forces that are not adequately explained by the three effects present in this thesis. Finally, we consider the generation of sound as a result of this tissue motion and determine the minimum displacements needed in order to produce a detectable signal.

## 1.1 Background

Fatemi and Greenleaf proposed the vibro-acoustography imaging technique as a method of "radiation force" based imaging.[31] Traditionally, the radiation force is defined as a static force proportional to the time average intensity of the acoustic field which results from the nonlinear action of a pressure wave with itself.[32] Several researchers have explored various radiation force techniques aimed at measuring material properties of biological tissues.[33-37] The relatively new field of radiation force imaging is of great interest because of known variances in tissue mechanical properties associated with malignancy and other pathologies.[38,39] Therefore, an imaging method that can distinguish between tissue mechanical moduli would be invaluable for diagnosis of malignancy where other imaging methods fail to distinguish healthy from pathological tissue. In addition, due to normal variations in mechanical stiffness of different tissue types, imaging tissue moduli may help differentiate between healthy tissues to provide a new means for general physiological imaging.[i]

[i] This field of radiation force imaging is closely related to another promising field of tissue elasticity imaging called elastography.

The USVA method has been used for localizing arterial plaques, imaging breast micro-calcifications, and measuring properties of solid targets like metal bars and struts by Fatemi and Greenleaf[24,40,41] and others[42-45]. We have demonstrated the use of this technique *ex vivo* to image lesions of coagulative necrosis caused by tissue ablation during thermal therapy and to measure temperature changes as tissue is heated by the application of focused ultrasound[2,3,26-29]. Despite these advances in the imaging technique there are still many difficulties with the dual-frequency system including sensitivity of the difference frequency response to target geometry and orientation. In order to better understand these findings, the origin of the difference frequency sound requires further investigation.

The study of the generation of difference frequency sound involves nonlinear acoustics because only through nonlinear mechanisms can waves at two frequencies combine to produce a wave at a third frequency not originally present as an input to the system. There is a rich body of literature filled with debate pertaining to the nonlinear generation of sum and difference frequency fields in acoustics[46-62]. The historic paper entitled "The Scattering of Sound by Sound" published in the Journal of the Acoustical Society of America in 1956 by Ingard and Pridmore-Brown sparked a controversy in the field of acoustics regarding the creation of scattered sound waves at the sum and difference frequency from the interaction of incident waves at a non-zero angle of propagation[63]. The theory of this type of nonlinear sound generation was clarified by Westervelt in his papers on the scattering of sound by sound[64] and the parametric array[65] which essentially explained that only if two fields are propagating in the same direction will they interact to produce sum and difference frequency waves which propagate. However, experimentalists reported measuring a sum frequency signal originating from the interaction of incident primary beams at a non-zero angle of propagation.[60,66] To this day there is some disagreement over these results as well as continued interest in the scattering of sound by sound[46,49,57,59-61,64,66-75]. Much of this history is outlined by Beyer[76] and also TenCate[66].

Theoretically, there are many mechanisms of nonlinear sound generation in acoustic regimes involving sources at multiple frequencies which may lead to the production of sum and difference frequencies. The controversy over experimental results in the literature arises in part from the plethora of possible sources of nonlinear sound, which exist simultaneously and are difficult to isolate experimentally. Several of the previously proposed sources of nonlinear sound in a dual-frequency system include nonlinear scattering from the interaction of two collimated fields in the medium [46], the nonlinear interaction of scattered waves from a target [52,77], parametric radiation in the incident field [42,47,65], and pseudo-sound effects at the hydrophone detector[47]. However, the only source of difference frequency considered by the authors of the vibro-acoustography imaging method is the "time varying" radiation force of the dual-frequency field on a target.

## 1.2 Scope of Thesis

This thesis explores three acoustical mechanisms which may contribute to the production of difference frequencies in a dual-frequency imaging system: 1) the parametric effect, 2) linear reflection of the local difference frequency field, and 3) nonlinear interaction of linearly scattered waves. Through mathematical analysis, computer modeling and laboratory experimentation, we explore and compare these three possible sources of difference frequency production with the aim of attaining a more complete understanding of the source of difference frequency signal in the vibro-acoustography imaging system.

The next (second) chapter of this thesis reviews the derivation of the nonlinear wave equation from first principles following the method found in standard references[32,78].[ii] The remainder of this thesis is organized into three main chapters, each of which addresses one of the three possible sources of difference frequency sound. Each chapter contains a theoretical section, a simulation section, and an experimental section. Chapter 3 sets forth an analytical description of the parametric effect, one method of nonlinear production of a difference frequency field. This analytical description models the reflection of a focused beam of one element from a tissue phantom onto the other element of the system. Several experiments demonstrate the correlation between the parametric effect and the orientation of the target. In chapter 4, we solve the second order wave equation for the difference frequency field that exists locally on the surface of an object. Then, we provide the solution for the scattering of this local difference frequency field for various spherical and planar targets. Repeated experiments fail to detect a difference frequency sound from this mechanism. In chapter 5, we calculate the nonlinear interaction of scattered waves from small spherical scatterers by combining linear scattering theory with Dean's[52] nonlinear spherical wave interaction theory. Preliminary experiments illustrate the production of difference frequency sound from small scatterers in a silicone gel phantom.

## 1.3 Description of Dual-Frequency System

The dual-frequency system used for the majority of the experiments and simulations in this thesis are similar to the system proposed by Fatemi and Greenleaf, with several key modifications[1]. These enhancements in the system design include (i) the use of two separate transducer elements arranged at a large angle to one another, (ii) the use of very short pulsed waveforms (rather than

[ii] Each subsequent chapter uses the results of this first mathematical foundation chapter together with coherent wave theory to account for the local difference frequency, parametric, and nonlinear scattering effects.

CW), and (iii) the addition of a dual-directional coupler in order to measure reflected power from one element onto the other element. The modified design still produces difference frequency responses similar to the original system, but allows for the distinction between the various causes of this response. This helps the experimentalist tease apart the physical mechanisms responsible for the total difference frequency response.

The dual-frequency system consists of source generation equipment and difference frequency signal measuring equipment. For source generation, we use either a custom designed dual-frequency amplifier system (Advanced Surgical Systems, Tucson, AZ) or separate function generators (Wavetek model 395, Fluke, Everett, WA and Hewlett-Packard HP33120A, Palo Alto, CA) connected to power amplifiers (ENI 1200L and ENI 3100L, Rochester, NY ). We couple the source generation devices to custom fabricated ultrasound transducers via standard inductor-capacitor (L-C) matching circuitry.

The most important deviation from Fatemi and Greenleaf's system is the design of the transducers. Separating the elements reduces unwanted inter-element interaction and near-field interaction of the two beams. Fatemi and Greenleaf's system design[iii], utilized in preliminary experiments leading to this thesis, consisted of a two-element transducer with elements arranged confocally such that their foci intercept.[iv] This confocal transducer was fabricated in house by etching the ground plane of each transducer separately in order to create two drivable elements from a single PZT-4 crystal. This method of fabrication ensures perfect alignment of the elements with one another. However, we noted that the mechanical coupling of the elements may lead to interaction at the transducer itself which could propagate difference frequency waves towards the focus rather than relying on local interaction at the focus.[79] Previously, a group in France had reported a related result in which they showed that even in the absence of mechanical coupling, the nonlinear interaction of incident sound waves generated with a concentric ring transducer may cause difference frequency sound generation short of the focal region.[42]

---

[iii] Until the most recent paper from Greenleaf's group[140], they utilized the transducer design described in this section.[24] This more recent study compares a transducer design they call "x-focal" which resembles the transducer design used in this thesis and our previous publications[26-28,122].

[iv] We used this design for many preliminary *ex vivo* tissue experiments conducted prior to this doctorate thesis[3], as well as for some of the tissue image results in Chapter 5.

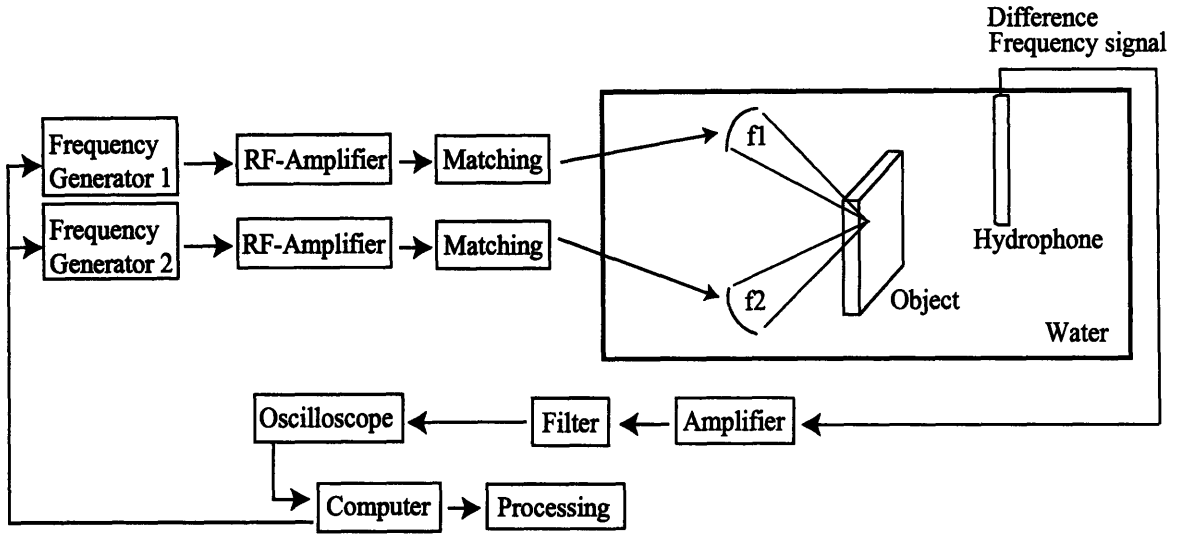


**Figure 1-1:** Diagram of the complete experimental set-up.

This mechanism by which the two fields may interact to produce difference frequency sound if the elements are mechanically coupled or closely spaced will be explained more completely in chapter 3 where the mathematical foundation is established for the generation of difference frequency sound from a parametric array. The main design consideration was simply that the beams from the two elements should be at a considerable angle to one another in order to avoid their interaction before the focal region which would inject addition unwanted complexity to the system and would underlie the design of difference frequency sound generation at the focus only. In order to meet this design constraint, the final system design consisted of two completely separate spherical cap elements positioned at a large angle to one another on an acrylic holder so that their foci intersect but their beams are almost completely independent before the focal region (see Figure 1-1). Certainly, this system minimizes the collinear interaction of the two sources and therefore prohibits the generation of difference frequency sound as described by Westervelt in his paper on the parametric array[80].

For the separate element system, each element was fabricated in house from PZT4 with a diameter of 4cm and focal length of 10cm operating at the third harmonic (1.624 MHz) or the fifth harmonic (2.74 MHz) of the fundamental plus or minus the difference frequency (usually in the kHz or Hz). The two separate elements were mounted on a custom fabricated adjustable acrylic arc so that the experiments could be repeated at various angles of separation. In addition, one of the targets used frequently in this thesis is a silicone gel tissue phantom which has been studied extensively for its tissue-like mechanical properties by Ottensmeyer[81,82].

The measuring equipment consisted of a low frequency hydrophone (International Transducer Corporation 6050C, Santa Barbara, CA) with a sensitivity of –154 dB re 1V/μPa connected to a

digital filter (Stanford Research Systems, SR650, Palo Alto, CA) and registered to a digital oscilloscope (Yokogawa DL7100, Japan). The measurement equipment was controlled by a GPIB IEEE-488 connection to a personal computer and the data was transferred and stored on the hard dive of the computer.

*Peak Pressure*

There are two important values used to characterize the system and provide a relative magnitude with which to compare the pressure of difference frequency sound generated from the three mechanisms described in this thesis. These values are the peak pressure of the incident primary field and the system noise. The peak pressure of the source field provides a relative value with which to scale the measured pressures at the difference frequency. Unlike linear acoustics problems which scale with pressure, the response at the difference frequency is dependant upon the product of the input pressures of the primary beams. This value is proportional to the electrical driving power which is provided through this thesis for reference when describing the simulations and experiments. In general, the driving powers used in experiments range from 1 to 30 W which results in peak pressures ranging from 800 kPa to 7 MPa for the focused primary fields.

For simulations, the peak pressure of the incident field from the source transducers is calculated by a consideration of the efficiency, $\mathrm{E}$, of the transducer, the beam pattern at the focal plane, $f(x,y)$, and the relationship between total acoustical power, $W_A$, and pressure squared, $P^2$, given approximately by,

$$W_E \cdot \mathrm{E} = W_A = \int_{Area} \frac{P^2(x,y)}{Z} dA \tag{0.1}$$

where $Z$ is the acoustical impedance which is equal to the product $\rho \cdot c$ of the speed of sound ($c$) and the density ($\rho$) (for values used see Table 1-4). The integral is evaluated over the area of the focal plane. The efficiency values and beam profiles for one of the dual-frequency systems used in this thesis is provided in Appendix A.

The pressure of the primary field at each point in space as measured by the needle hydrophone can be expressed as $P(x,y) = P_{peak} \frac{f(x,y)}{|f_{max}|}$ where $f(x,y)$ are the relative pressure measurements collected by the hydrophone at each position $(x,y)$ in the plane, $f_{max}$ is the maximum measured value over the region $(x,y)$, and $P_{peak}$ is the peak pressure value for the field.

Substituting this expression into equation (0.1) and solving for $P_{peak}$ gives the following expression for the peak pressure of the incident source field,

$$P_{peak} = \sqrt{\frac{W_E \cdot \mathrm{E} \cdot \rho c}{\int_{Area} \frac{f^2(x,y)}{f_{max}^2} dA}} \tag{0.2}$$

Therefore, we can calculate the peak acoustic pressure over the focused beam, $P_{peak}$, given the input electrical power ($W_E$), the transducer efficiency ($E$), the measured pressure distribution over the focal plane ($f(x,y)$), and the medium properties of density ($\rho$) and speed of sound ($c$).

*Noise Measurements*

We measured the system noise to set a lower bound for the detectable difference frequency sound in our experimental set-up. Any physical process which generates difference frequency sound at amplitudes below the system noise may result in an undetectable signal. The definition of the system noise used in this thesis is the standard deviation of the total background pressure acquired when the experimental system is run without any source of difference frequency sound. This measurement accounts for all signal sources that are not due to difference frequency generation and includes noise contributed by the amplifiers and electronic circuitry as well as background signals and interference in the environment of the experimental set-up.

The system noise was measured in a series of experiments with the digital filter set to two different band-pass settings indicative of difference frequency ranges used in this thesis. These experiments were conducted in order to demonstrate the magnitude of ambient noise in the experimental environment as well as the effect of filtering to reduce low frequency noise. The experiments to determine the amplitude of the noise consisted of acquiring 50 measurements from the low frequency hydrophone used throughout this thesis (International Transducer Corporation 6080c, Santa Barbara, CA) while all electronic devices were on but no dual-frequency signal was radiated from the transducer. The hydrophone signal was band-pass filtered (Stanford Research Systems SR650, Palo Alto, CA) to eliminate frequencies outside of the range 100 Hz - 50 kHz in one experiment and 1kHz – 50 kHz in the other. The signal was then registered to a digital oscilloscope (Yokogawa DL7100, Japan) and recorded to a personal computer via a GPIB-IEEE488 communications line.

The system noise is given below in absolute values of Pa and dB re μPa (Table 1-1). For the band-pass filter setting of 100 Hz – 50 kHz, a noise level of 94 dB (.05 Pa) was measured. For

the band-pass filter setting of 1 kHz – 50 kHz, a noise level of 86 dB (.02 Pa) was measured. The decrease in the noise level for the second experiment can be attributed to the elimination of low frequency noise below 1 kHz arising from mechanical vibrations in the environment as well as flicker noise, an electronic source of noise which is dominant for amplifiers in the hundreds of hertz frequency range[83]. These noise levels recorded for our experimental set-up are similar to the noise level found by Roy and Wu in experiments measuring the scattering of sound by sound with noise levels recorded at 80 dB (.01 Pa)[56].

| Filter Band Pass | System Noise Amplitude (Pa) | System Noise Level (dB re μPa) |
|---|---|---|
| 100 Hz – 50 kHz | .05 | 94 |
| 1 kHz - 50 kHz | .02 | 86 |

**Table 1-1:** Noise measured in experimental environment.

*Description of System Targets*

In this thesis, several targets are used to interact with the acoustical fields to generate difference frequency sound in experiments. The ultimate goal of the dual-frequency system is for use as a tissue imaging modality. Therefore, tissues would be ideal targets for determining the difference frequency generation of the system. To this end, several images are made using a target of fresh *ex vivo* rabbit liver tissue. However, many fundamental principles can be demonstrated for the interaction of the two frequencies using basic targets (referred to as tissue phantoms) with more constant mechanical and acoustical parameters. Tissue phantoms are ideal for the laboratory setting where tissue parameters may not be constant over the course of experiments and where more precise control and repeatability of the target parameters is desirable. The targets used in this thesis include a polyethylene (measuring 10.5 cm x 10.5 cm x 1.1 cm), which is used to model the reflection due to a tissue interface, and a silicone gel tissue phantom (11 cm diameter circular slab, 2.8 cm thick), which is used to model the mechanical properties of tissue. The silicone gel phantom has mechanical properties which closely resemble those of biological tissues and has been used extensively by others to mimic the elastic properties of tissue[84-86]. The acoustical properties of the polyethylene plate and the silicone gel are provided in Table 1-2.

| Target | Speed of Sound, m/s | Density, $kg/m^3$ | Acoustical Absorption (Np/m/MHz) |
|---|---|---|---|
| Polyethylene Plate[87] | 1950 | 900 | 5.53 |
| Silicone Tissue Phantom[v] (30:70, 40:60, 50:50 mix) | 1050 | 1100 | 3.45 |
| Mammalian Muscle[88] | 1508-1630 | 1070-1270 | 2-11 |

**Table 1-2:** Acoustical properties of targets used.

The mechanical Young's modulus of tissue as measured by various methods of mechanical indentation or compression together with the modulus for the silicone gel tissue phantom as reported by Ottensmeyer[86] are presented in Table 1-3.

| Tissue/Material | Young's Modulus, kPa |
|---|---|
| Bovine Liver[89] | .43-1.68 |
| Human Fibroglandular Breast Tissue[90] | 1.8 |
| Human Adipose Breast Tissue[90] | 1.9 |
| Rabbit Liver[91] | 5.6 |
| Rabbit Kidney[91] | 8.8 |
| Silicone Gel[86] (50:50 mix) | 2.39 |
| Silicone Gel[86] (40:60 mix) | 7.63 |
| Silicone Gel[86] (30:70 mix) | 15.3 |

**Table 1-3:** Mechanical properties of tissues and silicone gel tissue phantom.

The system described above in section 1.3 contains the basic elements of the original USVA dual-frequency system while including several enhancements designed to isolate the effects to be studied in this thesis. Before the three nonlinear effects that will be explored can be discussed in particular, the mathematical foundation for the generation of difference frequency pressure must be

[v] We measured the acoustical properties of the silicone gel using standard methods of time of flight for determining the speed of sound as described in Karshner[141] and using an electronic balance together with volume displacement to determine the density. We measured the coefficient of absorption using the standard technique based on the change in the measured radiation force as a function of sample thickness.

established. This basis begins with the derivation of the second order wave equation in the next chapter, after which the general method for solving the wave equation for the difference frequency pressure is presented as well as a discussion of the significance of this equation. These results are then used throughout the thesis in various implementations and models to calculate the generation of difference frequency sound from the three effects considered.

### *Simulation Parameters*

Throughout this thesis, computer simulations are performed to calculate the difference frequency sound generation by the three mechanisms described in this thesis. These simulations are all performed in the Matlab® programming environment on a personal computer with a 2GHz Pentium processor and 1Gb of RAM. The common simulation parameters used throughout this thesis are provided in Table 1-4.

| ***Parameter*** | ***Description*** | ***Value*** |
|---|---|---|
| $c$ | Speed of sound in water medium[v] | 1500 m/s |
| $c_{silicone}$ | Speed of sound in silicone gel tissue phantom[v] | 1050 m/s |
| $c_{polyethylene}$ | Speed of sound in polyethylene plate[87] | 1950 m/s |
| $\rho_0$ | Density of water medium[v] | 998 kg/m$^3$ |
| $\rho_{silicone}$ | Density of silicone gel tissue phantom[v] | 1100 kg/m$^3$ |
| $\rho_{polyethylene}$ | Density of polyethylene plate[87] | 900 kg/m$^3$ |
| $\gamma_{air}$ | Ratio of specific heats for air[76] | 1.4 |
| $\frac{B}{A}$ | Parameter of nonlinearity (for water at 1 atm, 30 $^0$C)[76] | 5.2 |
| $\gamma_{water} = 1 + \frac{B}{A}$ | Relates equations for ideal gases to cases of water medium)[76] | 6.2 |
| $(1-\Gamma)$ | Constant of nonlinearity $= 1 + \frac{(\gamma-1)}{2\gamma}$ for an ideal gas[vi] | 1.4 |

**Table 1-4:** General parameters for simulations used throughout the thesis.

Additional parameters like the power and geometry used, which is specific to the simulation, are detailed in the simulation section of each chapter.

[vi] We calculated this value using definitions from Beyer[76] as well as Morse and Ingard[32].

# 2 Mathematical Foundation

The acoustical wave equation governs the interaction of sound waves with one another and the medium in which they propagate. This equation arises from combining two general equations of fluid motion, namely the equation of continuity and the equation of motion, together with the equation of state, which relates the density to the pressure. In the usual derivation of the linear wave equation, the fundamental equations are linearized before they are combined, thereby eliminating higher order terms. However, the generation of difference frequency sound relies upon the interaction of waves in a nonlinear manner. Therefore, higher order terms must be retained in order to adequately describe this effect using the wave equation.

In this chapter, we briefly review a standard derivation[32,78] of the free-space, second-order, nonlinear wave equation in order to explain the origin of the second-order source term on the right hand side which is not present in the linear wave equation. First, we expand the equation of state, the equation of continuity, and Euler's equation to include second-order terms. Then, we combine these fundamental equations to give the second-order wave equation which includes 'source terms' on the right hand side not present in the linear wave equation.

## 2.1 First and second-order wave equations

The first-order wave equation is derived by combining the linearized form of three fundamental equations: the equation of continuity, the equation of motion, and the equation of state. In order to derive the second-order wave equation, these three fundamental equations are expanded to second order and then combined. The fundamental equations are expanded to second order by inserting field variables expanded to second order into the general form of these equations[32,78]. By way of example, suppose $\psi$ is a field variable, like density or velocity. This variable can be written as sum of increasing order terms such that, $\psi = \psi_0 + \psi_1 + \psi_2 + \ldots$, where $\psi_0$ is the unperturbed value; $\psi_1$ is the first order term; $\psi_2$ is the second order term, etc. This expansion to higher orders is most easily understood by considering the Taylor expansion of $\psi(x)$ about $x = 0$ which takes the form:

$$\psi(x)=\psi(0)+\frac{\partial\psi(0)}{\partial x}\cdot x+\frac{1}{2}\frac{\partial^2\psi(0)}{\partial x^2}\cdot x^2+\ldots\frac{1}{n!}\frac{\partial^n\psi(0)}{\partial x^n}\cdot x^n$$

where the $0^{th}$ order term is $\psi(0)$; the $1^{st}$ order term is $\frac{\partial\psi(0)}{\partial x}\cdot x$; etc. In the three sections that follow, the field variables are preserved to second order such that all second order terms are considered when the three fundamental equations are combined to give the second-order wave equation in free-space.

### *2.1.1 Equation of State*

The equation of state describes the relationship between the density $\rho$ and pressure $P$, where $\rho=\rho(P)$. Generally, the density can be written as the sum of increasing order terms,

$$\rho=\rho_0+\rho_1+\rho_2+\ldots \tag{0.3}$$

In particular, the Taylor series expansion of $\rho(P)$ about $P_0$ is given by,

$$\rho(P)=\rho\big|_{P_0}+\frac{\partial\rho}{\partial P}\bigg|_{P_0}\cdot(P-P_0)+\frac{1}{2}\frac{\partial^2\rho}{\partial P^2}\bigg|_{P_0}\cdot(P-P_0)^2+\ldots \tag{0.5}$$

By equating equations (0.3) and (0.5), and keeping terms up to the first order only, we obtain the following expression,

$$\rho_0+\rho_1=\rho\big|_{P_0}+\frac{\partial\rho}{\partial P}\bigg|_{P_0}\cdot(P-P_0) \tag{0.6}$$

The pressure, $P$, can also be expressed as terms of increasing order such that $P=P_0+P_1+P_2+\ldots$ If we substitute terms up to the first order for $P$ into equation (0.6), it becomes,

$$\rho_0+\rho_1=\rho_0+\frac{\partial\rho}{\partial P}\bigg|_{P_0}\cdot((P_0+P_1)-P_0) \tag{0.7}$$

which easily reduces to

$$\begin{aligned}\rho_1&=\rho_0+\frac{\partial\rho}{\partial P}\bigg|_{P_0}\cdot P_1\\&=\rho_0+\frac{1}{c_0^2}\cdot P\end{aligned} \tag{0.8}$$

The same procedure outlined above can be expanded to include terms up to second-order in equations (0.4) and (0.5) as well as for expressing the pressure $P$. Combining these second-order terms together, we obtain

$$\rho_0+\rho_1+\rho_2=\rho_0+\left.\frac{\partial\rho}{\partial P}\right|_{P_0}\cdot((P_0+P_1+P_2)-P_0)+\frac{1}{2}\left.\frac{\partial^2\rho}{\partial P^2}\right|_{P_0}\cdot((P_0+P_1+P_2)-P_0)^2 \tag{0.9}$$

By substituting in the expression for $\rho_1$ and only retaining terms up to second order[vii], equation (0.9) reduces to,

$$\rho_2=\left.\frac{\partial\rho}{\partial P}\right|_{P_0}\cdot P_2+\frac{1}{2}\left.\frac{\partial^2\rho}{\partial P^2}\right|_{P_0}\cdot P_1^2=\frac{1}{c_0^2}\cdot P_2+\frac{\Gamma}{\rho_0 c_0^4}\cdot P_1^2 \tag{0.10}$$

where $\Gamma=\frac{1}{2}\rho_0 c_0^4\left(\frac{\partial^2\rho}{\partial P^2}\right)_{P_0}$ is a constant of the medium.

## *2.1.2 Equation of Continuity*

The equation of continuity is a conservation equation, which states that the mass flux into a fixed control volume, minus the mass flux out of a fixed control volume, is equal to the change in time of the total mass within the fixed volume. This statement can be expressed in terms of density $\rho$ by dividing through by the volume to give the following general equation of continuity,

$$\frac{\partial\rho}{\partial t}+\nabla\cdot\rho V=0 \tag{0.11}$$

By first expanding the field variables to 0$^{th}$ order such that $\rho=\rho_0$ and $V=V_0$, and imposing the constraint that the resting velocity of the fluid particles is zero ($V_0=0$), it becomes clear that $\frac{\partial\rho_0}{\partial t}=0$. Next, we expand the variables to first-order ($\rho=\rho_0+\rho_1$, $V=V_0+V_1$) and insert the result into equation (0.11). After eliminating higher order terms such as the product $\rho_1 V_1$ (which is second-order), and using the 0$^{th}$ order result above, the first-order continuity equation reduces to,

---

[vii] We note that multiplying two terms together results in a product with order equal to the sum of the orders of each term. For example, a first-order term multiplied by a second-order term results in a product of third-order (i.e. $P_1\cdot P_2=O^3$, where $P_1$ and $P_2$ are terms of first and second order respectively and $O^n$ indicates a term of order $n$).

$$\frac{\partial \rho_1}{\partial t} + \rho_0 \nabla \cdot V_1 = 0. \tag{0.12}$$

Finally, we repeat these steps for the equation of continuity using variables expanded to second-order. Again, we eliminate terms greater than second-order and substitute in the result of the first-order equation (0.12) to simplify the second-order equation of continuity to the form,

$$\frac{\partial \rho_2}{\partial t} + \nabla \cdot \rho_0 V_1 = -\nabla \cdot \rho_1 V_1. \tag{0.13}$$

## *2.1.3 Equation of Motion*

Newton's second law of motion ($F = ma$) can be applied to fluid particles to give the equation of motion for fluid. Newton's law as applied to fluids states that the net force on the fluid contained within an infinitesimal control volume moving with the fluid particles[viii] is equal to the mass times the Lagrangian derivative[ix] of the velocity of the fluid within the control volume. This equation can be written in terms of pressure in a fluid environment by normalizing by the volume and taking the limit as the volume goes to zero. The result is the equation of fluid motion, which in general variables can be written in tensor form as[32],

$$\frac{\partial \rho V}{\partial t} + \nabla \cdot (T_{ij} + \mathrm{B}_{ij} + D_{ij}) = 0 \tag{0.14}$$

where $T_{ij}$ is the momentum flux tensor (also known as the advection term) given by

$$T_{ij} = \begin{pmatrix} \rho u_x u_x & \rho u_x u_y & \rho u_x u_z \\ \rho u_y u_x & \rho u_y u_y & \rho u_y u_z \\ \rho u_z u_x & \rho u_z u_y & \rho u_z u_z \end{pmatrix},$$

$D_{ij}$ is the viscous stress tensor and $\mathrm{B}_{ij} = P \cdot \delta_{ij}$ is the normal stress tensor. These tensor terms arise from the total derivative which, for a vector quantity $\rho V$, is given by

$$\frac{D\rho \mathbf{V}}{Dt} = \frac{\partial \rho \mathbf{V}}{\partial t} + (\nabla \times \rho \mathbf{V}) \times \rho \mathbf{V} + \nabla \frac{1}{2} \mathbf{V}^2.$$

---

[viii] This is known as a Lagrangian reference frame.

[ix] The Lagrangian derivative is also referred to as the Stokes Derivative or the Total Derivative in the literature.

The pressure term is made into a tensor by multiplication with $\delta_{ij}$ since only terms like $P_{xx}$ have physical significance for describing pressure (the cross terms of the pressure tensor are a result of viscous forces and are included as part of the viscosity tensor $D_{ij}$). The viscosity tensor is eliminated by assuming an inviscid medium.

Using the same procedure as above for the other two fundamental equations, we expand the equation of motion (0.14) to its 0th, 1st, and 2nd order. Using the fact that $V_0 = 0$, the 0th order equation is found by observation and reveals that $P_0$ is constant in space. To find the first-order equation, we use the results of the 0th order equation and note that the components of the stress tensor, $u_i u_j$, are all of 2nd order. Therefore, after eliminating high order terms, the remaining terms give for the 1st order equation of motion,

$$\rho_0 \frac{\partial V_1}{\partial t} + \nabla \cdot P\zeta_{ij} = 0 \tag{0.15}$$

Finally, using the variables expanded to 2nd order with the general equation (0.14) and the 0th order and 1st order equations, we can express the 2nd order equation of motion as,

$$\rho_0 \frac{\partial V_2}{\partial t} + \nabla \cdot P_2 = -\nabla \cdot T_2 - \frac{\partial \rho_1 V_1}{\partial t} \tag{0.16}$$

where $P_2$ and $T_2$ refer to the second order terms of the tensors $P \cdot \delta_{ij}$ and $T_{ij}$ respectively.

## *2.1.4 The Wave Equations*

To summarize, first the three fundamental equations were expanded to first order:

$$\begin{aligned}
&\rho_1 = \rho_0 + \frac{1}{c_0^2} \cdot P_1 && \text{equation of state} \\
&\frac{\partial \rho_1}{\partial t} + \rho_0 \nabla \cdot V_1 = 0 && \text{equation of continuity} \\
&\rho_0 \frac{\partial V_1}{\partial t} + \nabla \cdot P_1 = 0 && \text{equation of motion}
\end{aligned} \tag{0.17}$$

Then, in order to eliminate the velocity term, we combine these fundamental equations by equating the time derivative of the equation of continuity with the divergence of the equation of motion[78]. Next, we replace the variable $\rho_1$ using the equation of state. The result is the linear wave equation:

$$\nabla^2 P_1 - \frac{1}{c_0^2}\frac{\partial P_1}{\partial t} = 0 \tag{0.18}$$

We can follow the same procedure with the second order fundamental equations derived above and presented together here:

$$\begin{aligned}
&\rho_2 = \frac{1}{c_0^2}\cdot P_2 + \frac{\Gamma}{\rho_0 c_0^4} P_1^2 && \text{equation of state} \\
&\frac{\partial \rho_2}{\partial t} + \rho_0 \nabla \cdot V_2 = -\nabla \cdot \rho_1 V_1 && \text{equation of continuity} \\
&\rho_0 \frac{\partial V_2}{\partial t} + \nabla \cdot P_2 = -\nabla \cdot T_2 - \frac{\partial (\rho_1 V_1)}{\partial t} && \text{equation of motion}
\end{aligned} \tag{0.19}$$

These fundamental equations are of the same form as the first order equations with the addition of terms on the right hand side called 'source terms'. If we combine these second-order equations with the same algorithm used for the first-order wave equation above, we arrive at the second order wave equation,

$$\nabla^2 P_2 - \frac{1}{c_0^2}\frac{\partial^2 P_2}{\partial t^2} = -\nabla \cdot T_2 \cdot \nabla - \frac{\Gamma}{\rho_0 c_0^4}\frac{\partial^2}{\partial t^2}\left(P_1^2\right) \tag{0.20}$$

Following a change of variables found in Morse and Ingard, we can eliminate the stress tensor $T_{ij}$ from this equation, giving the final result for $P_2'$,

$$\nabla^2 P_2' - \frac{1}{c_0^2}\frac{\partial^2 P_2'}{\partial t^2} = \frac{(1-\Gamma)}{\rho_0 c_0^4}\frac{\partial^2}{\partial t^2}\left(P_1^2\right) \tag{0.21}$$

where $P_2'$ is the second order pressure minus local evanescent pressure terms, $1-\Gamma$ is a constant provided in Table 1-4, $\rho_0$ and $c_0$ are the density and speed of sound respectively also provided in Table 1-4.

## 2.2 Interpretation of Wave Equation

We rely upon the second-order wave equation in our study of the generation of difference frequency sound from two primary frequency sources. This nonlinear wave equation can be interpreted as describing the generation of second order pressure in free space (left hand side of

equation) due to first order pressure sources (right hand side of equation). For a single frequency input, this equation explains the phenomenon of second-harmonic wave generation whereby the input of a waveform given by $P_1 = Ae^{j(k_a r - \omega_a t)}$ will result in sources at both $\omega_a$ and $2\omega_a$ due to the squared $P_1$ source term on the right hand side.

Instead, if we set the pressure $P_1$ equal to the sum of two harmonic waves at different frequencies such that $P_1 = Ae^{j(k_a r - \omega_a t)} + Be^{j(k_b r - \omega_b t)}$, then the $P_1^2$ source term results in harmonics as well as sum and difference frequency sources at $\omega_a \pm \omega_b$ due to cross terms of the input to the second order wave equation, $\frac{(1-\Gamma)}{\rho_0 c_0^4}\frac{\partial^2}{\partial t^2}\left(P_1^2\right)$. This origin of the sum and difference frequency inputs is most easily understood by expressing the primary pressure as an expansion of the two individual input pressures,

$$P_1 = \mathrm{Re}(P_a + P_b) = \frac{1}{2}\left[(P_a + P_a^*) + (P_b + P_b^*)\right] \tag{0.22}$$

where $^*$ indicated the complex conjugate. The second-order pressure terms that are inputs to the wave equation are,

$$\begin{aligned} P_1^2 &= \frac{1}{4}(P_a P_a + 2P_a P_a^* + P_a^* P_a^*) + \frac{1}{4}(P_b P_b + 2P_b P_b^* + P_b^* P_b^*) + \frac{1}{2}(P_a P_b + P_a^* P_b^*) + \frac{1}{2}(P_a P_b^* + P_a^* P_b) \\ &= [\mathrm{Re}(P_a)]^2 + [\mathrm{Re}(P_b)]^2 + \mathrm{Re}(P_a P_b) + \mathrm{Re}(P_a P_b^*) \\ &= \mathrm{Re}(P_a^2) + \mathrm{Re}(P_b^2) + \mathrm{Re}(P_a P_b) + \mathrm{Re}(P_a P_b^*) + \tfrac{1}{2}|P_a| + \tfrac{1}{2}|P_b| \end{aligned} \tag{0.23}$$

These six terms of the final line of this expansion can be understood respectively as the second harmonic of $P_a$, the second harmonic of $P_b$, the pressure at the sum frequency $\omega_a + \omega_b$, pressure at the difference frequency $\omega_a - \omega_b$, and the DC components which come from the pressure squared term $[\mathrm{Re}(P)]^2$ and are commonly referred to as the "radiation pressure". These inputs to the second order wave equation all contribute to the total nonlinear pressure field in space $P_2$. This thesis is concerned only with the generation of sound at the difference frequency. Therefore, the term $\mathrm{Re}(P_a P_b^*)$ is the focus of the analysis in this thesis because it describes a pressure that oscillates at the difference frequency.

This generation of sum and difference frequencies was described in 1925 by Lamb[92], who derived the solution for the nonlinear displacement at the sum and difference frequency resulting

from the combination of two harmonic displacements arising from collinearly propagating plane waves. Later, Thuras experimentally verified Lamb's theoretical work for sound traveling in air at two frequencies[62].

The generation of sum and difference frequency waves from collimated, non-collinear plane waves is more complicated than the earlier findings for collinear plane waves. This added complexity spurred a series of papers referring to "The Scattering of Sound by Sound". In his 1957 paper by the same title, Westervelt provided a theoretical proof that two plane waves traveling in free-space cannot produce propagating sum and difference frequency waves unless the primary plane waves are collinear (meaning the angle between their directions of propagation equals 0)[47]. According to Westervelt, for the case of non-collinear waves, the sum and difference frequency waves only exist locally in the interaction region of the two primary waves[47]. Ingard/Pridmore Brown had previously demonstrated what some considered a conflicting theoretical derivation together with experiments that appeared to support their derivation. Ultimately, alternative explanations were suggested for the results obtained by Ingard. Several papers, including one by Bellin and Beyer[58] and one by Jones and Beyer[75] supported Westervelt's conclusions. For the limiting case of collinear propagation, Westervelt described the parametric array, whereby low frequency (difference frequency) could be highly focused and directional. In addition, Westervelt arrived at a second-order wave equation (Equations (7) and (8) in his 1963 parametric array paper)[65] which is equivalent to the second-order wave equation given above (0.21) given the definition of the constant $(1-\Gamma)$ from Morse and Ingard[32]. However, Westervelt arrived at the solution using a different approach than outlined in this thesis. In his analysis, Westervelt derived the second-order wave equation by expanding Lighthill's exact equation of fluid motion[x] and discarding source terms on the right hand side which do not significantly contribute to the scattered field at the difference frequency.

The background set forth above serves to provide historical context for this thesis and illustrates that topics related to the scattering of sound by sound addressed in papers of the 1950's and 1960's are pertinent to this study of the generation of difference frequency in the USVA system. In fact, Westervelt briefly described the Parametric Effect, one of the three mechanisms we study in this thesis as a source of difference frequency sound, in a short paper addressing experimental considerations for the scattering of sound by sound in 1990.[93]

In the following chapters, we describe three nonlinear effects that rely upon the free-space nonlinear wave equation derived above to generate difference frequency sound. Each effect is a variation on the theme of producing difference frequency sound due to nonlinear source terms

---

[x] Westervelt notes that the governing wave equation used as the starting point for the derivation in his 1957 paper[47] (equation 1) was also derived by Eckart in 1948.

present in a homogeneous medium. We calculate the generation of difference frequency sound using the free-space nonlinear wave equation (0.21) together with various linear scattering effects. The parametric effect we develop for this thesis is closely related that described by Westervelt. The other two effects involving the linear reflection of the local difference frequency field and the nonlinear interaction of linearly scattered waves were considered previously by Makris *et al.* for the case of plane waves.[94] In addition to the three effects studied here, there exist other nonlinear effects, which can be described using a nonlinear wave equation derived for an inhomogeneous medium with imposed boundary conditions. These additional sources of difference frequency sound, which have been proposed by Makris *et al.*, are beyond the scope of this thesis.[94]

## 2.3 General Solution to Second Order Wave Equation

The standard method for solving the wave equation (0.21) for the total second-order pressure $P_2$ involves taking the Fourier transform in time to transform the wave equation into the Helmholtz equation. For this nonlinear wave equation of section 2.1.4, the Helmholtz equation takes the form,

$$(\nabla^2 + k_\pm^2)P_\pm = \frac{1-\Gamma}{\rho_0 c_0^2} k_\pm^2 P_a P_b = S \tag{0.24}$$

where $P_\pm$ is the second-order pressure at either the sum or difference frequency, $P_a$ is the pressure at one of the primary frequencies, and $P_b$ is the pressure at the other primary frequency.[xi] The general solution to the Helmholtz equation is found by multiplying the source term $Q$ by the free-space Green's function, $\frac{e^{j(k_\pm|\mathbf{r}-\mathbf{r}'|)}}{4\pi|\mathbf{r}-\mathbf{r}'|}$ (the particular solution to the Helmholtz equation for a point source in free-space) and integrating over the volume of sources as follows[78,95],

$$P_\pm(\mathbf{r}) = \int_{Volume} \frac{1-\Gamma}{\rho_0 c_0^2} k_\pm^2 P_a P_b \cdot \frac{e^{j(k_\pm|\mathbf{r}-\mathbf{r}'|)}}{4\pi|\mathbf{r}-\mathbf{r}'|} dV \tag{0.25}$$

In cases where the primary waves can be expressed as analytic functions, they may be inserted for $P_a$ and $P_b$ directly, and the integral can often be solved or an approximate solution

found. Thuras[62] solved for the sum and difference frequency pressure resulting from the interaction of two *collinear* plane waves using the nonlinear derivation of displacement at the sum and difference frequency provided by Lamb[92]. Dean reiterated this result.[52] Using Dean's notation[52], the solution for the sum and difference frequency pressure field resulting from the interaction of two collinear plane waves $P_a = Ae^{j(k_a x - \omega_a t)}$ and $P_b = Be^{j(k_b x - \omega_b t)}$ is,

$$\begin{aligned} P_{\pm}(\mathbf{x}) &= \mathrm{Re}\frac{1-\Gamma}{2j\rho_0 c_0^2} k_{\pm} ABx \cdot e^{j(k_{\pm}x - \omega_{\pm}t)} \\ &= \frac{1-\Gamma}{2\rho_0 c_0^2} k_{\pm} ABx \cdot \sin(k_{\pm}x - \omega_{\pm}t) \end{aligned} \tag{0.26}$$

where $x$ is the propagation distance from an infinite planar source at $x=0$, $k_{\pm} = \frac{\omega_{\pm}}{c}$ is the wave number for either the sum or difference frequency ($\omega_+ = |\omega_a + \omega_b|$ and $\omega_- = |\omega_a - \omega_b|$ are the angular frequencies for the sum and difference frequency waves respectively), and $\rho_0, c_0$ are the density and speed of sound of the medium respectively. This solution shows that for *collinear* plane waves, the amplitude of the sum or difference frequency pressure increases with the propagation distance, $x$, of the two primary waves and is proportional to the wave number, $k_{\pm}$.

Further, Dean found solutions for the second-order wave equation using canonical cylindrical waves and spherical waves. Given spherical waves $P_a$ and $P_b$ radiating from the same source point at frequencies $\omega_a$ and $\omega_b$, the sum and difference frequency field given by Dean[52] is,

$$\begin{aligned} &P_{\pm}(r) = \mathrm{Re}\frac{1-\Gamma}{\rho_0 c_0^2} k_{\pm} P_a P_b \cdot e^{j(k_{\pm}r - \omega_{\pm}t)} \cdot \frac{1}{r}\left[\ln\frac{r}{a} - e^{-j\phi(r)}\right] \\ &\text{where } \phi(r) = 2k_{\pm} r \int_a^r \frac{e^{2jk_{\pm}r}}{r} dr \end{aligned} \tag{0.27}$$

for a small radiating sphere of diameter $a$.[52] The spherical wave solution is particularly useful because it will be helpful for determining the nonlinear interaction of scattered waves from small targets like bubbles in chapter 5. In chapter 5, the form of the scattered primary wave from a small spherical bubble and pressure release surface for which $ka \ll 1$ is approximated by an omni-directional outward spreading spherical wave. Therefore, when considering the interaction of scattered primary waves from small objects, the spherical wave solution to the second-order nonlinear wave equation can be used with the solution for the linear spherical scattering problem to

---

[xi] In the case of the difference frequency solution, the complex conjugate of $P_b$ is used.

find the resulting sum and difference frequency pressures as a function of radial distance $r$. For the more general problem where the pressure field cannot be described analytically, the second order field can be solved numerically given the pressure values of the two primary fields at all points in space and equation (0.25).

# 3 The Parametric Effect

This chapter focuses on a specific type of difference frequency sound generation originally described by Westervelt as the "parametric effect".[93] The parametric effect causes the nonlinear production of difference frequency sound through the reflection of a field at one frequency from a transducer radiating at a different frequency. The reflected field travels collinearly with the radiated field and produces difference frequency sound. Fatemi and Greenleaf may allude to this effect in their article describing the use of the USVA imaging system for tissue mammography when they report that, "the field intensity and resulting image can become excessively sensitive to the transducer-to-object distance" [30]. In this chapter, we propose a mechanism based on the theory of the parametric array described by Westervelt in 1963[65], that can account for this enormous sensitivity to the target orientation as observed by Fatemi and Greenleaf.

The theory of the parametric array emerged from an active period of investigation on the nonlinear interaction of two sound beams which began with the work of Lighthill on the theory of sound produced aerodynamically.[96,97] Lighthill's equations were applied to two beams interacting at right angles by Ingard and Pridmore-Brown in a paper entitled "The Scattering of Sound by Sound", published in the Journal of the Acoustical Society of America in 1956.[63] This paper sparked disagreement in the field of acoustics regarding the creation of scattered sound waves at the sum and difference frequency from the interaction of incident waves at non-zero angles of propagation. In response to Ingard's experimental results demonstrating scattered sum frequency sound, Westervelt began his analysis with Lighthill's equations of fluid motion and derived a theory of scattered sum and difference frequency waves from the intersection of collimated beams in his papers on the scattering of sound by sound[64,74,98]. At the suggestion of Lighthill, Westervelt also considered the case for two perfectly collinear fields in a paper called the "Parametric Acoustic Array"[65]. Westervelt's papers proposed that only plane waves propagating in the same direction will interact to produce sum and difference frequency waves which propagate. However, authors including Berktay and Al Temimi published theoretical and experimental papers with results demonstrating the production of a sum frequency field despite a non-zero angle between incident primary waves[99-101]. In his derivation, Berktay assumes that the two primary beams are fully collimated, but in experiments, the fact that the beams are not perfectly collimated allows for partially collinearity of the pressure fields. In part, due to conflicting theoretical and experimental

results, the scattering of sound by sound remained a popular topic for years after the original paper by Ingard and Pridmore-Brown.[46,49,57,59-61,64,66-75]

Westervelt revisited the topic of the scattering of sound by sound in a short paper in 1990 in which he suggested that the direct interaction of the field of one element with another in a dual frequency system may produce sum frequencies via a parametric interaction of their fields.[102] In his simple experiment, he pointed one element directly at the other and noted that the sum frequency was produced, suggesting that the field of one element was reflected from the surface of the second element and thereby traveled collinearly with the primary field of the second element, similar to a parametric array driven at both primary frequencies.

In a similar vein, we hypothesize in this thesis that the dual-frequency imaging system creates difference frequency sound due to the field of one element reflecting from the surface of the target and projecting back onto the other element, thereby creating a parametric effect like the one observed by Westervelt. This effect would happen simultaneously on both elements and would be proportional to the amplitude of reflected sound from the target. In addition, the amplitude of the difference frequency field would be very sensitive to the geometry of the target, particularly the position and orientation of the target surface.

In this chapter, we first review the parametric array and relate the parametric array to the parametric effect, which we hypothesize for the dual-frequency imaging system. In the parametric array section, we review the volume integral solution to the second order wave equation and also develop an approximate solution for the propagating field at the difference frequency, providing a useful method for rapidly simulating the field over large volumes of interaction. This approximate solution is compared with the volume integral solution to the wave equation and experimental measurements of the difference frequency field from a parametric radiator. In the parametric effect section of this chapter, we first present a theoretical model to account for the multiple reflections needed to generate the parametric effect. Then, we demonstrate the relatively large difference frequency pressure (Pa levels) produced by the parametric effect based on results from the simulation as well as experiments. We find that the difference frequency field is at a pressure well above the amplitude of the system noise and many orders of magnitude ($10^7$ times) above the difference frequency response due to the incident difference frequency field scattered from a target as discussed in chapter 4.

## 3.1 The Parametric Array

Westervelt described the difference frequency pressure field produced by the collinear interaction of two collimated plane waves traveling in the same direction in a 1963 paper entitled "Parametric Acoustic Array". His work was closely related to previous work by Lamb[92] and Thuras[62] that described the production of difference frequency sound through the interaction of collinear plane waves. In his derivation, Westervelt includes the condition of collimated beams to restrict the interaction of the two fields to a limited region called the interaction region. The interaction region is defined as the volume in space over which both collimated beams achieve a non-zero pressure. In his paper, Westervelt derives the equation for the scattered difference frequency wave by starting with Lighthill's exact equation for fluid motion, $\frac{\partial^2 \rho}{\partial t^2} - C_0^2 \nabla^2 \rho = \frac{\partial^2}{\partial x_i \partial x_j} T_{ij}$ (where $T_{ij} = \rho u_i u_j + p_{ij} - C_0^2 \rho \delta_{ij} + D_{ij}$ is the complete stress tensor and $D_{ij}$ represents the viscous stresses), and successively eliminating terms on the right hand side that do not significantly contribute to the second order field outside of the interaction region of the two collimated beams. This approach reduces Lighthill's complete equation of motion to a wave equation for the scattered second order pressure field $P_s$,

$$\nabla^2 P_s - \frac{1}{c_0^2} \frac{\partial P_s}{\partial t} = -\rho_0 \frac{\partial q}{\partial t} \tag{0.28}$$

where "q is the simple source strength density resulting from the primary waves $p_i$"[65] which Westervelt defines as,

$$q = \frac{1}{\rho_0^2 C_0^4} \left[ 1 + \frac{1}{2} \rho_0 C_0^2 \frac{d^2 p}{d \rho^2} \bigg|_{\rho = \rho_0} \right] \frac{\partial}{\partial t} p_i^2 \tag{0.29}$$

This equation is equivalent to the second order wave equation provided (0.21) in chapter 2. Likewise, we can solve equation (0.28) using the method outlined in section 2.3, which involves converting the wave equation into a Helmholtz equation and integrating the source distribution multiplied by the Green's function over the entire volume of interaction of the two fields.

### *3.1.1 Application to Parametric Effect*

The parametric effect follows the same principles of sum and difference frequency sound production as the parametric array. The only distinguishing feature of the Westervelt's parametric effect is that the collinear interaction does not arise from one source driven at two frequencies but rather from two frequencies emanating from a single source by means of the reflection of one beam from the surface of the second transducer. The illustration in Figure 3-1 diagrams the parametric array and the parametric effect to illustrate their relation to one another.

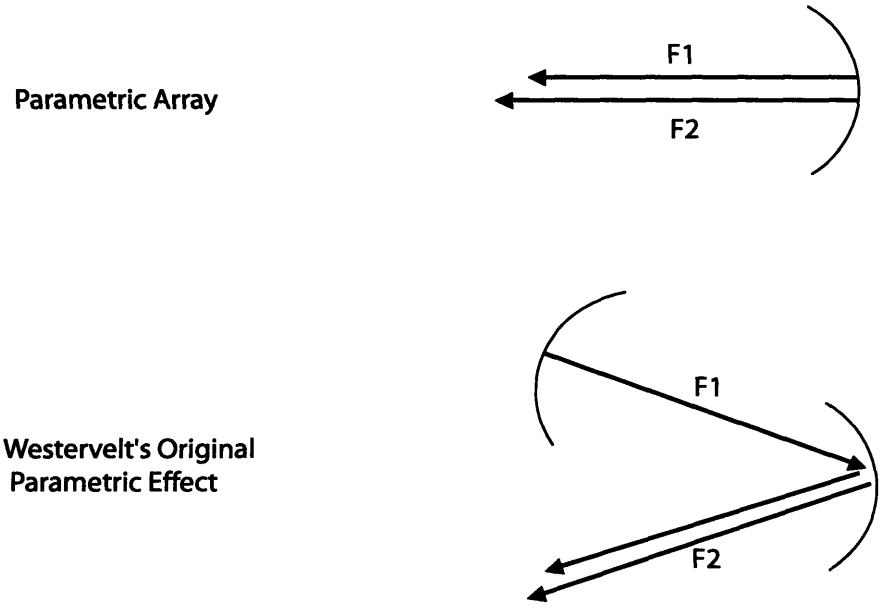


**Figure 3-1:** Diagram illustrating parametric array vs. parametric effect.

### *3.1.2 Simulating the Second Order Field*

The direct method for solving the nonlinear wave equation in order to calculate the difference frequency field involves multiplying the source term by the Green's Function and integrating over the entire volume of source terms. This solution method is not computationally burdensome for a transducer geometry that creates a limited interaction region[xii] of the two fields because in this case, the resulting volume of source terms is small. We use this solution method in

[xii] Here we use the term "interaction region" to indicate the volume in space over which the two pressure fields both achieve appreciable amplitudes (as opposed to our previous definition of the interaction region for perfectly collimated beams stating that the interaction region is the volume in space over which both beams achieve *non-zero* amplitudes).

chapter 4 to simulate the second order pressures incident on a planar target from two transducers orientated at an angle to each other (see Figure 3-2).

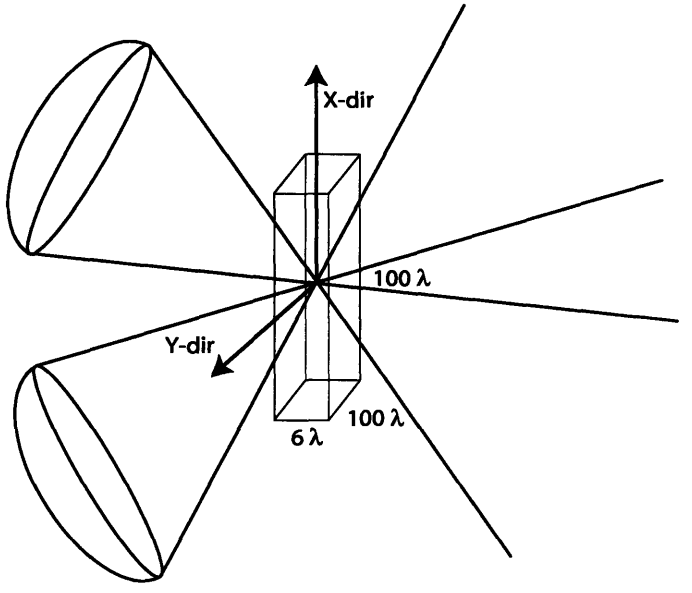


**Figure 3-2:** Diagram of the limited volume of interaction for two angled transducers operating at different frequencies.

However, this same solution method can become extremely intensive for the parametric array because the volume of the interaction region in this case is much larger (see Figure 3-3). When discretizing the space for a numerical implementation of the integral for the parametric array, the domain of the integral can become large considering the small wavelengths involved in the problem ($\lambda \sim 10^{-4}$ m) and the relatively large volume over which the primary fields will interact ($x, y, z \sim 10^{-1}$ m). For reasonable phasing of the primary field, a step size of $\lambda/6$ or $\lambda/8$ is needed to discretize the space. This creates an integral domain containing roughly $10^9$ points in order to find the scattered field at one point in space. If the calculation of the field over a plane in space is required, this integral space will increase by several additional orders of magnitude. In addition, the Green's function given by $\frac{e^{jk|\mathbf{r}-\mathbf{r}'|}}{4\pi|\mathbf{r}-\mathbf{r}'|}$ becomes infinitely large as $|\mathbf{r}-\mathbf{r}'|$ goes to zero. This occurs as the point at which the scattered field is calculated approaches the source points. In typical radiation problems, the source array is often an isolated surface or even a volume of elements which is considered 'outside of the medium' with the calculation points at a distance away from these sources and 'within the medium'. However, in the unique setting of the parametric array, the sources exist everywhere in space where both primary fields exist. Therefore, in numerical

calculations of the volume integral, the scattered field will often be calculated at points very close to, if not at the sources.

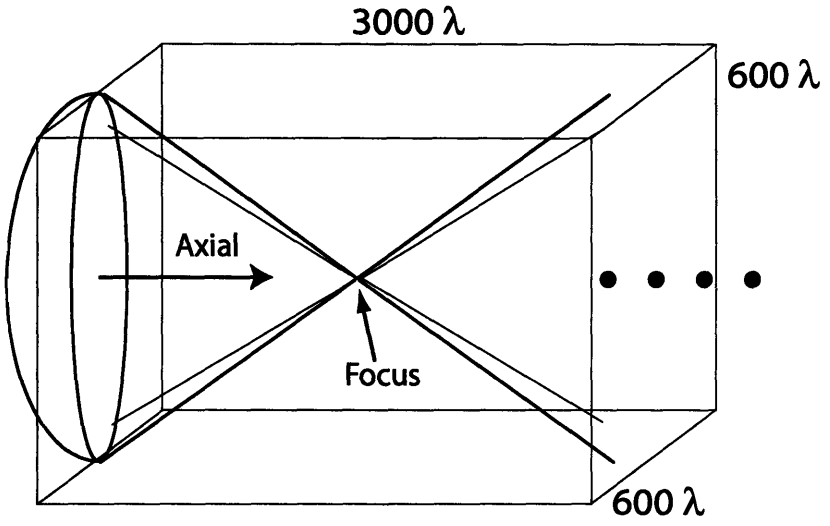


**Figure 3-3:** Diagram of the extensive volume of interaction for a parametric array operating at two frequencies. The parametric array used for the simulations below and experiments in section 3.1.3 is illustrated here. This transducer has an outer diameter of 4 cm, a radius of curvature of 10 cm, and operates at a center frequency of 2.74 MHz. The four points represent the locations simulated using the volume integral method and plotted in **Figure 3-4**.

For these reasons of computational intensity and singularities of the integral, other authors in the literature have used basic geometries and simplifying approximations to calculate the scattered field. Many employ the KZK equation[103,104] (which is a paraxial approximation to the second order wave equation and therefore only should be used for cases involving slowly spreading beams) as well as other quasilinear or parabolic approximations[53,105,106]. One method to offset the singularity at the source points is to add an attenuation term $e^{-\alpha|r|}$, which Westervelt does in his parametric array paper[65].

Despite these complications, the difference frequency field resulting from a focused parametric array (4 cm diameter, 10 cm radius of curvature) driven at 2.705 and 2.755 MHz was simulated using the Green's Function volume integral method described above for a range of values along the axis of propagation at distances typical for experiments with the dual-frequency system (see Figure 3-3). For this simulation, the fields of the primary waves are discretized to $\frac{\lambda}{6}$ spacing and solved for a volume extending from the source at $z = -.095$ meters to the furthest receiver point at $z = .4$ meters and over a range of $-.025 < x, y < .025$ meters. The interaction of these primary fields creates the source terms for the nonlinear field. Their product together with the constants for

the source strength $S$ are multiplied by the Green's Function and integrated over the volume of interaction. The result of the simulation of difference frequency sound generation is plotted for a limited number of on-axis points in Figure 3-4. For this simulation, we modeled a focused transducer with the dimensions of 4cm diameter and 10 cm radius of curvature which was driven at a center frequency of $2.74Mhz \pm 25kHz$ to yield a difference frequency of 50 kHz. The transducer was driven at 1.6 W electrical power which corresponds to a peak acoustic pressure of approximately .85 MPa at the focus of each primary field. The result of the simulation plotted in Figure 3-4 is the solution for the difference frequency field, which includes the local evanescent field as well as the propagating field.

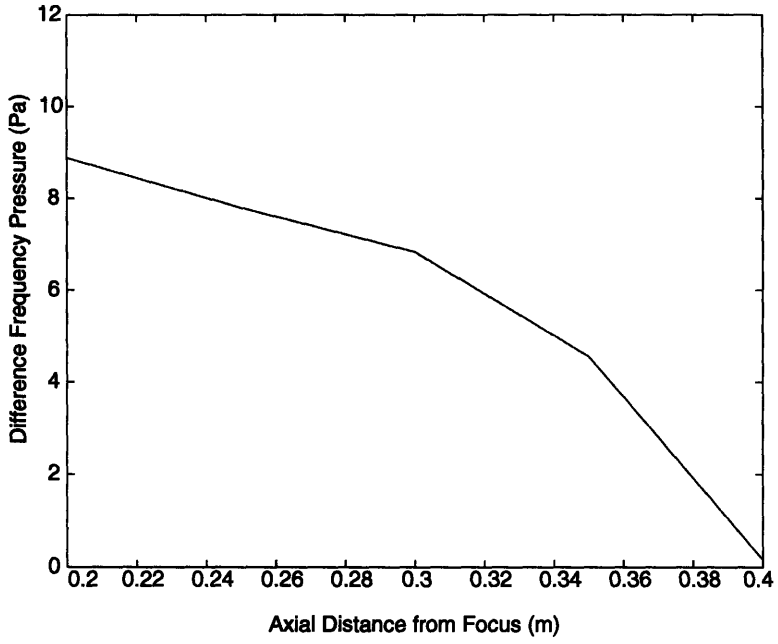


**Figure 3-4:** Simulated difference frequency level obtained using the volume integral solution for a parametric array. The simulation is evaluated at several points on-axis using the Green's function integral method to calculate the propagating difference frequency field of a parametric array operating at 1.6 W electrical power (.85 MPa peak acoustic pressure) per frequency and a difference frequency of 50 kHz.

### *Approximation to the Difference Frequency Field*

In this section, we formulate an approximation to the propagating field of the second order wave equation in order to overcome the singularities and the computational intensity of solving the full volume integral. This approach is related to the work of Woodsum and Westervelt who devised a "General Theory for the Scattering of Sound by Sound" which relies on the spatial Fourier Decomposition of the primary field into plane wave components and the application of an

inverse operator to solve the wave equation (0.24) for the sum or difference frequency pressure $P_{\pm}$.[49,107] The inverse operator they use includes terms derived from the inverse of the d'Alembertian operator (where the d'Alembertian is defined as $\Box^2 = \frac{\partial^2}{\partial t^2} - c_0^2 \nabla^2$) as well as boundary conditions[49,107,108]. At about the same time that Woodsum and Westervelt published their solution, the French researchers Hennion and Alais proposed a similar method for solving for the second order pressure using a Fourier decomposition of the primary field.[109-111] By operating on the Fourier transform of the primary fields and integrating over the solid angles of the plane wave propagation directions, Woodsum and Westervelt's method reduces the complexity of the solution, compared to using the previously discussed standard approach which relies on a three-dimensional volume integral. Their method relies upon the interaction of all plane waves to produce both evanescent and propagating pressures at the difference frequency. In an effort to simplify their approach further, we formulate an approximation to the propagating part of the second order field in this section.

The propagating difference frequency field can be estimated by considering only the interaction of collinearly propagating plane waves. Lamb's solution for the nonlinear interaction of plane waves is utilized for pairs of co-directional plane waves. The collinear plane wave solution to the second-order wave equation is written in this thesis using Dean's notation in equation (0.26). The Woodsum and Westervelt method, which is three dimensional in the wave-vector $\mathbf{k} = (k_x, k_y, k_z)$, can be reduced to a two-dimensional integral for the approximation of highly directional sound beams by noting the wave-vector constraint for propagating waves, $|\mathbf{k}| = \frac{\omega}{c} = \sqrt{k_x^{\,2} + k_y^{\,2} + k_z^{\,2}}$ where the magnitude of the wave-vector, $|\mathbf{k}|$, is known for the pressure fields of the primaries at a given frequency. First, the two primary fields $P_a$ and $P_b$ are expressed as a "local plane-wave spectrum" as described by Korpel[112] and Ludwig and Wong[113], by taking the two-dimensional Fourier Integral over the plane $(x, y)$ in space at a depth $z_0$ indicating the beginning of the interaction region,

$$P_a(k_{ax}, k_{ay}; z_0) = \int_{-\infty}^{\infty}\int_{-\infty}^{\infty} P_a(x, y, z_0) e^{-j(k_{ax}x + k_{ay}y)} dxdy$$
$$P_b(k_{bx}, k_{by}; z_0) = \int_{-\infty}^{\infty}\int_{-\infty}^{\infty} P_b(x, y, z_0) e^{-j(k_{bx}x + k_{by}y)} dxdy \qquad (0.30)$$

where $\mathbf{k}_a = (k_{ax}, k_{ay}, k_{az})$ is the wave-vector for the pressure field at frequency $\omega_a$ (likewise for $\mathbf{k}_b$), and for the case of a parametric array, the $(x, y, z)$ axis is oriented with $z$ pointing in the direction normal to the center point on the transducer surface and $(x, y)$ spanning a plane in space parallel to the transducer surface as illustrated in Figure 3-5.

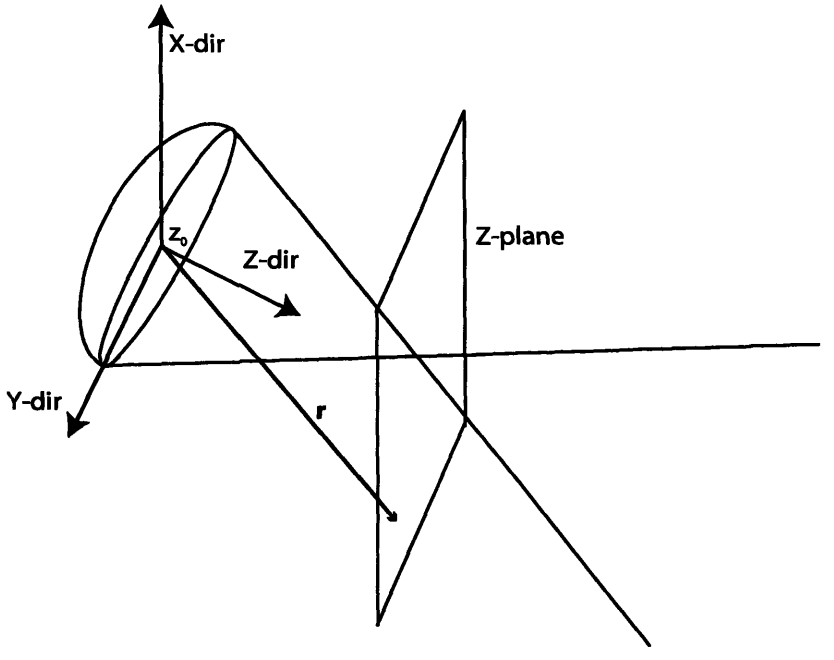


**Figure 3-5:** Diagram of a focused transducer with the orientation of the $(x, y, z)$ axes indicated.

Next, the solution for the difference frequency pressure generated by the collinear propagation of plane waves given in equation (0.26) is applied to planar components $P_a(\mathbf{k}_a)$ and $P_b(\mathbf{k}_b)$ which are propagating in the same direction such that $\frac{\mathbf{k}_a}{|\mathbf{k}_a|} = \frac{\mathbf{k}_b}{|\mathbf{k}_b|}$. We write the result in terms of solid angles $\mathbf{\Omega}_a, \mathbf{\Omega}_b$ corresponding to the plane wave propagation directions $\frac{\mathbf{k}_a}{|\mathbf{k}_a|}, \frac{\mathbf{k}_b}{|\mathbf{k}_b|}$. The result is the difference frequency pressure density over solid angles $\mathbf{\Omega}_a, \mathbf{\Omega}_b$ that is generated by each pair of collinear plane wave components and given by the approximation,

$$\tilde{P}_{-}(\mathbf{r}, \mathbf{\Omega}_a, \mathbf{\Omega}_b) = \mathrm{Re}\frac{1-\Gamma}{2j\rho_0 c_0^2} k_{-} P(\mathbf{k}_a) P^*(\mathbf{k}_b) \cdot D \cdot e^{j(|\mathbf{k}_a - \mathbf{k}_b|\cdot r - \omega_{-} t)} \delta(\mathbf{\Omega}_a - \mathbf{\Omega}_b) \qquad (0.31)$$

where $\tilde{P}$ indicates pressure density over the solid angles $\mathbf{\Omega}_a, \mathbf{\Omega}_b$, $\mathbf{r}$ is a point on the new z-plane, $D$ is the distance of propagation for the plane wave in the direction $\mathbf{\Omega}_a = \mathbf{\Omega}_b$ from the source at $z_0$, $P^*$ represents the complex conjugate of the pressure $P$, $k_{-} = \frac{\omega_{-}}{c} = \frac{|\omega_a - \omega_b|}{c}$ is the difference frequency

wave-number, and $\delta(\Omega_a - \Omega_b)$ is the Dirac delta function, used here in a somewhat heuristic manner to indicate that we consider only plane wave components traveling in the same direction such that $\Omega_a = \Omega_b$. The geometry for one such pair of collinear plane wave components is depicted in Figure 3-6.

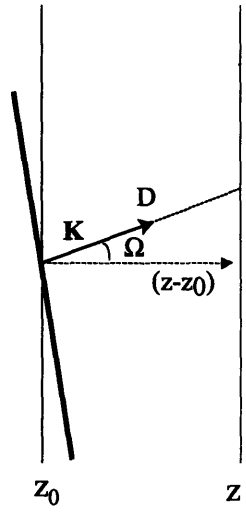


**Figure 3-6:** Diagram of the approximate solution method for the parametric array. This diagram illustrates one pair of collinearly propagating plane waves traveling at an angle Ω, relative to the z-axis.

An approximate expression for the total difference frequency pressure $P_{-}(\mathbf{r})$ at position $\mathbf{r} = (x, y, z)$ is found by integrating over all propagation directions $\Omega_a, \Omega_b$ and is given by,

$$P_{-}(\mathbf{r}) = \frac{1}{(2\pi)^4} \int_{\mathbf{k}_b} \int_{\mathbf{k}_a} \mathrm{Re} \frac{1-\Gamma}{2j\rho_0 c_0^2} k_{-} P(\mathbf{k}_a) P^*(\mathbf{k}_b) \cdot D \cdot e^{j(|\mathbf{k}_a - \mathbf{k}_b|\mathbf{r} - \omega_{-} t)} \delta(\Omega_a - \Omega_b) k_a k_b d\Omega_a d\Omega_b \qquad (0.32)$$

where we limit the propagation angles over which the integrand is evaluated to satisfy the approximation of highly directional beams. The integrand may be restricted by simply filtering the plane wave components in the spatial frequency domain so that values of $P_a(\mathbf{k}_a)$ and $P_b(\mathbf{k}_b)$ are eliminated for large values of $k_x$ and $k_y$ (which represent plane waves with large angles of propagation $\Omega_a, \Omega_b$ relative to the z-axis). Another method for limiting the integral is to include an *ad hoc* attenuation term $e^{-\alpha D}$ in order to attenuate plane wave components propagating for large distances $D$ (where $D = \frac{|z - z_0|}{\cos\varphi}$) at large angles $\Omega$ (where $k_z \ll 1$), which would violate the approximation of highly directional beams. Following a heuristic approach, we found that a value

of $\alpha = \alpha_1 + \alpha_2 = 3.7/m$ for the attenuation coefficient provided the best match between the position of the peak difference frequency pressure generated by a parametric array in simulations and experiments.

This approximation for the difference frequency pressure considers only the interaction of collinear propagating plane waves and ignores the interaction of non-collinear plane waves included in Woodsum and Westervelt's complete solution. However, as the experimental verification below demonstrates, for the geometries considered in this thesis, the approximate solution is consistent with the experimental results. As compared to the full volume integral, this approximate expression greatly reduces the computational time for the problem (by a factor of at least 1000) and also eliminates the problem of singularities at the source points.

The propagating difference frequency field was simulated using equation (0.32) in the Matlab® programming environment. The simulation of a 4 cm diameter, 10 cm radius of curvature transducer operating at 2.705 and 2.755 MHz with an electrical power of 1.5 W per element (corresponding to a peak acoustic pressure of .85 MPa at the focus of each primary field) was calculated at receiver points along the axis of propagation from $0 < z < .4$ meters (where the focus of the primary beams is located at $z = 0$). The result is compared to experiments below in Figure 3-7. The results of the approximate solution are at nearly the same magnitudes as the volume integral solution ($\sim 10Pa$) and actually fit the data a bit better than the integral solution because the finite volume considered for the integral method neglected portions of the primary beams which have spread outside of $-.025 < x, y < .025$ meters. This necessary limitation on the domain of the integral due to the computational intensity of the problem creates artificial boundary conditions for the sources, reducing the accuracy of this calculation. In contrast, the solution algorithm provided here has no such boundary conditions. The approximate solution method neglects evanescent contributions to the difference frequency field, but we assume that these are relatively small far from the focal region of the primary beams.

### *3.1.3 Experiment*

We conducted experiments to produce a focused acoustical field at the difference frequency created by a geometrically focused transducer driven simultaneously at two primary frequencies (driven as a parametric array). These experiments were consistent with the difference frequency field levels we calculated using the approximate method of simulation described in equation (0.32) because they demonstrated reasonable agreement between the simulated and experimentally measured beam patterns. These experiments also established a relative order of magnitude for the

difference frequency signal generated from the transducer geometries we use in this thesis. The maximum difference frequency signal generated by a parametric array imposes an upper limit on the magnitude of the expected difference frequency pressure when considering the related parametric effect.

A single geometrically focused transducer fabricated in-house from PZT-4 was driven by an arbitrary waveform generator (Wavetek model 395, Fluke, Everett, WA) using the suppressed carrier AM modulation mode (SCM) which creates an output at the sum of the two sideband frequencies only. The carrier is suppressed and not part of the output signal. For these experiments, the carrier was set to 2.74 MHz with a modulation frequency of 25 kHz, thereby creating an output at both 2.715 and 2.765 MHz from the single element (difference frequency = 50 kHz). The waveform generator signal was amplified (ENI 2100L, Rochester, NY) to 1.6 W electrical power (corresponding to a peak acoustic pressure of .85 MPa at the focus of each primary field) and the output was sent to the transducer which was matched to 50 Ω and 0 phase via standard L-C matching circuitry. The signal was measured with a low frequency hydrophone (International Transducer Corporation ITC6050c, Santa Barbara, CA), notch filtered around the difference frequency from 48.5 – 51.5 kHz, registered to a digital oscilloscope (Yokogawa DL7100, Japan), and recorded to a personal computer via a IEEE-488 GPIB connection.

The results of the experiment, along with the results of the simulation using the approximate solution developed above, are plotted in Figure 3-7. The simulation (line) is plotted along with the measured data (*) to demonstrate their correlation both with regard to the shape and magnitude of the difference frequency field. The results indicate a difference frequency that rises until approximately 25 cm from the focus of the primaries and then begins to decrease in amplitude. The measured field correlates with the simulated field using the approximate method outlined above, although the peak of the measured field at 25 cm is more pronounced and the maximum amplitude of the difference frequency on-axis is slightly greater. We note that although we only simulate a few values at the difference frequency using the volume integral solution method as displayed in Figure 3-4, these pressure values are also of the same order of magnitude (4-9 Pa) as the experimental measurements.

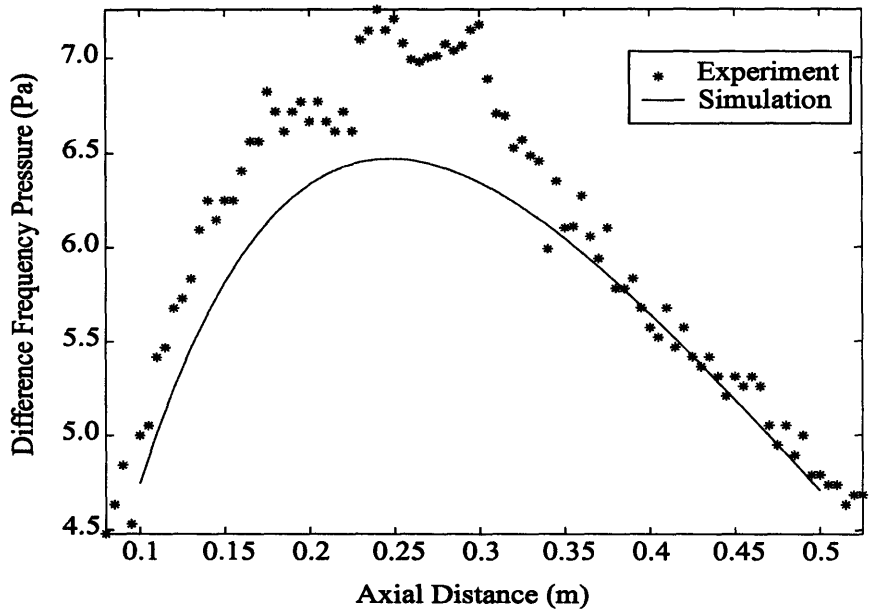


**Figure 3-7:** Axial scan experiment and simulation using approximate solution method of the difference frequency field generated by a focused parametric array.

Finally, we recorded the difference frequency response over a plane of measurement points as indicated in Figure 3-8. In this experiment, the data is acquired as the low frequency hydrophone is scanned through the field of the difference frequency in both the axial and radial directions.[xiii] In this experiment, the measurement points spanned the area: $11cm <$ axial range $< 52.5cm$ and $-6cm <$ radial range $< 6cm$ with a step size of $5mm / step$ in either dimension. The driving frequency generator (Wavetek model 395, Fluke, Everett, WA) modulated the carrier frequency of 2.7 MHz by 50 kHz using the suppressed carrier modulation mode (SCM). The signal was recorded using a low frequency hydrophone (International Transducer Corporation ITC-6080C, Santa Barbara, CA) and registered to an oscilloscope (Yokogawa DL7100, Japan), which acquired the average over 8 sequential measurements. Then, this average signal was filtered with a digital filter (Stanford Research Systems SR650, Sunnyvale, CA), which was set to notch filter from 48.5 – 51.5 kHz. The final processed signal was recorded to a personal computer via a IEEE-488 GPIB connection.

[xiii] Although attempts were made to use a PVDF needle hydrophone (Precision Acoustics, Dorchester, UK) to measure the difference frequency field, the measurements proved unreliable because the needle hydrophone device is neither calibrated nor designed to measure frequencies at 50 kHz and below.

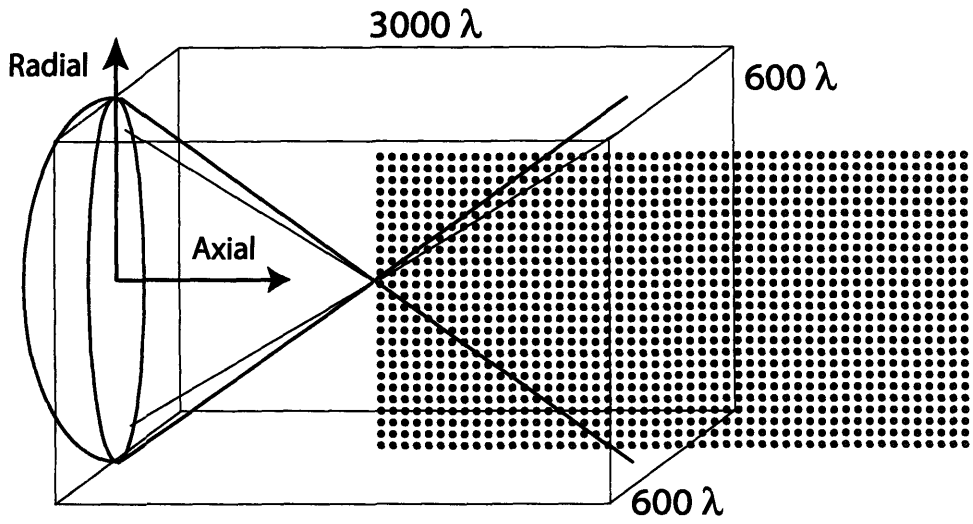


**Figure 3-8:** Diagram of the experiment for measuring the field of a parametric array. In this experiment, the hydrophone was scanned through a plane of measurement points to record the difference frequency field produced by a parametric array. The small circles indicate the points at which measurements were acquired with the low frequency hydrophone.

The experimental results are displayed in Figure 3-9. The plotted data represents the amplitude of the measured difference frequency signal in the units of Pa as a function of axial and radial position in the measured field. The results demonstrate that the measured difference frequency field has an axial distribution that gradually reaches a maximum at approximately 25 *cm* from the transducer surface. This axial distribution was illustrated previously in Figure 3-7. In the radial direction, the results demonstrate a broad difference frequency pressure distribution measuring approximately 6 cm across at the –3 dB drop-off.

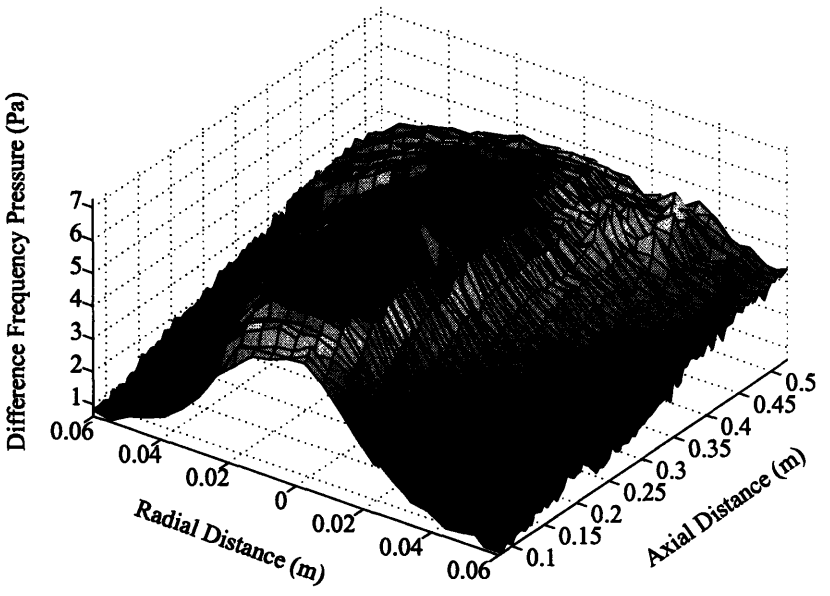


**Figure 3-9:** Experimental measurement of the difference frequency field from a focused parametric array. The field was measured with a low frequency hydrophone scanned in the axial direction from .1 m (focal plane) to .5 m and in the radial direction from -.06 m to .06 m.

## 3.2 The Parametric Effect

The parametric effect is a result of sound from one transducer scattering from another transducer driven at a slightly different frequency. This produces two collinear fields at slightly different frequencies that generate nonlinear sum and difference frequency fields in a manner similar to a parametric array. In this section, a dual frequency imaging system with separate elements is used to study the difference frequency sound generation due to the parametric effect. A theoretical model is presented together with results from simulations and experiments that illustrate the relatively large difference frequency signal produced by the parametric effect as compared to the undetectable difference frequency production due to local difference frequency pressures presented in chapter 4.

There is a rich body of literature pertaining to the generation of sum and difference frequency fields in acoustics[46,48,49,58,60,61,66,68,75,107,114-117]. The plethora of possible sources of nonlinear sound generation makes it difficult to determine the exact source of sum and difference frequency sound. The nonlinear effects which might produce difference frequency sound, as proposed by several groups, include the collinear interaction of the incident field[42], pseudo-sound effects at the hydrophone itself[47], nonlinear scattering effects[52], and dual-frequency radiation force effects[40].

Despite advances in the imaging technique with the USVA method achieved by others and in our laboratory[2,4,25-30,40,118-122], we found experiments with the dual-frequency system difficult to repeat. In addition, our results often demonstrated a response signal that was sensitive to the geometry and orientation of the target. In response to these observations, we consider the hypothesis that perhaps a previously unconsidered source of difference frequency generation in the USVA system, the parametric effect of the reflected field, may contribute to the difference frequency field for the USVA method.

This chapter examines the conditions under which the parametric effect of the reflected field may contribute significantly to the nonlinear difference frequency field both through simulation and experimental verification of the simulations. The theoretical section provides a model for the multiple reflections needed to create the parametric effect. We then simulate that model to predict the resulting levels of the difference frequency field generated by the parametric effect. The experiments in this section are designed to limit some of the aberrant sources of nonlinear sound generation in order to concentrate only on the parametric effect. While the system used is similar to the dual-frequency imaging system proposed by Fatemi and Greenleaf, there are important differences including the use of two separate transducer elements arranged at a large angle to one another, the use of short pulsed waveforms rather than CW, and the addition of a dual-directional coupler in order to measure reflected power from one element onto the other element. These differences are designed to isolate the parametric effect for this study.

### *3.2.1 Theory of Parametric Effect*

The parametric effect as described by Westervelt[93] is simply the creation of a parametric array by means of the reflection of a field at one frequency from a transducer generating a field at another frequency. After this reflection, the two fields act collinearly to produce difference frequency sound according to the second-order wave equation in a manner similar to the parametric array described above. For the case of the dual-frequency imaging system, the proposed parametric effect is complicated by the introduction of a target at the focus of the two transducers (Figure 3-10). This target provides a surface for reflecting the incident field back to the transducers and allows for a parametric effect despite the fact that the elements are directed away from one another initially. The diagram of this effect, as well as the theoretical description of the effect found in this section, account for only the action of one element on the other. However, it is important to note that the parametric effect occurs simultaneously on both elements such that each will generate a difference frequency field.

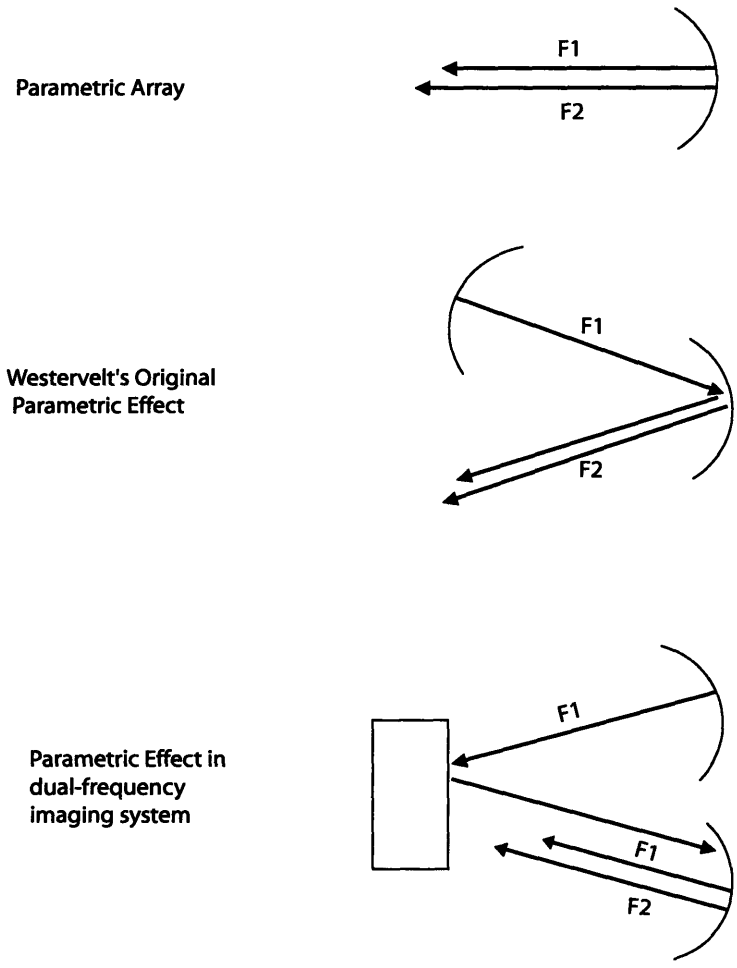


**Figure 3-10:** Diagram illustrating the parametric array, Westervelt's original parametric effect, and the parametric effect in the dual-frequency imaging system.

In this section, we formulate a mathematical description of the interaction of the two beams in a manner that will produce a difference frequency field due to the parametric effect. Our method makes reasonable approximations in calculating the total reflected field of one element from an interface and back onto the other element. First, we model the planar reflection of the incident primary field from the interface of a stratified medium to calculate the reflected field from the target of finite thickness. Then, we calculate the field after a second reflection from the spherical surface of the second transducer. For this second reflection we use a method involving the spherical harmonic decomposition of the incident field. Finally, we use the result of this reflected field in the parametric array simulation described in equation (0.32) in order to calculate the generation of the difference frequency field.

*Planar Reflection*

Figure 3-11 illustrates the interaction of the acoustic fields from two transducers with the interface of a planar target.

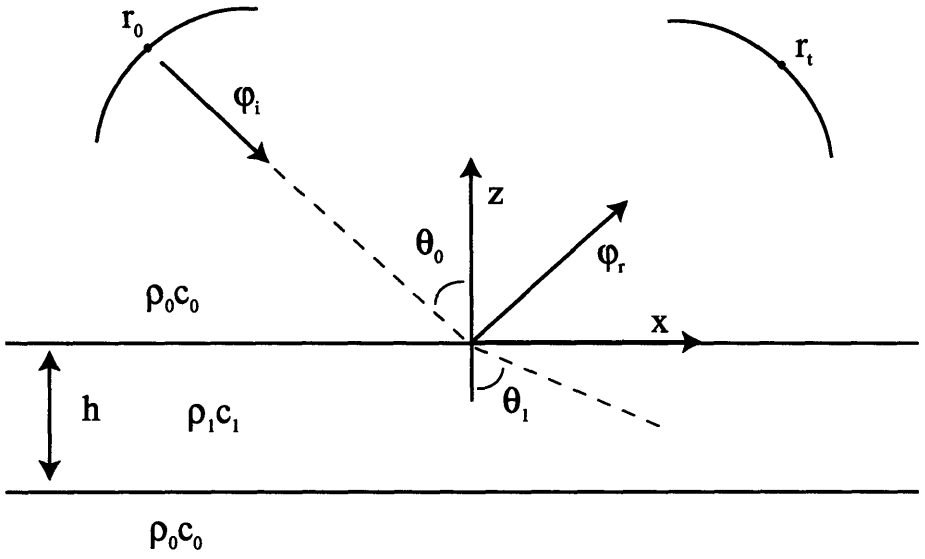


**Figure 3-11:** Diagram of the model of reflection from a horizontally stratified planar interface.

The total incident field from a focused transducer can be decomposed into the "local plane-wave spectrum" as described by Korpel[112] and Ludwig[113] so that we may analyze the planar reflection of each component individually. Taking the 2D-spatial Fourier Transform over all points in space where there is a nonzero incident pressure $P_i$, we can solve for each incident plane wave component $\varphi_i(k_x,k_y)$ of the total incident field at the interface with the planar boundary,

$$\varphi_i(k_{ix},k_{iy};z=0)=\int_{-\infty}^{\infty}\int_{-\infty}^{\infty}P(x,y,0)e^{-j(k_{ix}x+k_{iy}y)}dxdy \tag{0.33}$$

where the wave vector amplitude $k=|\mathbf{k}|=\sqrt{k_x^2+k_y^2+k_z^2}=\frac{2\pi}{\lambda}$ and $\varphi_i(k_x,k_y;z=0)$ is an incident plane wave at $z=0$ traveling in the direction of the unit vector $\frac{\mathbf{k}}{|\mathbf{k}|}$.

Given a plane wave $\varphi_i(k_x,k_y)$ incident on a planar boundary and a reflection coefficient $R(k_x,k_y)$, the reflected plane wave is expressed as $\varphi_r = R\varphi_i$. Likewise, by taking the inverse

Fourier Transform over all wave-vectors $(k_x, k_y)$, we can find the total reflected field $P_r(\mathbf{r})$ at position $\mathbf{r} = (x, y, z = 0)$ resulting from the reflection of all incident plane waves from a horizontally stratified surface,

$$P_r(\mathbf{r}) = \frac{1}{(2\pi)^2} \int_{-\infty}^{\infty} \int_{-\infty}^{\infty} R(k_x, k_y) \varphi_i(k_x, k_y; z = 0) e^{j\mathbf{k}\cdot\mathbf{r}} dk_x dk_y \tag{0.34}$$

where $R(k_x, k_y)$ is the K-space reflection coefficient from a horizontally stratified medium[123],

$$R(k_x, k_y) = \frac{R_{01} + R_{10} e^{2jk_1 h \cos\theta_1}}{1 + R_{01} R_{10} e^{2jk_1 h \cos\theta_1}}, \tag{0.35}$$

$k_1 = \frac{\omega}{c_1}$, and $R_{01}$ is the real-space reflection coefficient given by,

$$R_{01} = \frac{m_0 \cos\theta_0 - \sqrt{n_0^2 - \sin^2\theta_0}}{m_0 \cos\theta_0 + \sqrt{n_0^2 - \sin^2\theta_0}}$$

$$(\text{where } m_0 = \tfrac{\rho_1}{\rho_0} \text{ and } n_0 = \tfrac{k_1}{k_0}) \tag{0.36}$$

Similarly, $R_{01}$ is the real-space reflection coefficient given by,

$$R_{10} = \frac{m_1 \cos\theta_1 - \sqrt{n_1^2 - \sin^2\theta_1}}{m_1 \cos\theta_1 + \sqrt{n_1^2 - \sin^2\theta_1}}$$

$$(\text{where } m_1 = \tfrac{\rho_0}{\rho_1} \text{ and } n_1 = \tfrac{k_0}{k_1}) \tag{0.37}$$

*Spherical Reflection*

Equation (0.34) describes the total reflected field from a horizontally stratified surface. Now, we are interested in describing the second reflection of the field from a spherical cap (Figure 3-12). First, we express each planar wave component of $P_r(\mathbf{r})$ (corresponding to each value of $k_x$

and $k_y$ ) in terms of its spherical harmonics using a Bessel function plane wave expansion described by Stratton.[124]

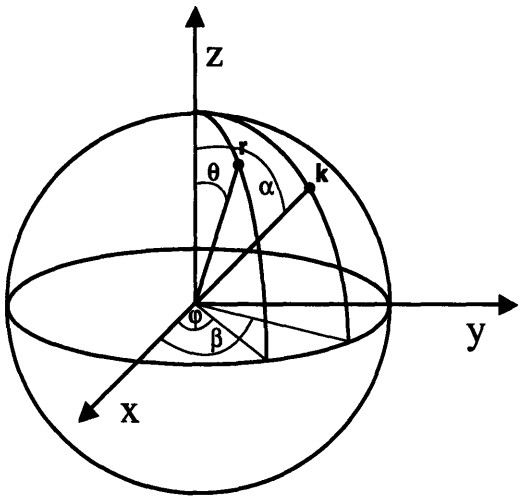


**Figure 3-12:** Diagram of the spherical coordinate system used for the spherical decomposition of plane waves.

The plane wave at an arbitrary position in space $\mathbf{r}$ propagating with the wave-vector $\mathbf{k}$ is written $e^{j\mathbf{k}\cdot\mathbf{r}}$, given wave-vector $\mathbf{k}=(k_x,k_y,k_z)=(k\sin\alpha\cos\beta,k\sin\alpha\sin\beta,k\cos\alpha)$ and an arbitrary observation point $\mathbf{r}=|\mathbf{r}|(\sin\theta\cos\varphi,\sin\theta\sin\varphi,\cos\theta)$. Note also that $\mathbf{k}\cdot\mathbf{r}=k|\mathbf{r}|\cos\gamma$. Further, the plane wave can be expressed as an infinite sum of spherical harmonics,

$$\begin{aligned} e^{i\mathbf{k}\cdot\mathbf{r}} &= e^{ik|\mathbf{r}|\cos\gamma} \\ &= \sum_{n=0}^{\infty} i^n(2n+1)j_n(k|\mathbf{r}|)P_n(\cos\gamma) \\ &= \sum_{n=0}^{\infty} i^n(2n+1)j_n(k|\mathbf{r}|)P_n\left(\tfrac{\mathbf{k}\cdot\mathbf{r}}{k|\mathbf{r}|}\right) \end{aligned} \tag{0.38}$$

where $P_n$ is the nth-order Legendre Polynomial, and $j_n$ is the nth-order spherical Bessel function (which should not be confused with the imaginary number $i=\sqrt{-1}$ ).[124]

After describing the reflected wave from the horizontal planar boundary in terms of spherical harmonic waves incident on the spherical cap, we can assume the form for the reflected wave from the spherical cap. Given an incoming wave $P_i$ of the form,

$$P_i = \sum_n A_n j_n(k|\mathbf{r}|) \tag{0.39}$$

where $A_n = i^n(2n+1)P_n\left(\frac{\mathbf{k}\cdot\mathbf{r}}{k|\mathbf{r}|}\right)$, we assume that the outward reflected spherical wave $P_R$ from the spherical cap is also spherical and of the form,[113,125]

$$P_R = \sum_n R_n A_n h_n^{(2)}(kR_t) \tag{0.40}$$

where $R_n$ is the $n^{th}$ order reflection coefficient for the spherical cap. Further, we assume that the transmitted wave through the spherical cap $P_T$ has the form,

$$P_T = \sum_n T_n A_n(\theta,\varphi) j_n(kR_t) \tag{0.41}$$

where $T_n$ is the $n^{th}$ order transmission coefficient for the spherical cap.
Then it is a relatively easy matter to impose the conditions of continuity of pressure (0.42) and velocity (0.43),

$$P_i + P_R = P_T \tag{0.42}$$

$$\frac{1}{\rho_w}\frac{\partial}{\partial \mathbf{r}}(P_i + P_R) = \frac{1}{\rho_t}\frac{\partial}{\partial \mathbf{r}}(P_T) \tag{0.43}$$

at the water/second transducer interface $|\mathbf{r}| = a$ in order to solve for the coefficient of interest, $R_n$ (where $a$ is the radius of curvature of the transducer, $\rho_w = 998kg/m^3, \rho_t = 10{,}000kg/m^3$ are the densities of the water and transducer material respectively). Note that we chose arbitrarily large value for the density of the transducer simply to ensure a large impedance mismatch and therefore nearly perfect reflection of the incident field from this surface.

Substitution of expressions for $P_i, P_R$, and $P_T$ (equations (0.39) - (0.41) ) into these constraints yields the system of two equations with two unknowns $R_n$ and $T_n$,

$$\begin{aligned} j_n(ka) + R_n h_n^{(2)}(ka) &= T_n j_n(ka) \\ \dot{j}_n(ka) + R_n \dot{h}_n^{(2)}(ka) &= T_n \dot{j}_n(ka) \end{aligned} \tag{0.44}$$

This system of equations can be written in matrix form as

$$\begin{bmatrix} j_n(ka) \\ j_n(ka) \end{bmatrix} = \begin{bmatrix} -h_n^{(2)}(ka) & j_n(ka) \\ -\dot{h}_n^{(2)}(ka) & \frac{\rho_w}{\rho_t}\dot{j}_n(ka) \end{bmatrix} \begin{bmatrix} R_n \\ T_n \end{bmatrix} \tag{0.45}$$

Solving by Crammer's Rule results in the system,

$$\begin{bmatrix} R_n \\ T_n \end{bmatrix} = \frac{\begin{bmatrix} \frac{\rho_w}{\rho_t}\dot{j}_n(ka) & -j_n(ka) \\ \dot{h}_n^{(2)}(ka) & -h_n^{(2)}(ka) \end{bmatrix}}{-\frac{\rho_w}{\rho_t}h_n^{(2)}(ka)\dot{j}_n(ka) + \dot{h}_n^{(2)}(ka)j_n(ka)} \begin{bmatrix} j_n(ka) \\ j_n(ka) \end{bmatrix} \tag{0.46}$$

and solving for $R_n$ explicitly gives the result for the reflection coefficient,

$$R_n = \frac{(\frac{\rho_w}{\rho_t} - 1)\dot{j}_n(ka)j_n(ka)}{-\frac{\rho_w}{\rho_t}h_n^{(2)}(ka)\dot{j}_n(ka) + \dot{h}_n^{(2)}(ka)j_n(ka)} \tag{0.47}$$

Now, combining the expression for the incident pressure, $P_i$, and the reflected pressure from the second transducer, $P_R$, we get the total pressure, $P_{IR}$,

$$\begin{aligned} P_{IR}(\mathbf{r}) &= P_i + P_R \\ &= \sum_n A_n(\theta,\varphi)P_n\left(\tfrac{\mathbf{k}\cdot\mathbf{r}}{kR_t}\right)\left[j_n(kR_t) + R_n h_n^{(2)}(kR_t)\right] \\ &= \sum_{n=0}^{\infty} i^n(2n+1)P_n\left(\tfrac{\mathbf{k}\cdot\mathbf{r}}{kR_t}\right)\left[j_n(kR_t) + R_n h_n^{(2)}(kR_t)\right] \end{aligned} \tag{0.48}$$

This pressure field is the sum of incident waves scattered from a horizontally stratified medium as well as these scattered waves after reflecting from the second transducer. In practice, and for the simulations performed in the next section, only the reflected field from the transducer cap, $P_R$, is considered in calculations of the parametric effect since these waves are traveling collinearly with the other primary field and thereby contribute significantly to the difference frequency field. The term $P_{IR}$ represents the pressure due to a single directional plane wave after

multiple reflections. The expression for the total pressure over all plane wave directions can be written by taking the inverse Fourier transform of $P_{IR}$ over all k-space. The result for the total reflected field, $P_{Total}$, is given by,

$$P_{total}(\mathbf{r}) = \frac{1}{(2\pi)^2} \int_{-\infty}^{\infty} \int_{-\infty}^{\infty} R_n(k_x, k_y) \varphi_i \sum_{n=0}^{\infty} i^n (2n+1) P_n\left(\frac{\mathbf{k}\cdot\mathbf{r}}{k|\mathbf{r}|}\right) \left[ j_n(k|\mathbf{r}|) + R_n h_n^{(2)}(k|\mathbf{r}|) \right] dk_x dk_y \qquad (0.49)$$

The entire field in space at both primary frequencies can be determined by adding this total reflected field, $P_{total}(\mathbf{r})$, at the frequency $\omega_A$ to the field radiating from the second transducer at a slightly different frequency, $\omega_B$. The summed field from both elements can be used in the source term of the second-order wave equation (0.24) to solve for the resulting difference frequency generation due to the parametric effect using either the volume integral or approximate solution methods outlined previously is section 3.1.2.

### *3.2.2 Simulation of Parametric Effect*

The simulation was performed in the Matlab® programming environment running on a personal computer with a 2 GHz Pentium processor and 1 GB of RAM. Table 1-4 details the parameters for the speed of sound and density for the silicone gel used in the simulation. In the simulation, the total pressure from one transducer is first reflected from the silicone gel and then from the 2nd transducer. The resulting field after both reflections is then used in the approximate solution to the nonlinear wave equation (0.32) to calculate the difference frequency pressure at the focus of the second element. The value for the amplitude of the difference frequency pressure is calculated as a function of rotation angle of the silicone gel tissue phantom (Figure 3-13). In addition to calculating the difference frequency pressure at the focus, we calculate the total incident power on the second transducer from the first transducer in order to quantify the energy incident on the second element. We call this quantity the "Reflected Power" because it corresponds to power reflected from the interface of the silicone gel. In addition, in experimental measurements, this quantity is proportional to the "Reflected Power" measured by a dual-directional coupler placed between the driving amplifier and the transducer.

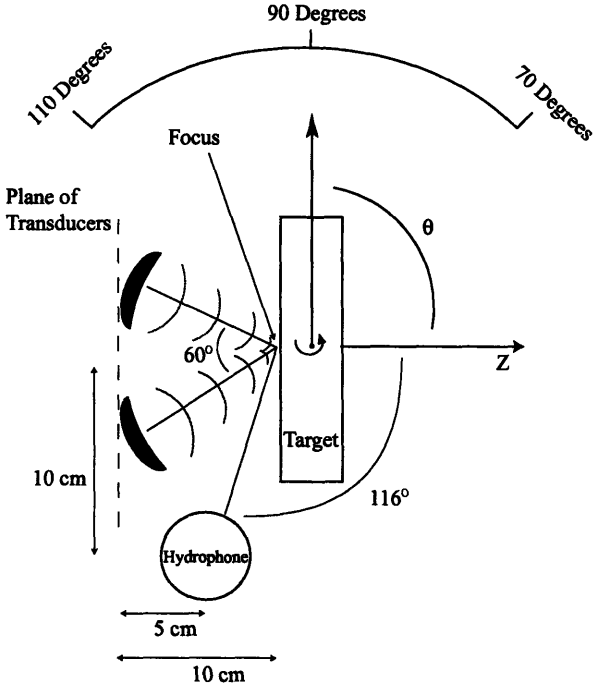


**Figure 3-13:** Diagram of the geometry of the simulation and experiment used for rotational scans of a silicone gel tissue phantom.

The simulation and experimental results for the reflected power are plotted in the left pane of Figure 3-14. This plot demonstrates a reasonable correlation between the simulation and experiment. The reflected power is normalized because the dual-directional coupler set-up is not calibrated and therefore the experimental value is not an absolute power measurement. The simulation and experimental result are similar in the shape of the angular distribution of the values. They both demonstrate a peak reflected power at 90 degrees rotation. This rotation corresponds to the silicone gel surface oriented parallel to the plane of the transducers (see Figure 3-13). The simulation and experimental results for the difference frequency are plotted in the right pane of Figure 3-14. We plot the absolute pressure measured with the low frequency hydrophone (International Transducer Corporation ITC-6080C, Santa Barbara, CA) to illustrate the correlation of the simulation and experimental levels at the difference frequency. The simulation agrees reasonably well with the levels measured experimentally and demonstrates a similar angular dependence. However, the simulation does not capture the sharp variations in amplitude as a function of angle, which we observe in the experiment. Relatively large standard deviations accompany these fluctuations, which may simply represent the sensitivity of the system to slight motions of the interface. Additionally, the difference frequency field may interact with the silicone

gel, the hydrophone, or the tank to produce the sharp variations. These interactions are not modeled in the simulation.

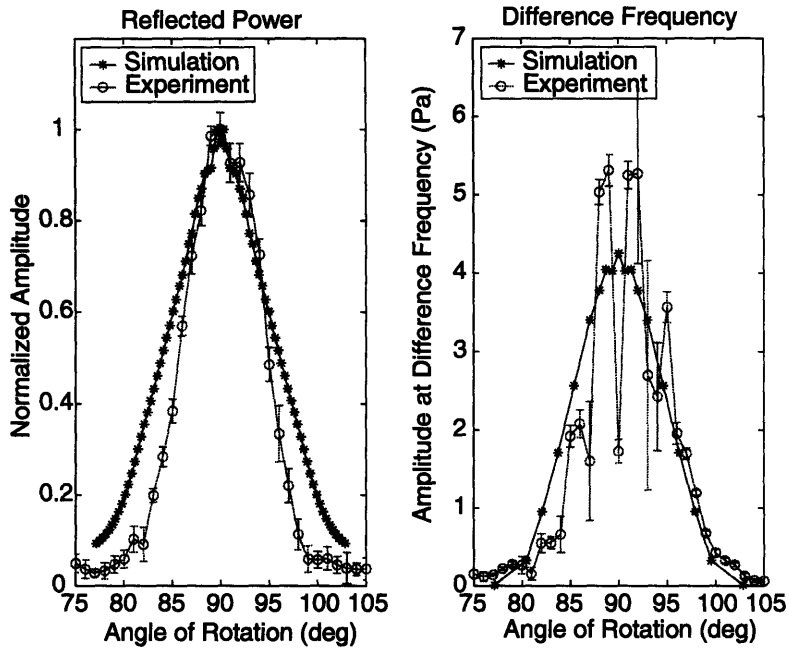


**Figure 3-14:** Simulation vs. experimental results for the parametric effect. The reflected power signal (at the primary frequency of one element as received at the other element) (left) and the generated difference frequency sound (right) are plotted as a function of the angle of rotation of the silicone gel tissue phantom.

For both the reflected power and the difference frequency plots of Figure 3-14, we note that the angle of rotation over which an appreciable signal is simulated or experimentally measured spans approximately 23 degrees. This value corresponds to the aperture of the elements given a diameter of 4 cm diameter and radius of curvature of 10 cm (see Figure 3-15). The 23-degree range of angles over which a difference frequency signal is produced makes sense intuitively because at angles larger than 102 degrees or smaller than 79 degrees, the field from one element will no longer be incident upon the second element (see Figure 3-13).

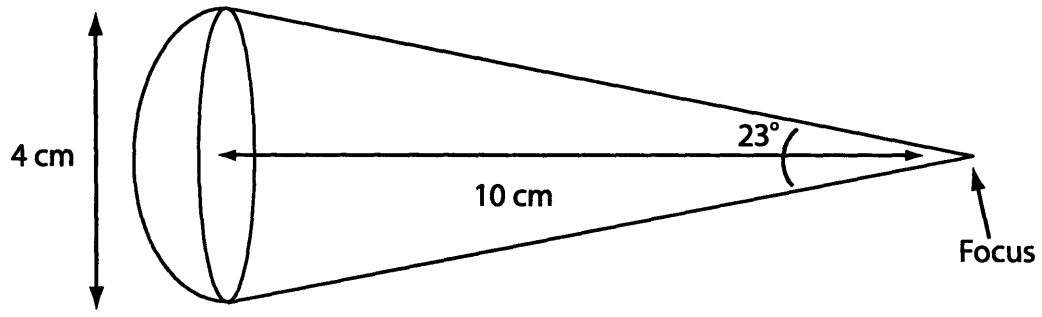


**Figure 3-15:** Diagram detailing the geometry of a single element of the dual-frequency system.

## *3.2.3 Experiments*

We demonstrate the generation of difference frequency sound in a series of experiments of increasing complexity designed to approximate tissue imaging with a dual frequency system. In the first set of basic experiments similar to those performed by Westervelt[102], we compare the difference frequency signal from a single element driven as a parametric array to the difference frequency signal from two elements driven at their primary frequencies and positioned such that their fields exactly reflect from each other. This experiment, diagramed in Figure 3-16, compares the field generated by the parametric array vs. the field generated by the parametric effect. In the next set of experiments, we demonstrate the dependence of the difference frequency sound generation on the geometry of a planar target by focusing the two elements on a rigid polyethylene plate that is translated and rotated in space. Next, we illustrate the parametric effect resulting from a soft interface by replacing the polyethylene plate with a tissue phantom made from silicone gel. Finally, we form an image in *ex vivo* rabbit liver at a difference frequency sound level and geometry consistent with the parametric effect.

### *Materials and Methods*

We conducted all experiments in a tank of degassed, de-ionized water lined with acoustic absorbing rubber. In addition, the tank was encased on the bottom and four sides by a 2" thick acoustical foam rubber for absorbing environmental noises. We fabricated the air-backed, spherically focused transducers in-house from PZT4 to the specification of 10 cm radius of curvature and 4 cm diameter. We mounted the elements at an angle to one another (60 degrees) so that their foci intersected at 10cm from either element (see Figure 3-13). This set-up varies slightly from the USVA system described previously in the literature.[24] In this set-up, the two elements are separated physically at a considerable angle from one another to eliminate the effects of collinear sound waves incident on the target which may combine nonlinear to produce difference frequency

fields as described by Calle[42]. The elements were electrically matched with separate inductor/capacitor circuitry to both their 3rd (1.624 MHz) and 5th harmonic (2.73 MHz) and driven by either a custom built 2-channel amplifier (Advanced Surgical Systems, UDS04PF-CSA, Arizona) or by ENI RF amplifiers (ENI2100L and ENIA150, Rochester, NY) with the signal generated by HP function generators (Hewlett-Packard HP33120A, Palo Alto, CA). The target was positioned in the experimental tank with a Velmex 3-axis motor controlled positioning system (Velmex Unislide NF90, Bloomfield, NY) and a manual rotational axis (Velmex, Bloomfield, NY). The low frequency signal was detected in the tank with a low frequency hydrophone (International Transducer Corporation ITC-6080C, Santa Barbara, CA), filtered with a dual channel filter (Stanford Research Systems SR650, Sunnyvale, CA), and digitized by a digital oscilloscope (Yokogawa DL7100, Japan).

In addition to the difference frequency signal measured by the hydrophone, we measured the forward and reflected power from one element via a dual directional coupler placed between the amplifier output and the matching circuitry of the transducer. This signal was unfiltered and digitized by the same Yokogawa oscilloscope as used for the low frequency hydrophone signal. The dual directional coupler signal, when analyzed in the Fourier domain, reveals the effect of one element (which is at a different primary frequency) on the other through the reflection of power from the target. The entire set-up was coordinated with the Instrument control Toolbox in Matlab® (ver. 6) using RS232 and GPIB computer control to move the positioner, specify the output timing and power levels to each element, and acquire the signals from the oscilloscope.

*Parametric Array vs. Parametric Effect*

This experiment shows the equivalent interaction of two fields when driving one element at two frequencies as a parametric array or driving them both at their primaries and pointing them at one another to create the parametric effect. Two elements are positioned facing each other in a tank of degassed water and aligned to share a common focus at the midpoint between them. First, both elements are driven at their primary frequencies (2.74 MHz), plus or minus a range of difference frequencies from 1-65 kHz. Then one element is turned off and the other is driven as a parametric array (at two frequencies simultaneously) using the carrier suppressed AM mode on the function generator. Each element was driven continuous wave (CW) at a time-averaged power of 5 W electrical as measured by an inline power meter (Agilent Technologies E4419B, Palo Alto, CA). The power level corresponded to a peak acoustic pressure of 1.5 MPa at the focus of the primary field. The signal was received by the low frequency hydrophone positioned off to the side of the two transducers, filtered from 5-65 kHz with 0dB gain, registered to the digital oscilloscope and

then recorded by personal computer via a GPIB-IEEE488 communications connection. The set-up is illustrated in Figure 3-16.

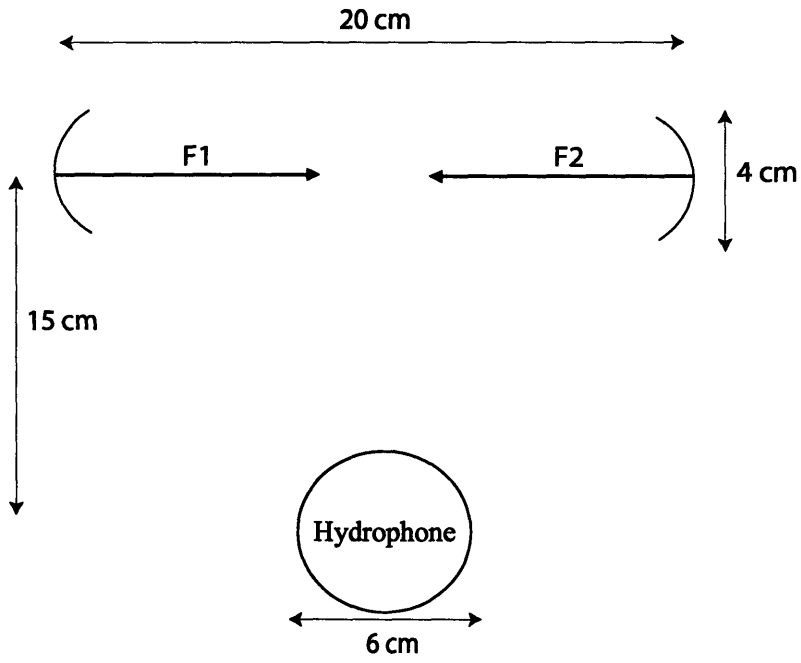


**Figure 3-16:** Diagram of the set-up for an experiment designed to compare the parametric array with the parametric effect.

The results of this experiment for the difference frequency of 50 kHz are plotted in Figure 3-17. This result demonstrates that the difference frequency pressures recorded at the hydrophone for the parametric array (top plot of Figure 3-17) and the parametric effect (bottom plot of Figure 3-17) achieve similar amplitudes. We observe that for both cases, the response signal at the difference frequency is approximately 4 Pa in amplitude and well differentiated from the background noise. This observation supports the hypothesis that the mechanism of generating the difference frequency is similar in the two cases. Technically, the parametric array experiment may be described as a parametric array with a reflector, because the field from the parametric array may reflect from the other transducer, which is not powered but positioned 20 cm away. To determine the significance of the presence of the second element, we repeated the parametric array experiment after removing the second element from the tank. The result was similar to those plotted in Figure 3-17 but the amplitude of the difference frequency signal was slightly lower reaching approximately 2 Pa of peak pressure. However, for the comparison of the parametric array with the parametric effect, we include the parametric array results with the second element in the tank to control for the

interaction of difference frequency waves with the second element, which may occur in either scenario.

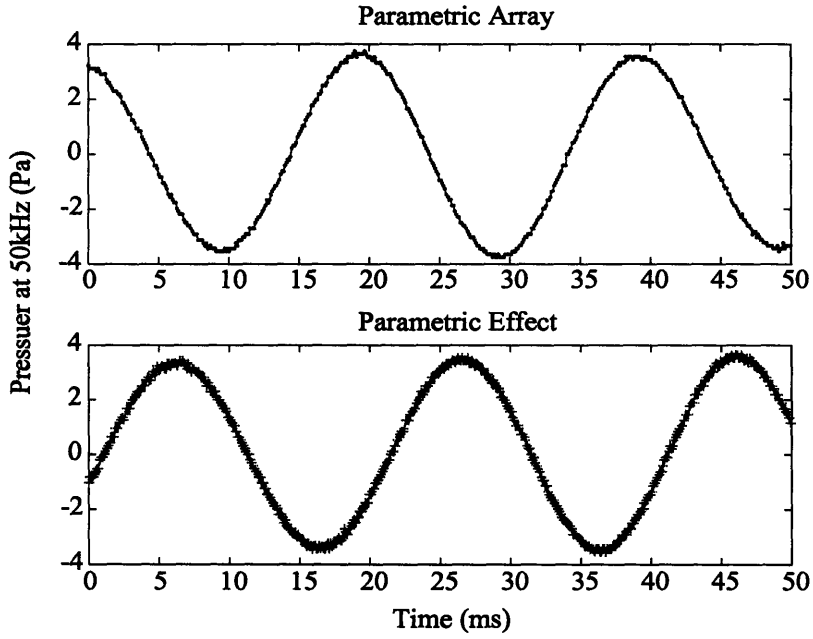


**Figure 3-17:** Experimental result comparing the parametric array and parametric effect. The plot shows the difference frequency signal (50kHz) as a function of time produced by a single element driven as a parametric array (top) and by two elements facing one anther to produce a parametric effect (bottom).

In addition to the results at a difference frequency of 50 kHz, the response was recorded at several other difference frequencies to demonstrate the comparable magnitudes of the response for the two methods of driving the elements. The responses, plotted as a function of difference frequency in Figure 3-18, demonstrate a similar frequency dependence for both driving methods. The frequency dependence illustrates a general increase in amplitude with increasing difference frequency as well as sudden smaller drops in amplitude at particular difference frequencies. The important result of this experiment is that a difference frequency signal at comparable levels is recorded for the parametric array and the parametric effect, suggesting that the mechanism of difference frequency signal generation is related for these two driving methods. The results also serve to set a relative order of magnitude for the generation of difference frequency sound via the parametric effect on the order of 1-10 Pa for driving powers of 5-10 W electrical per element (1.5 – 2 MPa peak pressure at the focus of each primary field). With few exceptions, this relatively limited range of driving powers is used throughout the thesis.

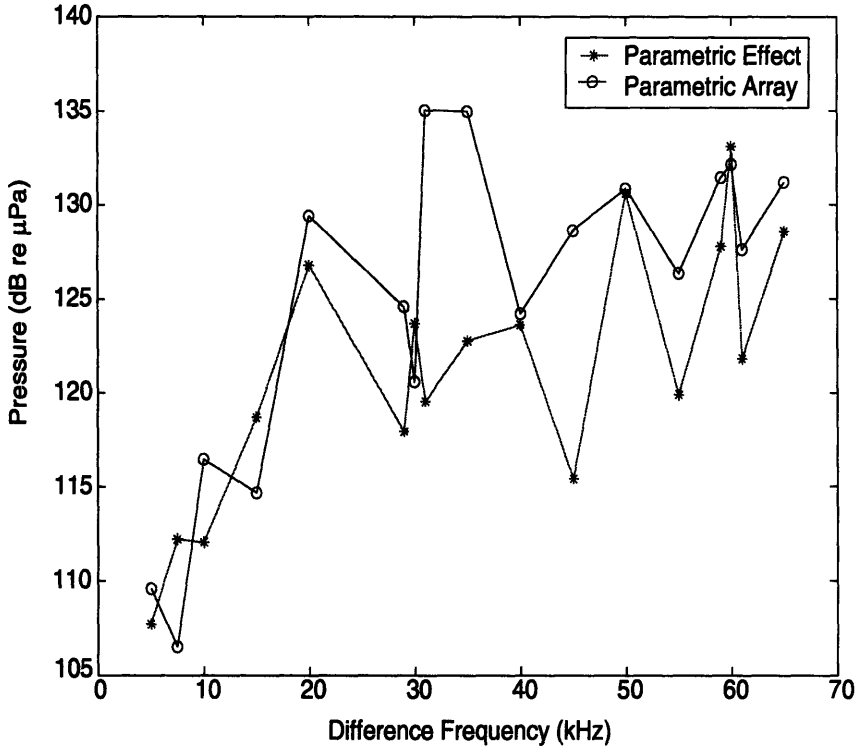


**Figure 3-18:** Experimental result comparing the parametric array and parametric effect as a function of frequency. The plot shows the difference frequency signal produced by a single element driven as a parametric array and by two elements interacting to produce a parametric effect for a range of difference frequencies.

### *Rotational Scans and Axial Scans of an Polyethylene Plate and a Silicone Gel*

In the dual-frequency system, the parametric effect is achieved through the reflection from a planar boundary as described in section 3.2.1. This reflection suggests that the difference frequency response may be sensitive to the angle of rotation of the planar boundary. Independently, we observed in experiments that the amplitude of the difference frequency response was sensitive to the orientation of the target with respect to the transducers. In order to quantify this relationship, we conducted several experiments with a polyethylene plate (measuring 10.5 cm x 10.5 cm x 1.1 cm) and with a silicone gel tissue phantom (11 cm diameter circular slab, 2.8 cm thick) to demonstrate the angular dependence of the difference frequency response. For the rotational scans, the focus of the acoustic pressure field was positioned at the front surface of the target and the target was rotated by 1 degree steps starting from 70 and ending at 110 degrees, where 90 degrees is perfectly parallel to the plane of the transducers (see Figure 3-19). At each angular position, the two transducers

pulsed at a power of 10 W (corresponding to a peak pressure of 2 MPa for each primary field) electrical per element and at a difference frequency of 30 kHz with a period of 75 msec and a duty cycle of 20%. The acoustic response was recorded by the low frequency hydrophone and the signal was captured and digitized by the oscilloscope. The measurements were repeated for a total of ten pulses at each angular position. In addition to measuring the low frequency field in the tank, we recorded the forward and reflected power signals from one of the transducer elements using the dual-directional coupler.

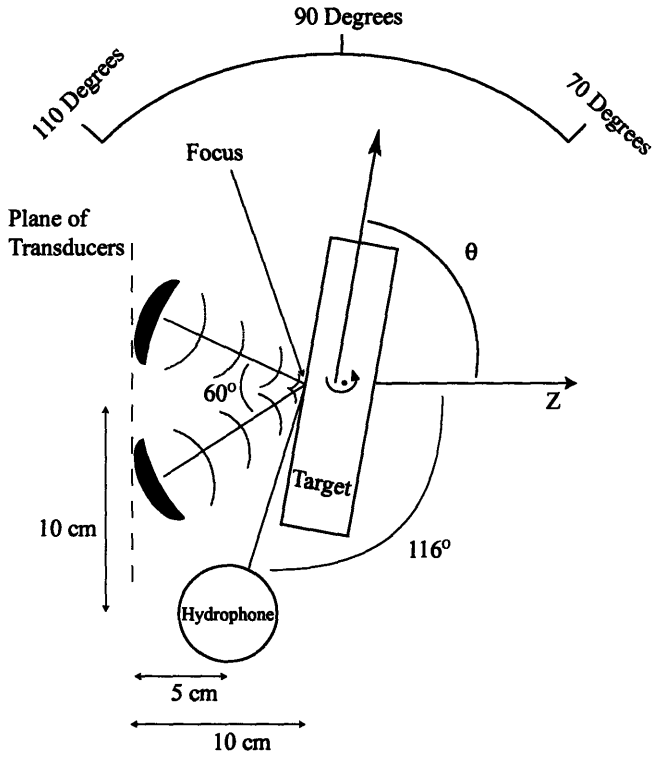


**Figure 3-19:** Diagram of the set-up used for rotational scan experiments with the silicone gel tissue phantom and the polyethylene plate.

The results of the rotational scans are very similar for the polyethylene plate (Figure 3-20) and the silicone gel tissue phantom (Figure 3-21). Results from both scans demonstrate a significant difference frequency response (3.5-5.5 Pa) from the target near an angle of 90 degrees. The response decreases symmetrically when the target is rotated in either direction away from 90 degrees. At angles greater than 100 degrees or less than 75 degrees, the response drops to the established noise amplitude for these experiments of .1Pa. The amplitude of the difference frequency sound at 30 kHz is nearly the same amplitude as demonstrated in the first set of experiments involving the direct parametric interaction of the two fields (Figure 3-17).

In addition to measuring the difference frequency signal directly, we recorded the amplitude of the reflected power from one element and analyzed the frequency component of the reflected power signal corresponding to the output frequency of the other element. The magnitude of this frequency component of the reflected power measurement directly corresponds with the degree to which the field from one transducer is incident upon (and reflecting from) the other transducer. The amplitude of this reflected power signal varies with the angle of rotation of the target, in a manner similar to the difference frequency signal such that the generation of difference frequency corresponds with the reflected power of one element interacting with the other. This correlation between the reflected power signal and the difference frequency pressure is demonstrated in experiments (Figure 3-20 and Figure 3-21) and the simulation of the parametric effect (Figure 3-14), supporting the hypothesis that the parametric effect is responsible for the generation difference frequency sound.

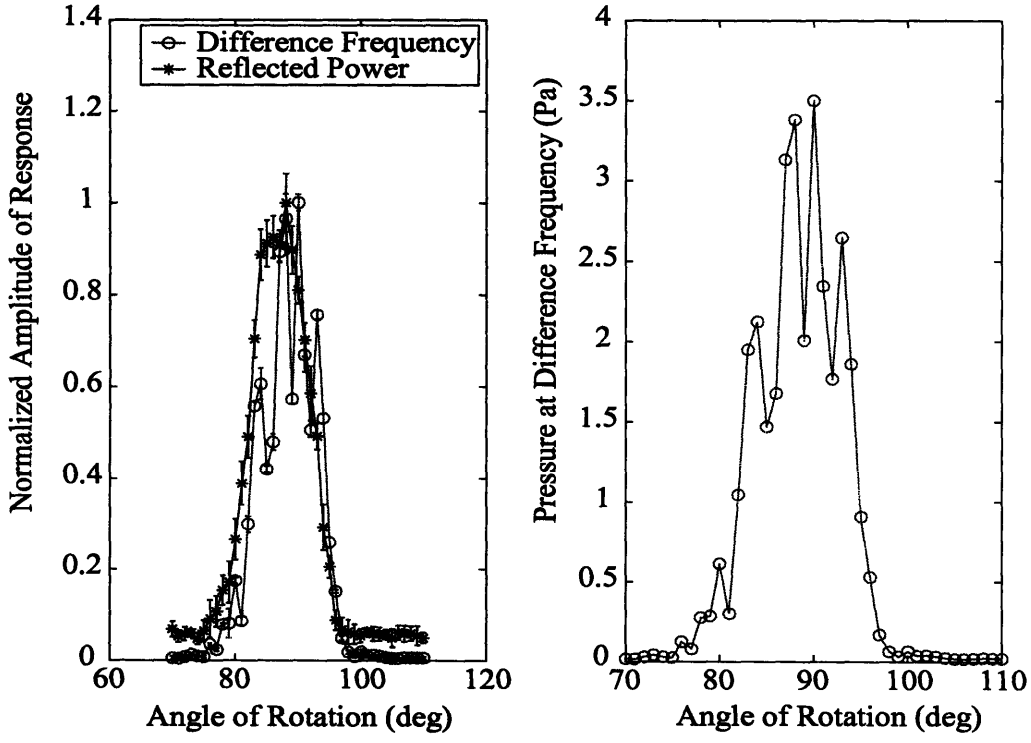


**Figure 3-20:** Experimental results for the rotational scan of a polyethylene plate with the focus of the dual frequency system positioned at the front interface. On the left, we plot the reflected power signal (at the primary frequency of one element as received at the other element) and the difference frequency signal normalized to their max values to demonstrate their correlation with each other and with the angle of rotation. On the right, we plot the difference frequency signal in the units of Pa to demonstrate the magnitude of the response as a function of the angle of rotation.

We repeated the rotational scans, replacing the polyethylene plate with the silicone gel tissue phantom (Figure 3-21) . The results demonstrate a difference frequency response that depends on the target rotation angle in a manner similar to the experiment with the polyethylene plate. Further, these experimental results correlate with the simulation results as presented in Figure 3-14. In the silicone gel tissue phantom experiment, the difference frequency levels are slightly greater than those produced with the polyethylene plate target. This result is not obvious since the silicone gel is much softer than the plate and one might imagine that the impedance match between the gel and water would be much closer than that of the plate and water. However, given the polyethylene plate properties of c = 1950 m/s, $\rho = 900$ kg/m$^3$ and the silicone tissue phantom properties of c = 1050 m/s, $\rho = 1000$ kg/m$^3$ and using equation (0.36), the reflection coefficient for a plane wave at a normal angle of incidence $\theta_o = 0$ is $|R| = .08$ for the plate and $|R| = .17$ for the silicone gel. Therefore, the silicone gel has a greater coefficient of reflection, which explains the slightly greater response from the gel than the plate as evident in careful inspection of Figure 3-20 as compared to Figure 3-21.

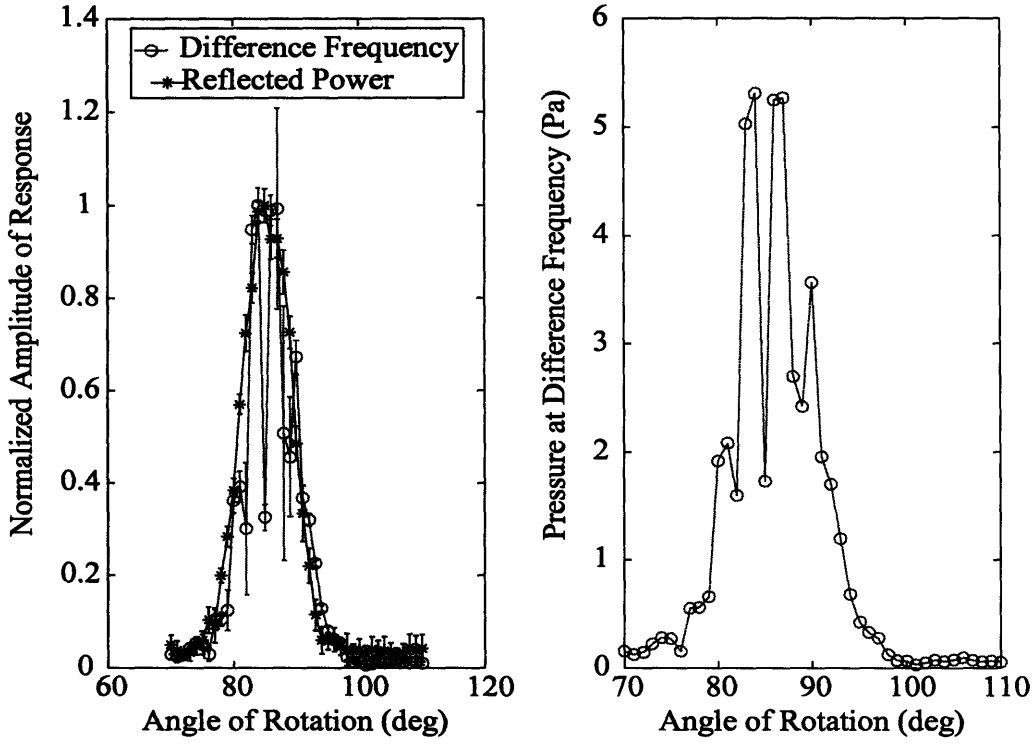


**Figure 3-21:** Experimental results for the rotational scan of a silicone gel tissue phantom with the focus of the dual frequency system positioned at the front interface. On the left, we plot the reflected power signal (at the primary frequency of one element as received at the other element) and the difference frequency signal normalized to their max values to demonstrate their correlation with each other and with the angle of rotation. On the right, we plot the difference frequency signal in the units of Pa to demonstrate the magnitude of the response as a function of the angle of rotation.

In experiments similar to the rotational scans, the silicone gel was scanned for 160 steps in the axial direction with a step size of .25 mm (Figure 3-22). In these axial scan experiments, we used a period of 880 msec with a duty cycle of 2%. The difference frequency was 30 kHz in both experiments with the primary frequency centered around 2.74 MHz for the first experiment (Figure 3-23) and 1.624 MHz for the second experiment (Figure 3-24). Each element was driven with 29 W electric power in the first experiment and 5 W electrical power in the second experiment, corresponding to a peak acoustic pressure at the focus for the primary fields of 3.5 MPa and 1.5 MPa respectively. Three measurements were recorded from both the low frequency hydrophone and the dual-directional coupler per location.

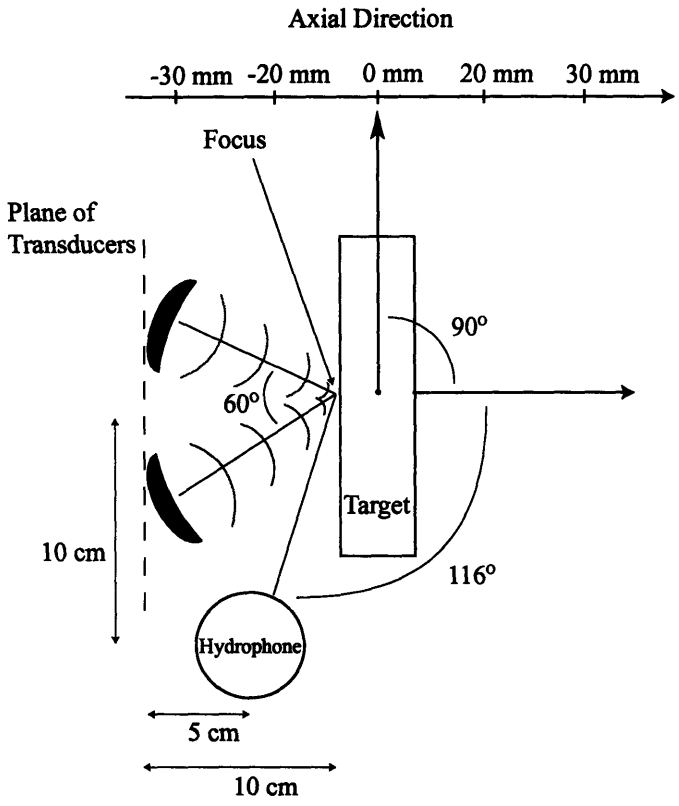


**Figure 3-22:** Diagram of the experimental set-up for axial scan experiments.

The experimental results of axial scans of the silicone tissue phantom support the conclusion that the parametric effect is responsible for the difference frequency sound generated in experiments with the transducers focused on a common target. For the axial scan experiments plotted in Figure 3-23 and Figure 3-24, there is relatively little recorded signal at the difference frequency except at the front and back interfaces of the gel, which are visible as the right-hand and left-hand peaks of the response respectively. The results of the first axial scan experiment plotted in Figure 3-23 show the response amplitude at the difference frequency from an axial scan in which a relatively large amplitude (29 W electrical, 3.5 MPa peak acoustic pressure at the focus of each primary field) pulse was sonicated from each element for a duration of 17 msec. This scan demonstrates prominent signals for both the difference frequency and the reflected power at the front and back interfaces of the gel, establishing a qualitative correlation between the generation of difference frequency signal and the reflection of one field onto the transducer forming the other field. The center of the gel and the water in front of and behind the gel produce almost zero signal at the difference frequency and likewise show almost no reflected power signal. We note that this correlation between the difference frequency signal and the reflected power signal is observed in the rotational scan experiments as well (Figure 3-20 and Figure 3-21).

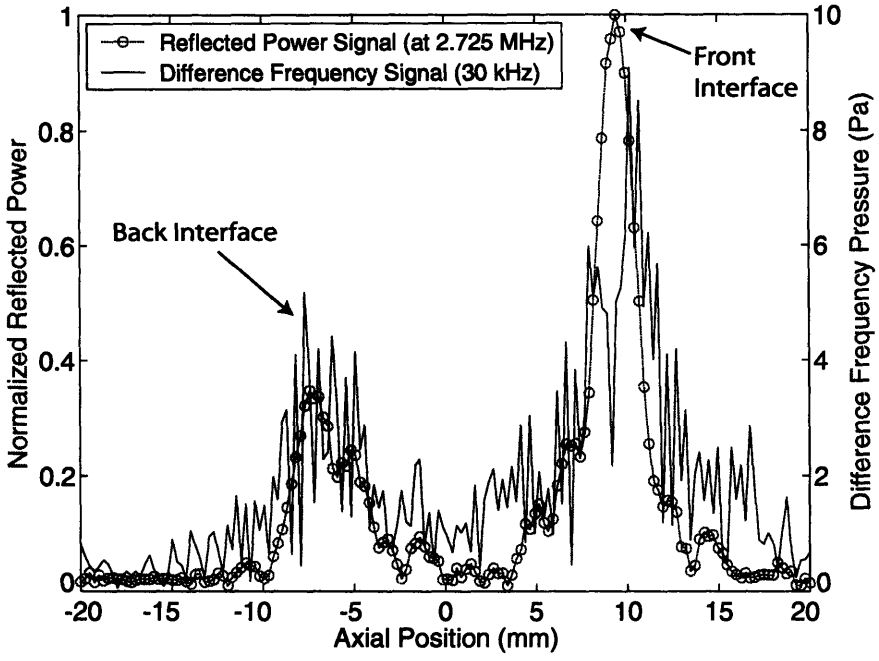


**Figure 3-23:** Experimental results for an axial scan through a silicone gel tissue phantom demonstrating the difference frequency sound generation and reflected power (at the primary frequency of one element as received at the other element) when the focus of the two beams is incident on the back and front interfaces of the target.

The second axial scan experiment (Figure 3-24) demonstrates the level of difference frequency signal encountered at the interfaces of the phantom when 5 W electrical driving power is used, corresponding to a peak acoustic pressure at the focus for the primary beam of 1.5 MPa. Here, the peak difference frequency response is 2.5 Pa which is the same order of magnitude for levels observed for the parametric effect in the experiments presented in Figure 3-17 as well as more complex rotational experiments presented below in Figure 3-21. The second axial scan also reveals that at the gel center, the recorded difference frequency signal is at the amplitude of the system noise in contrast to the larger signal observed at the target interfaces. This data supports the hypothesis that one reflected primary field is interacting with the field of the other primary signal and thereby creating a difference frequency field via the parametric effect because it illustrates that difference frequency responses are only generated when the primary beams are focused at the planar interface of a target which is positioned at the specular angle to the two transducers.

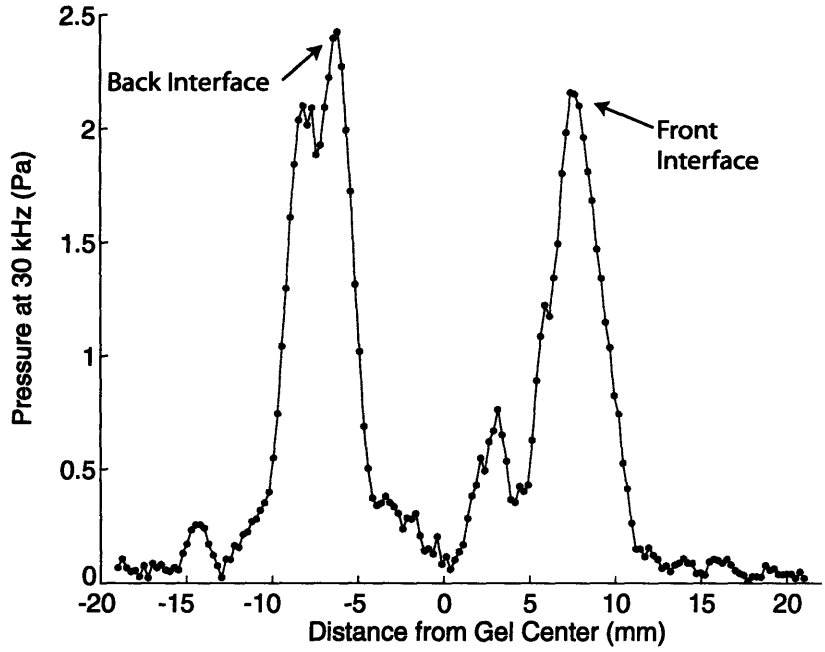


**Figure 3-24:** Experimental results for the second axial scan through a silicone gel tissue phantom demonstrating the generation of difference frequency sound on the order of 2.5 Pa when the focus of the primary beams is incident on the front and back interfaces of the target. The elements were each driven at 5 W electrical power (1.5 MPa peak acoustic pressure of each primary field).

### *Imaging Surface of ex vivo Rabbit Liver*

We performed a scan of the irregular surface of an *ex vivo* rabbit liver to demonstrate the parametric effect when using a dual-frequency system for imaging at a tissue interface. For this experiment, a portion of a rabbit liver was identified in which there was a 4mm diameter dimple in the normally smooth tissue surface. The liver was degassed prior to the scan to remove any bubbles that may have formed in the tissue post mortem. The liver sample was held in a plastic bag filled with saline to prevent further decomposition and positioned so that the focus of the dual-frequency system was at the tissue surface. The tissue was then scanned in a raster pattern of 14 mm x 14 mm (step size = .5 mm) along the plane of the tissue surface. At each position, 4 pulses at 15 W electrical power (corresponding to 5 MPa peak pressure at the focus of each primary field) were radiated from a concentric ring dual-frequency system operating at 1.7 MHz with an outer diameter of 10 cm, a focal distance of 8 cm, and a difference frequency of 7 kHz. The signal was received with a hydrophone (Benthos AQ-18, North Falmouth, MA) located approximately 20 cm away from the tissue surface, notch filtered around the difference frequency (Stanford Research Systems SR650, Sunnyvale, CA), registered to a digital oscilloscope (Tektronix TD210, Beaverton, OR),

and recorded by a personal computer via a IEEE-488 GPIB interface. An image was acquired by scanning the focus of the dual-frequency system over the surface of a fresh sample of rabbit liver as illustrated in Figure 3-25.

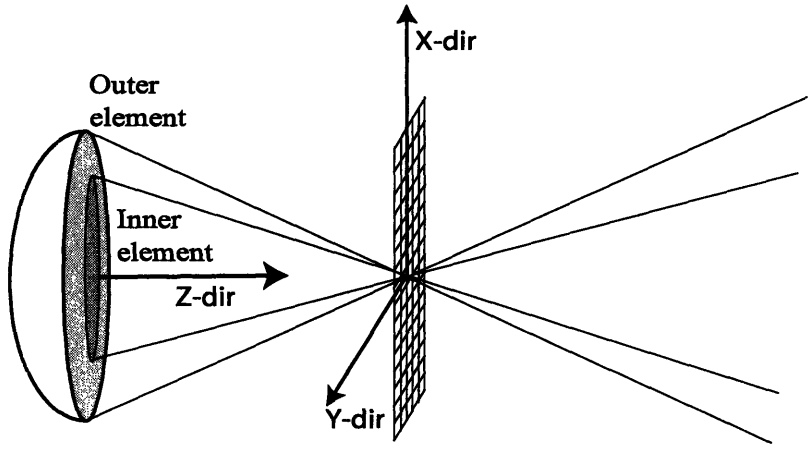


**Figure 3-25:** Diagram of the experimental set-up used for scans of *ex vivo* rabbit liver. The diagram indicates the grid of points through which the focus of the dual-frequency system was raster scanned in order to create an image based on the amplitude of the response from each location in the rabbit liver.

The result, displayed in Figure 3-26, demonstrates the sensitivity of this system to surface deviations of the tissue interface. The top of Figure 3-26 is a plot of the difference frequency amplitude as a function of scan position. The bottom of Figure 3-26 is a photograph of the irregular tissue surface. We recorded an increase in the difference frequency response when the focus of the dual-frequency system was incident on the crease and the indent,. The levels of the difference frequency signal for this experiment were in the range of 6-8 Pa. The experiment represents very preliminary data from an *ex vivo* tissue sample. Nonetheless, the correlation of the difference frequency signal with the tissue surface deviations indicated by the arrows support the conclusion that the geometry of the sample is an important factor contributing to the difference frequency response. While this experiment lacked sufficient controls to prove that the parametric effect was the source of the difference frequency signal, the sensitivity of the signal to the axial position of the interface which we observed while positioning the sample in the focus suggests that the parametric effect may have contributed to the response in a manner similar to the axial scans previously

discussed. This type of *ex vivo* tissue experiment (as well as eventual *in vivo* experiments) deserves attention in future work with a dual-frequency system.

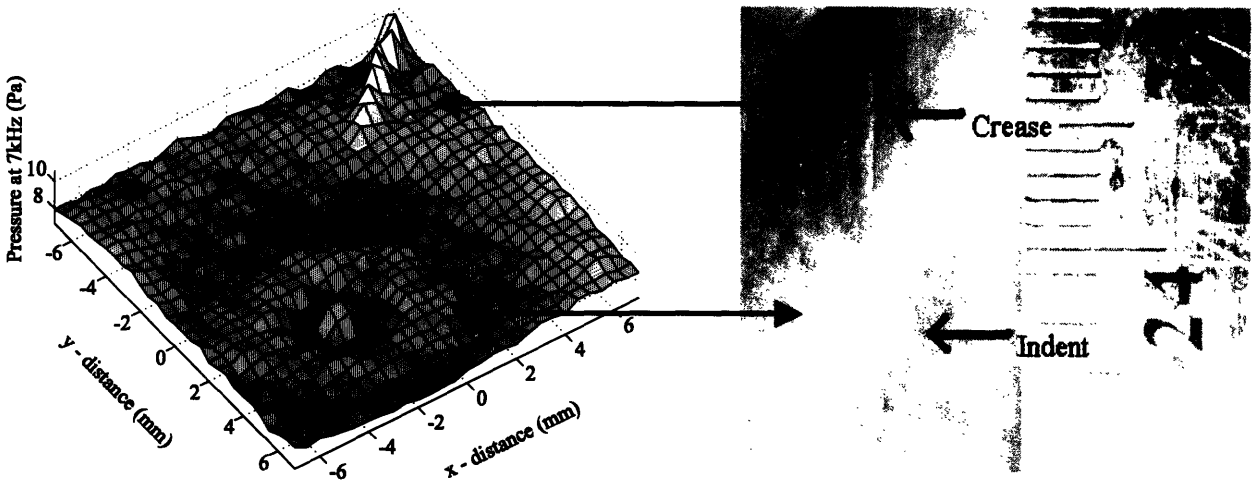


**Figure 3-26:** Experimental image of the surface of a rabbit liver. This image is created from the amplitude of the difference frequency signal plotted as a function of x-y position along the surface of the scanned *ex vivo* rabbit liver (top). The indent and crease, observed in the photograph of the tissue (bottom), are evident in the image of the difference frequency response (top).

## 3.3 Conclusions

In this chapter, we explored the generation of difference frequency sound by a mechanism called the parametric effect. First we described the theory of the parametric array and illustrated the relationship between the parametric array and Westervelt's original parametric effect. Then we modeled the parametric effect as it applies to the dual-frequency system used in this thesis by taking into account the multiple reflections of the primary field first from a silicone gel tissue phantom and then from the spherical cap of the second transducer to produce the parametric effect. The results of a simulation of the parametric effect, modeled using the target properties of the silicone gel tissue phantom, are displayed as a function of target rotation angle in Figure 3-14 together with the corresponding experimental results. The simulation and experimental results correlated reasonably well, illustrating the creation of difference frequency sound pressure at levels in the 1-10 Pa range

and supporting the hypothesis that the parametric effect was the primary source of difference frequency sound in the experiments performed in this chapter.

In the experimental section, we first demonstrated that the parametric array and parametric effect produce nearly identical sound levels at the difference frequency in a simple experiment plotted in Figure 3-17. Then, we conducted experiments involving the rotation and translation of the target in order to demonstrate the geometrical sensitivity of the measured difference frequency sound. Fatemi and Greenleaf[126] commented on the sensitivity of the difference frequency signal to the target geometry in a recent paper, but this effect has neither been previously studied in a systematic manner nor related to the parametric effect. In the systematic experiments in this chapter, the target was rotated and translated over a range of geometries. The rotational scan results, plotted in Figure 3-20 and Figure 3-21, demonstrated that the difference frequency signal was produced only over a limited range of target rotation angles. The maximum difference frequency signal was generated when the target was parallel to the plane of the transducers (see Figure 3-13). The axial scan results, plotted in Figure 3-23 and Figure 3-24, demonstrated the existence of the reflected power signal as well as the difference frequency signal only when the front or back interface of the target was in the focus of the primary fields. The results suggest that the reflection of the primary fields is critical for the generation of a difference frequency signal. Starting from basic experiments and building to more complicated and realistic imaging scenarios, the results in this chapter demonstrated the generation of a difference frequency signal from the parametric effect as evidenced by the sound levels and the geometry of the target at which a difference frequency signal was measured. In particular, in the simulations and experiments, difference frequency sound is created only when the field from one element is reflected back to the second element. In experiments, this conclusion is supported by the measured difference frequency signal and the reflected power signal from one element, which contained a strong frequency component at the primary frequency of the other element. The reflected power signal was sensitive to the orientation of the target in a manner similar to the difference frequency signal. These experimental results suggest that the source of difference frequency sound generation can be attributed to the parametric effect described in this chapter because the parametric effect relies upon the reflection of the field of one transducer from the second transducer. In our experiments, difference frequency sound was detected only when reflected power from one element was recorded at the surface of the other element.

This conclusion is significant because it indicates that previously hypothesized sources of difference frequency sound may be less important than this form of difference frequency sound generation. Experiments revealed that this mode of difference frequency sound generation may produce relatively large signals (1-10 Pa) relative to the other two mechanisms considered in this

thesis. Unfortunately, the parametric effect relies largely on the reflectivity of the target. Therefore, the benefits of imaging with this signal as opposed to imaging with traditional echo ultrasound system are not apparent. Nonetheless, it is important to identify this signal as a prominent source of difference frequency sound, at the very least, to further our understanding of the possible artifactual signals present in a dual-frequency imaging system such as the USVA system and the ways in which this type of difference frequency sound generation can be avoided.

# 4 Local Interaction of Two Pressure Fields

In this chapter, we examine the response of various targets to the local incident difference frequency field calculated using the free-space nonlinear wave equation. In practice, even with separate transducers, intersecting primary fields will contain collinear elements, which may produce a difference frequency field incident on a target. This incident field may scatter from the target and result in a difference frequency signal that can be detected outside of the interaction region of the two primary beams. In a previous study, non-collinear plane waves were considered and the nonlinear evanescent field at the difference frequency was shown to cause negligible scattering from several targets.[94] In this chapter, we examine the scattering of an incident difference frequency field due to focused transducers through simulations and experiments with various targets.

We begin by presenting the solution of the second-order wave equation for the difference frequency field using the Green's function integral method. We calculate the solution over the finite interaction region of two primary beams radiating from focused elements which are positioned at an angle of 35 degrees to each other (see Figure 4-3). We then present equations describing the linear scattering of the incident difference frequency field from several targets including a silicone gel tissue phantom, a pressure release sphere, and a small gas bubble.[xiv]

In simulations, we calculate the difference frequency field scattered from the interface of the target at a plane 10cm from the tissue phantom target and as a function of distance from the small bubble target. The results of the simulations reveal a difference frequency field with a maximum amplitude of 20 μPa for the case of the silicone tissue phantom. This pressure amplitude is not measurable given the system noise levels detailed in Table 1-1.

In the experimental section, we first check the linear simulation of the primary pressure field by comparing the simulated field to experimental measurements of the total linear field. Checking the simulation of the total linear field is an important step because we rely on the accuracy of the simulated linear field in solving the second-order wave equation. Then, we perform several experiments in an effort to measure a difference frequency field in the tank resulting from the scattering of the incident difference frequency field from the interface of a polyethylene plate and a

[xiv] These same scattering equations for various targets are used in chapter 5 to analyze the scattering at the primary frequencies.

silicone gel tissue phantom. The experiments support the conclusion drawn from the simulations, demonstrating an immeasurable difference frequency signal from the scattering of incident difference frequency sound from various targets.

## 4.1 Theory

*Total Difference Frequency Pressure at Focal Plane*

To solve for the total difference frequency pressure at the focal plane of the primary beams, we calculate the difference frequency field using the volume integral solution for the second-order wave equation given by equation (0.25). The solution relies upon knowledge of the primary pressure fields $P_a$ and $P_b$. The primary pressure fields are determined by Green's theorem[127], in which the free-space Green's function is multiplied by the source amplitude for a baffled simple source[128], and the product is integrated over the surface of the radiating transducer,

$$P_{a,b}(\mathbf{r}) = \frac{j\rho_0 c_0 U_0 k}{2\pi} \iint_{S'} \frac{e^{j(\omega_{a,b}t - \mathbf{k}_{a,b}\cdot(\mathbf{r}-\mathbf{r}'))}}{4\pi|\mathbf{r}-\mathbf{r}'|} dS' \tag{50}$$

where $\mathbf{r}$ and $\mathbf{r}'$ are the locations of the receiver and source points respectively, $U_0$ is the amplitude of the in-phase velocity of the source points at the transducer surface $S'$, and $\mathbf{k}_{a,b} = (k_x, k_y, k_z)$ is the wave vector.

*Scatter Functions of Targets*

We consider the scattering of the incident difference frequency field from a pressure release sphere, an air-bubble, and an infinite horizontally stratified medium. In this section, we present the general form of the scattering problem and specific scatter functions for the targets we simulate. For the targets we consider, the scatter functions detailed below describe the scattered field for an incident plane wave. Therefore, the total difference frequency pressure at the interface with the target, $P_-$, must first be transformed into the "local plane wave spectrum" by means of the two-dimensional spatial Fourier Transform following the method described by Korpel[112] and using the Fourier transform pair,

$$P(k_x,k_y;z_0)=\int_{-\infty}^{\infty}\int_{-\infty}^{\infty}P(x,y,z_0)e^{-j(k_x x+k_y y)}dxdy$$
$$P(x,y,z_0)=\left(\tfrac{1}{2\pi}\right)^2\int_{-\infty}^{\infty}\int_{-\infty}^{\infty}P(k_x,k_y;z_0)e^{j(k_x x+k_y y)}dk_x dk_y \quad (0.51)$$

The scattered field for the case of a pressure release sphere and a small air bubble follow the form given by the approximation[78,127],

$$P_s(r)\approx P_i(\mathbf{k}_i)\cdot\frac{S(k_i)}{kr}e^{j(kr)} \quad (0.52)$$

where $k_i=|\mathbf{k}_i|=k=\frac{\omega}{c_0}$ is the wave number corresponding to the incident wave vector $\mathbf{k}_i$, $P_i$ is the incident plane wave, $P_s(r)$ is the scattered wave at distance $r$ from the origin located at the target center, and $S(k_i)$ is the scatter function for the target considered, which is independent of the incident and outgoing wave vector directions because we only consider the case of omni-directional scattering from a pressure release sphere and an air bubble satisfying $ka\ll 1$ (the object is very small compared to the difference frequency wavelength). In general, for small solid scatterers, the scatter function will not be spherically spreading. The approximation of equation (0.52) is valid for the far field where $|\mathbf{r}|>\frac{L^2}{\lambda}$, given the target dimension $L$ and wavelength $\lambda$.

For the infinite horizontally stratified medium, the outgoing scattered wave is not omni-directional. In this case, we use a k-space reflection coefficient[123] to calculate the reflection of plane wave components of the total field, obtained by a Fourier decomposition of the local difference frequency field into the "local plane wave spetrum"[112].

*Pressure Release Sphere (vacuum bubble)*

Pressure release spheres are considered because they represent bubbles that might occur in tissue during thermal therapy with focused ultrasound due to voids created by cavitation or the boiling of tissue. Pressure release spheres that satisfy the condition $ka\ll 1$ can be approximated by an omni-directional scatter function given by[78],

$$S=ka \quad (0.53)$$

From this simple scatter function, we observe that the strength of the scattered field is proportional to the diameter, $a$, of the pressure release sphere.

*Air Filled Bubble*

Air-bubbles present a sudden change in compressibility from the water to air medium and may exhibit resonance in the frequency ranges of interest depending on their size. Practically speaking, bubbles are significant in medical imaging of thermal therapy because they may be produced during high-intensity therapeutic ultrasound treatment due to cavitation events[129].[130] In addition, gas bubbles can be added to the body in the form of contrast agents containing micro-bubbles. This technique is increasingly utilized to enhance echogenicity in ultrasound imaging.[130] The term air-bubble in this thesis refers specifically to gas-bubbles containing a gas with a ratio of specific heats, $\gamma = 1.4$. This applies to bubbles containing either Nitrogen, Oxygen, or common air. However, the scatter function below can be used for any gas-containing bubble if the appropriate constant $\gamma$ is used. Brekhovskikh[131] gives the scatter function for an air bubble satisfying $ka \ll 1$,

$$S = \frac{ka}{(f_r/f)^2 - 1 - ika} \tag{0.54}$$

where the bubble resonance $f_r$ is,

$$f_r = \frac{(3\gamma P_0/\rho)^{1/2}}{2\pi a} \tag{0.55}$$

($\gamma = 1.4$ is the ratio of specific heats for air, $\rho = 1000\ \mathrm{kg}/m^3$ is the water density, $P_0 = 100$ kPa is the ambient pressure, and $a$ is the bubble radius in meters).

Note that the scatter function increases dramatically as the frequency of the incident field approaches the bubble resonance reaching a maximum magnitude of 1 at resonance. Bubble resonance may contribute to enhanced difference frequency sound generation. In particular, bubble resonance becomes significant when considering the interaction of waves scattered at the primary frequencies for which the resonant bubble size is on the order of a micron and the peak pressure levels of the primary field are in the MPa range at the focus. As we will see in chapter 5, this may lead to scattered waves of appreciable magnitude at the primary frequencies even from a single resonant bubble.

*The infinite horizontally stratified medium*

We consider the reflection problem for plane waves incident on an infinite horizontally stratified medium because this is closely related to the geometry of difference frequency waves incident on organ and tissue interfaces *in vivo*. Organ and tissue interfaces can be approximated as infinite planar surfaces given $L \gg \lambda$ , where $L$ is the dimension of the planar interface of the tissue and $\lambda$ is the wavelength of the incident pressure wave. In experiments in this thesis, a rigid plate of polyethylene or a slab made from a silicone gel is used to model this interface. We use the K-space reflection coefficient, $R(k_x, k_y)$ for a horizontally stratified medium[123] given by,

$$R(k_x, k_y) = \frac{R_{01} + R_{10} e^{2jk_1 h \cos\theta_1}}{1 + R_{01} R_{10} e^{2jk_1 h \cos\theta_1}} \tag{0.56}$$

where $k_1 = \frac{\omega}{c_1}$ and $R_{01}$ is the real-space reflection coefficient for a horizontally stratified medium given by $R_{01} = \frac{m_0 \cos\theta_0 - \sqrt{n_0^2 - \sin^2\theta_0}}{m_0 \cos\theta_0 + \sqrt{n_0^2 - \sin^2\theta_0}}$, (where $m_0 = \frac{\rho_1}{\rho_0}$ and $n_0 = \frac{k_1}{k_0}$) .[78] The reflection coefficient is valid for plane waves at any angle of incidence and can be used together with the planar decomposition of the incident difference frequency field (0.51) to give the reflected difference frequency field as,

$$P_s(x, y, z) = \left(\tfrac{1}{2\pi}\right)^2 \int_{-\infty}^{\infty} \int_{-\infty}^{\infty} R(k_{-x}, k_{-y}) P_-(k_{-x}, k_{-y}; z_0) e^{jk_{-z}(z - z_0)} e^{j(k_{-x}x + k_{-y}y)} dk_{-x} dk_{-y} \tag{0.57}$$

where the difference frequency wave vector is indicated by $\boldsymbol{k}_- = (k_{-x}, k_{-y}, k_{-z})$, the scattered field is $P_s(x, y, z)$ at location $(x, y, z)$, and the position of the interface of the target is $z_0$.

## 4.2 Simulations

In the simulation section, we first calculate the total linear pressure field from two elements of various geometries. The accuracy of the solution to the second-order wave equation calculated later in this section relies upon our ability to first accurately solve for the total linear field. Next, we simulate the combined linear field of two separate elements in the vicinity of the focal plane to check the validity of applying the volumetric integral solution to the second-order wave equation over a limited region in which the two primary fields interact. Then, we solve for the local incident

difference frequency field at the focal plane. Finally, we calculate the scattered field from a small air bubble, a small pressure-release sphere, a polyethylene plate, and a silicone tissue phantom plate to find the resulting difference frequency field in space.

### *4.2.1.1 Linear Field Simulations*

#### *Concentric Ring Transducer*

For the case of the concentric ring transducer, the fields from an inner element (7.3 cm diameter, 8 cm radius of curvature, 1.624 MHz) and an outer element (10 cm diameter, 8 cm radius of curvature, 1.624 MHz) with equal surface areas are calculated separately using the Green's theorem method described in equation (50). We include the time dependence term $e^{j\omega_{a,b}t}$ because the sum of the two fields varies in time at the difference frequency. The resulting primary fields are added together to give the total primary pressure field $P_T$,

$$P_T(\mathbf{r},t) = \frac{j\rho_0 c_0 U_0 k_a}{2\pi}\iint_{S'}\frac{e^{j(\omega_a t-\mathbf{k}_a\cdot(\mathbf{r}-\mathbf{r}'))}}{4\pi|\mathbf{r}-\mathbf{r}'|}dS' + \frac{j\rho_0 c_0 U_0 k_b}{2\pi}\iint_{S'}\frac{e^{j(\omega_b t-\mathbf{k}_b\cdot(\mathbf{r}-\mathbf{r}'))}}{4\pi|\mathbf{r}-\mathbf{r}'|}dS' \tag{58}$$

(where $\rho_0 = 998kg/m^3$ is the density of the water, $c = 1500m/s$ is the speed of sound in the water, $k_{a,b} = \frac{\omega_{a,b}}{c}$ is the magnitude of the wave-vector for the field at frequency $\omega_{a,b}$, $\mathbf{r}$ is the position of the measurement point in the units of meters, and $\mathbf{r}'$ is the position of the source point on the surface of the transducer $S'$ in the units of meters). The simulation returns the total complex pressure generated by the inner and outer transducer elements at points in the focal plane of the two elements (Figure 4-1).

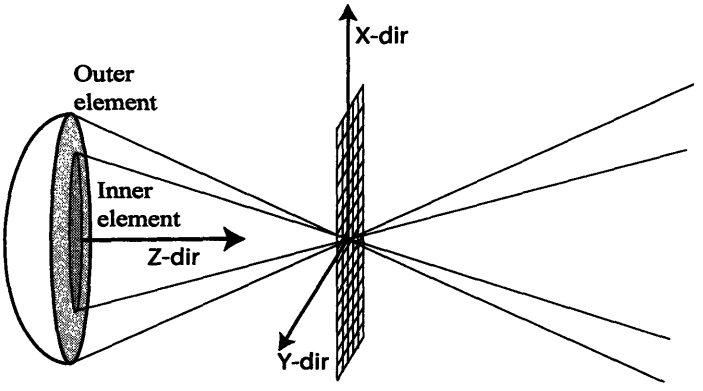


**Figure 4-1:** Diagram of the simulation of the total linear pressure field produced by concentric elements operating at different frequencies.

Only the difference frequency component of $P_T^2$ (containing the cross term $P_a P_b^*$) is used in the solution of the nonlinear wave equation (0.25) to simulate the incident difference frequency field at the focal plane. The other cross-terms, given in (0.23), do not result in the generation of a difference frequency field, as described in section 2.2. However, in order to compare the simulated total linear field to experiments, the entire term $P_T$ is simulated here because in experiments, the needle hydrophone measures the total primary frequency field $P_T$. Figure 4-2 displays the magnitude of the simulated total linear pressure field $P_T$ generated from driving the outer and inner elements at $f_1 = 1.675MHz$ and $f_2 = 1.725MHz$ respectively and 10 W electrical power per element, corresponding to 2 MPa peak pressure at the focus of each primary field. The field oscillates at the difference frequency $\Delta f = 50kHz$ between the two instances in time displayed. The most notable feature of this pressure field is the pattern of phase reversals due to the interaction of the two primary fields. The geometry of the inner and outer elements results in an interference pattern that has the form of rings of in-phase pressure alternating with rings of 180 degree out-of-phase pressure. Further, these phased rings of pressure evolve in time so that when the two fields are exactly in phase at the focal plane, they add constructively to make a peaked focus as seen in the top plot of Figure 4-2. When the two fields are exactly out of phase in time they cancel at the focus and make a broad ringed pattern as observed in the bottom plot of Figure 4-2.

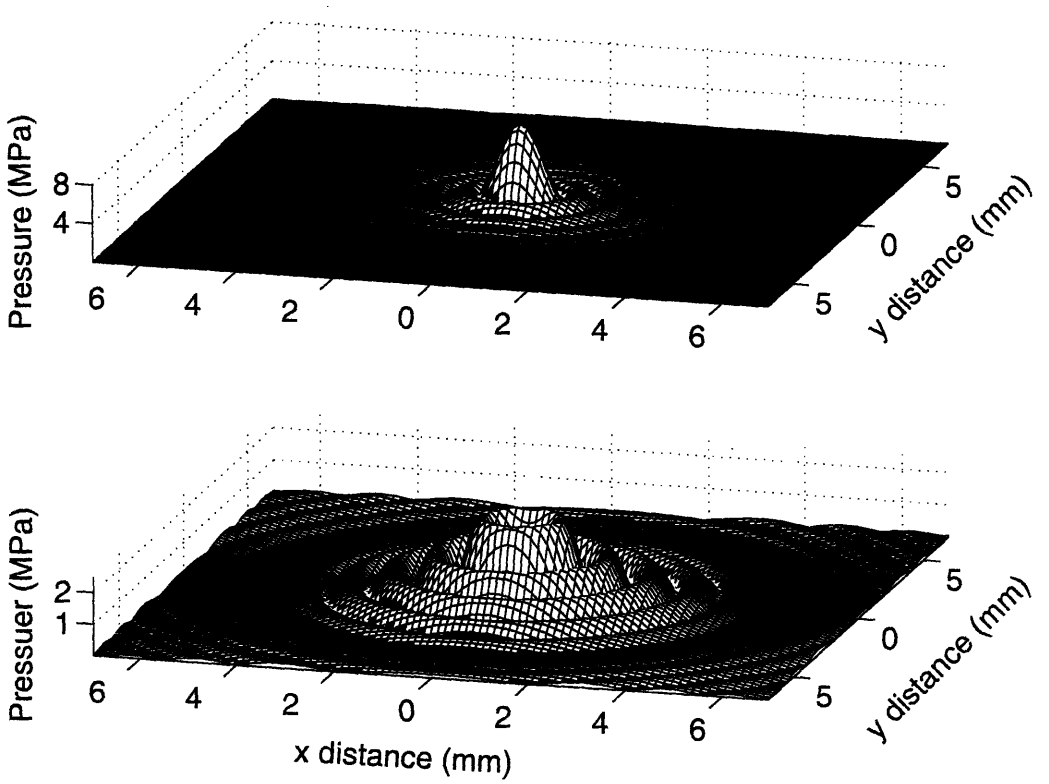


**Figure 4-2:** Simulated total linear pressure field from a concentric element transducer with F-num = .8. The inner and outer elements are driven at 1.675 MHz and 1.725 MHz respectively and 10 W electrical power each. The result is displayed at 0 relative phase (row 1) and 180 relative phase (row2) of the two fields.

The total field at the primaries from the two elements driven at different frequencies and with an F-number[xv] of .8 is compared to experiments in Figure 4-18. The simulation agrees reasonably well with the experimental measurements. Simulation and experiment show a similar phase-reversal pattern.

*Separate Element System*

For the case of two separate elements intersecting at an angle to produce a summed field in the focal plane, a slightly more complicated simulation is needed. First, we calculate the linear pressure field from each element (4 cm diameter, 10cm radius of curvature, 2.705 MHz and 2.755 MHz) using the method described above by equation (50). Then, we transform the complex

[xv] The F-number is defined as the ratio of the focal distance to the diameter of the spherically focused element. It is proportional to 3db diameter of the focused pressure field created by the geometric curvature of a spherical element.[127]

pressure fields into the "local plane wave spectrum" using the forward transform of the Fourier transform pair[112],

$$P(k_x,k_y;z_0)=\int_{-\infty}^{\infty}\int_{-\infty}^{\infty}P(x,y,z_0)e^{-j(k_x x+k_y y)}dxdy$$
$$P(x,y,z_0)=\left(\frac{1}{2\pi}\right)^2\int_{-\infty}^{\infty}\int_{-\infty}^{\infty}P(k_x,k_y;z_0)e^{j(k_x x+k_y y)}dk_x dk_y \quad (59)$$

Once in wave-vector space, the field from each element can be projected or rotated to the desired orientation using the methods outlined by Clement[132]. In this case, the fields are first projected to the focal plane at 10 cm. Then, one field is rotated by α/2 in the positive θ-direction while the other field is rotated by α/2 in the negative θ-direction by multiplication of the basis vector $(k_x,k_y,k_z)$ with an Euler rotation matrix $\hat{A}(\phi^{ROT},\theta^{ROT},\psi^{ROT})$ to give a new rotated basis $(k'_x,k'_y,k'_z)$. The resulting fields are transformed back into real space by means of the inverse spatial, two-dimensional Fourier Transform from equation (59) and summed together. The simulations were calculated for two separate elements driven at different frequencies and intersecting at an angle α ranging from 0 degree to 180 degrees (Figure 4-5).

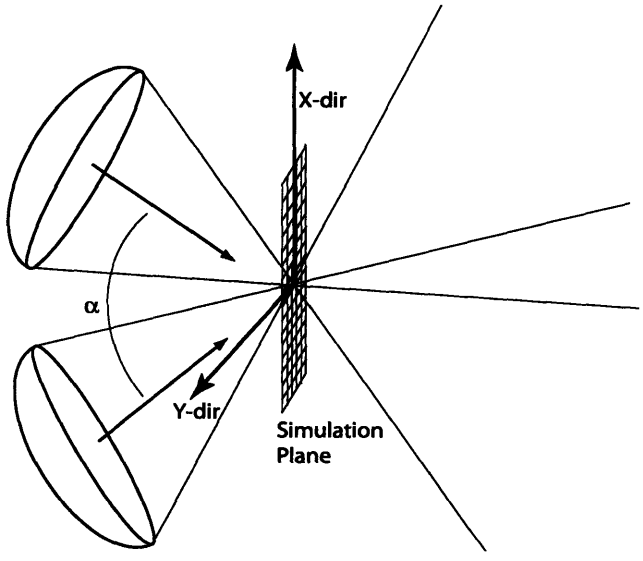


**Figure 4-3:** Diagram of the simulation of the total linear pressure field generated by elements separated by an angle alpha.

The simulated amplitude of the total linear pressure field from the two elements driven at different frequencies and with an angle of separation of 25 degrees and 50 degrees is plotted in Figure 4-4 and Figure 4-5 respectively. In both simulations, the field oscillates at the difference frequency between the two instances of time displayed. Similar to the concentric element case, the difference frequency field has a pattern of phase reversals due to the interaction of the two primary fields. However, the pattern for the system with separate elements is different than for the concentric element case. Here, the result at any given instant in time is a field with stripes of in-phase pressure alternating with stripes of 180 degree out-of-phase pressure. We note that as the angle of separation of the elements increases, the stripes of phase reversed pressures become narrower until a limit of spacing on the order of the wavelength of the primary frequencies is obtained.

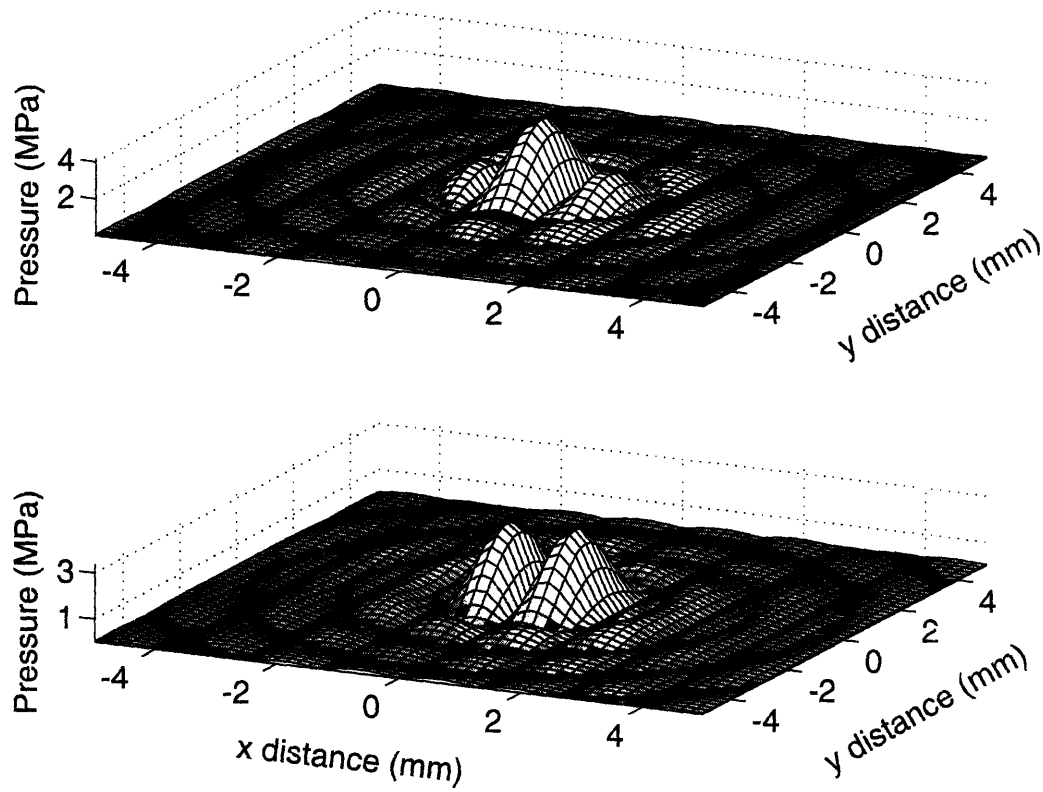


**Figure 4-4:** Simulated total pressure field generated by two elements separated by an angle of 25 degrees. The simulation result is plotted at 0 relative phase (row 1) and 180 relative phase (row2) of the two primary fields.

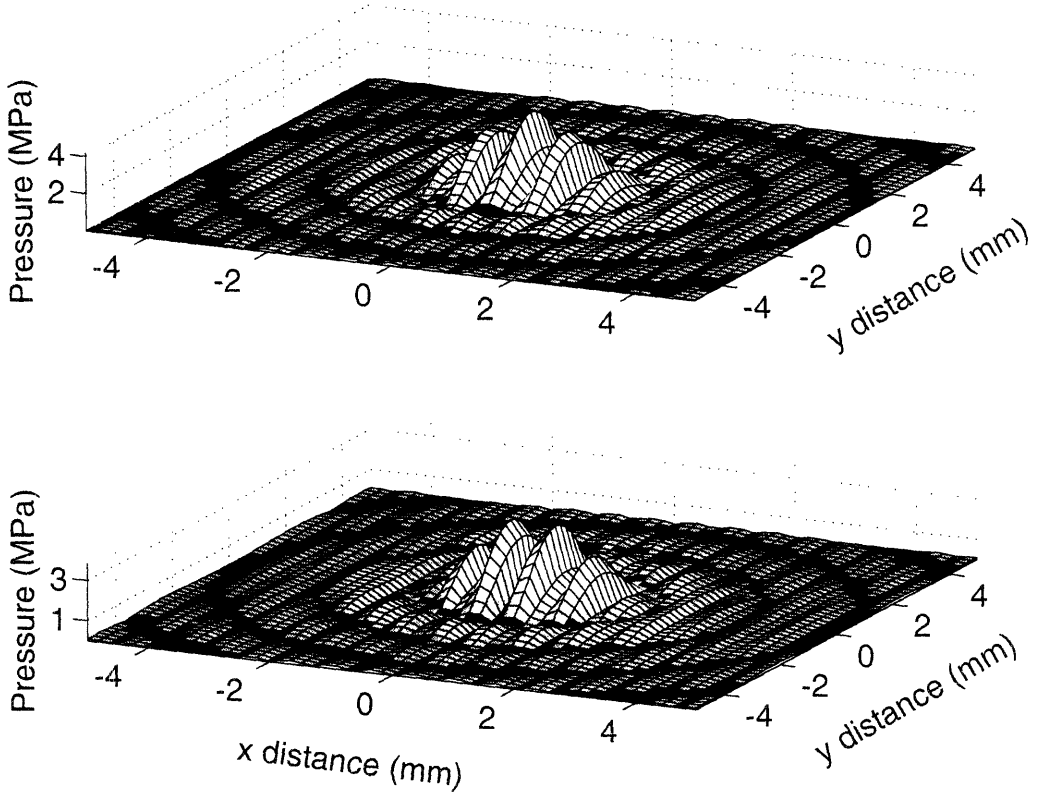


**Figure 4-5:** Simulated total pressure field generated by two elements separated by an angle of 50 degrees. The simulation result is plotted at 0 relative phase (row 1) and 180 relative phase (row2) of the two primary fields.

The simulations of the total linear field are compared to experiments for the elements angled at 25 and 50 degrees to each other in Figure 4-19 and Figure 4-20 respectively. As seen in these figures, the simulations correlate relatively well with the experimentally measured fields and demonstrate similar striped phase reversal pattern.

*Interaction Region*

In order to solve for the local incident difference frequency pressure at the focal plane, we must integrate $P_a P_b^*$ over the region in space where the two primary fields interact to generate a difference frequency field according to the volumetric solution method of equation (0.25). We define the interaction region as the volume in space where the product of the two fields, $P_a P_b^*$, achieves an amplitude of at least $1/100^{th}$ of the peak value for this quantity and we make the approximation that outside of this region, there is no significant interaction between the two fields.

Using this definition, we can limit the integral of equation (0.25) to a finite interaction volume. Limiting the domain for the integral to the finite interaction region greatly reduces the computation time for this integral. The product $P_a P_b^*$ for two elements (4 cm diameter, 10 cm radius of curvature) separated by an angle of 35 degrees is simulated in Figure 4-6 along with the profile of the primary fields ( $P_a$ and $P_b$ ) from each element. The primary fields are plotted in each of the first two columns and the combined pressure term $P_a P_b^*$ is plotted in the third column. The axial distance[xvi] on the plot starts at the focal plane (z = 0) and extends towards the plane of the transducers by a distance of 10 mm. The object with which the resulting difference frequency field will interact is located at radial distance[xvii] = 0, axial distance = 0. The figure illustrates that despite the relatively long focal dimension of the primary beams (approximately 15 mm in length for the -3db value), the interaction region is finite and extends for only 2-3 millimeters in front of the focal plane. The limited interaction region of the two pressure fields is due to the geometry of the separate element system, which creates primary fields that intersect at an appreciable angle, thereby limiting the extent of the interaction region.

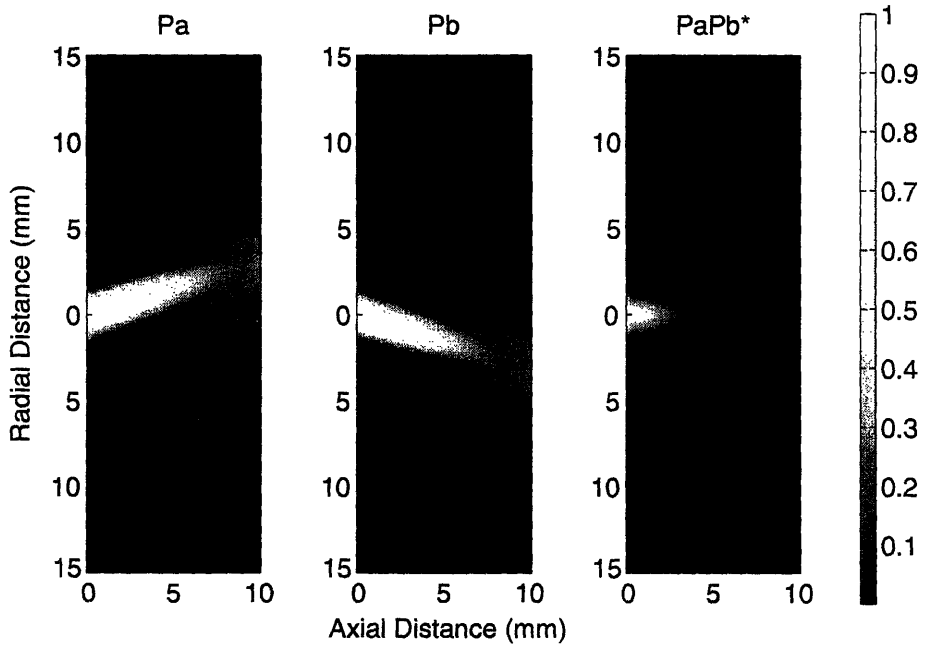


**Figure 4-6:** Normalized plots of the simulated incident primary fields Pa and Pb, and their product PaPb*. PaPb* is the combined source term of the second order wave equation. The axial distance starts at the focal plane (z = 0) and is simulated towards the plane of the transducers. The object with which the field interacts is centered at the focus (radial distance = 0, axial distance = 0).

---

[xvi] Axial distance refers to the distance along the axis of propagation and is measured in these simulations from the focal plane at a distance of 0 mm towards the transducer face.

[xvii] Radial distance refers to the distance from the geometric center of the transducer outward in the radial direction.

### *4.2.1.2 Nonlinear Difference Frequency Field*

Finally, we simulate the total difference frequency pressure at the focal plane using the above experimentally verified results for the primary fields and the volume integral solution to the second order wave equation as provided in equation (0.25) of the theory section. The volume integral solution method is applied without computational difficulty because the interaction region is limited to only a few millimeters in depth as demonstrated by the results of the incident primary fields in Figure 4-6 and illustrated in the diagram of Figure 4-7.

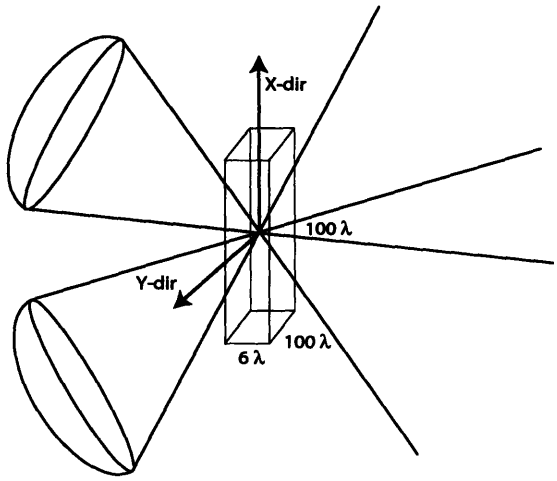


**Figure 4-7:** Diagram of the interaction region of two pressure fields generated by separate elements intersecting at a common focal point.

We calculate the incident difference frequency pressure at the focal plane of the primary beams by plugging the combined pressure term, $P_a P_b^*$, (plotted in Figure 4-6) into the volume integral solution of the second-order wave equation (0.25). Figure 4-8 shows the result for the instantaneous value of the difference frequency pressure field at the focal plane for one point in time. The field is calculated using two 4 cm diameter, 10 cm radius of curvature elements oriented at 35 degrees between centers and each driven with 10 W electrical power (corresponding to 2 MPa peak pressure at the focus of each primary field) at a frequency of $2.73MHz \pm 25kHz$ to provide a difference frequency of $50kHz$.

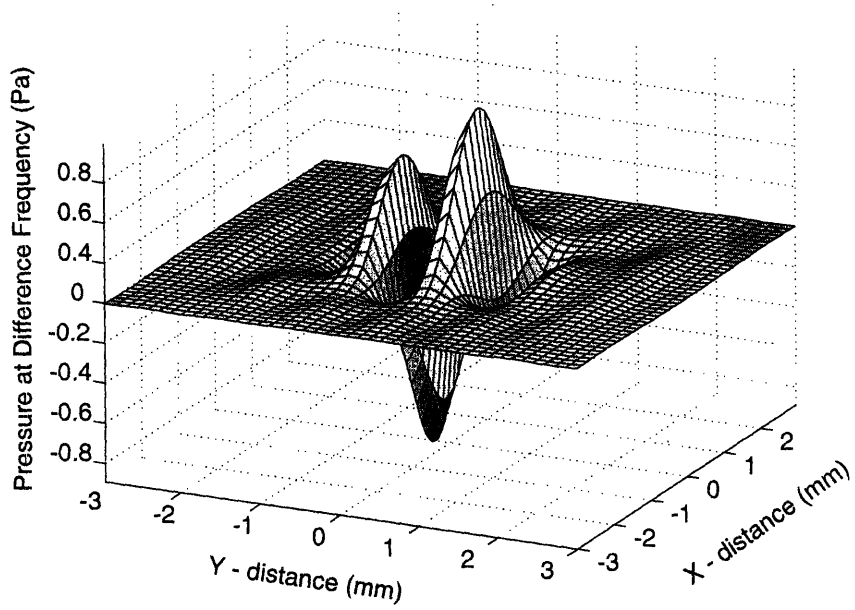


**Figure 4-8:** Simulated instantaneous value of the total difference frequency pressure at the focal plane from the intersection of two primary pressure fields of a separate element system with a 35 degree angle of separation. The difference frequency field was calculated using the Green's Function integral solution for the second order wave equation.

We note that the difference frequency field demonstrates a phase-reversal pattern, which oscillates at the difference frequency, similar to the total primary field. For soft targets, the local pressure pattern will cause motion of the target interface. For all objects (hard or soft), the difference frequency waves will scatter out from the object and may be detected by the low frequency hydrophone in the tank. The amplitude of the scattered field depends on the mechanical properties of the target which can be related to the acoustical properties by $c = \sqrt{\beta/\rho}$ , where $\beta = \frac{E}{3(1-2\nu)}$ is the Bulk Modulus of the material for a given Young's Modulus, E, and Poisson's Ratio, $\nu$. See Appendix C for a more detailed explanation of the relationship between the acoustical and mechanical properties of the target. The difference frequency pressure field displayed in Figure 4-8 will scatter from an object located at the focal plane. In the next section, we simulate the scattered difference frequency field resulting from several different targets.

*Scattered Local Difference Frequency Field*

Before calculating the amplitude of the scattered difference frequency field, we note that the scattering function, $S$, or reflection coefficient $R(k_x, k_y)$, is much less than one for targets we use. Therefore, we would expect the scattered field to be small. The result of scattering from a single micro-bubble, for example, is very small due to its small size, which allows only part of the

incident energy to scatter outward. In addition, we note from equation (0.52) that in the far field, the sound pressure at the difference frequency falls off at a rate $\frac{1}{r}$ as the receiver is moved a distance $r$ from the center of scattering from the small gas bubble or pressure release sphere. This rate of decay is due to spherical divergence and will tend to reduce our ability to detect the difference frequency sound further.

The simulations described in this section use the difference frequency field calculated above Figure 4-8 for separate focused sources driven at 10 W electrical power (corresponding to 2 MPa peak pressure of the primary field) with a difference frequency of 50 kHz and the parameters detailed in Table 1-4. First, we simulate the response of a single, small ($ka \ll 1$) pressure release sphere and air-filled bubble (Figure 4-9).

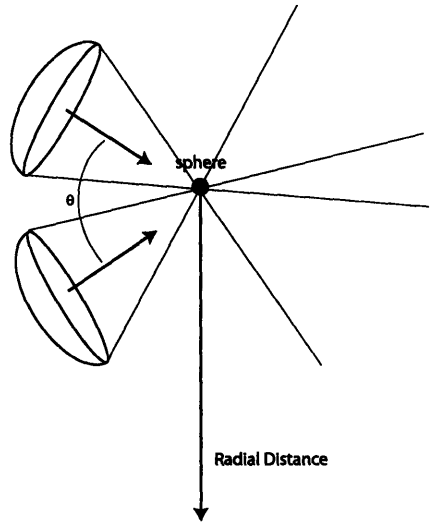


**Figure 4-9:** Diagram of the model for scattering of the local difference frequency field from a small spherical target.

Because we suspect that the scattered field will be much smaller than the peak of the incident field (which is .6 Pa according to Figure 4-8), we perform simulations in an effort to calculate the maximum possible scattered difference frequency pressure. To maximize the scattered field, two scenarios are simulated. The first case we consider is the simulation of the largest spherical target that still satisfies the condition of omni-directional scattering ($ka \ll 1$). For this simulation, a bubble of 400 μm is modeled. This is two orders of magnitude larger than bubbles modeled in chapter 5 where the maximum diameter considered must scale with the primary frequency wavelengths. The second scenario we simulate is the interaction of the local difference frequency field with a bubble that is exactly the resonant size for the 50 kHz difference frequency pressure acting upon it. It is well known that resonance greatly increases the scattering efficiency of

a bubble[131]. In Figure 4-10, we plot the simulation results for the scattered incident difference frequency field as a function of distance from the interaction region for the two optimal scattering scenarios.

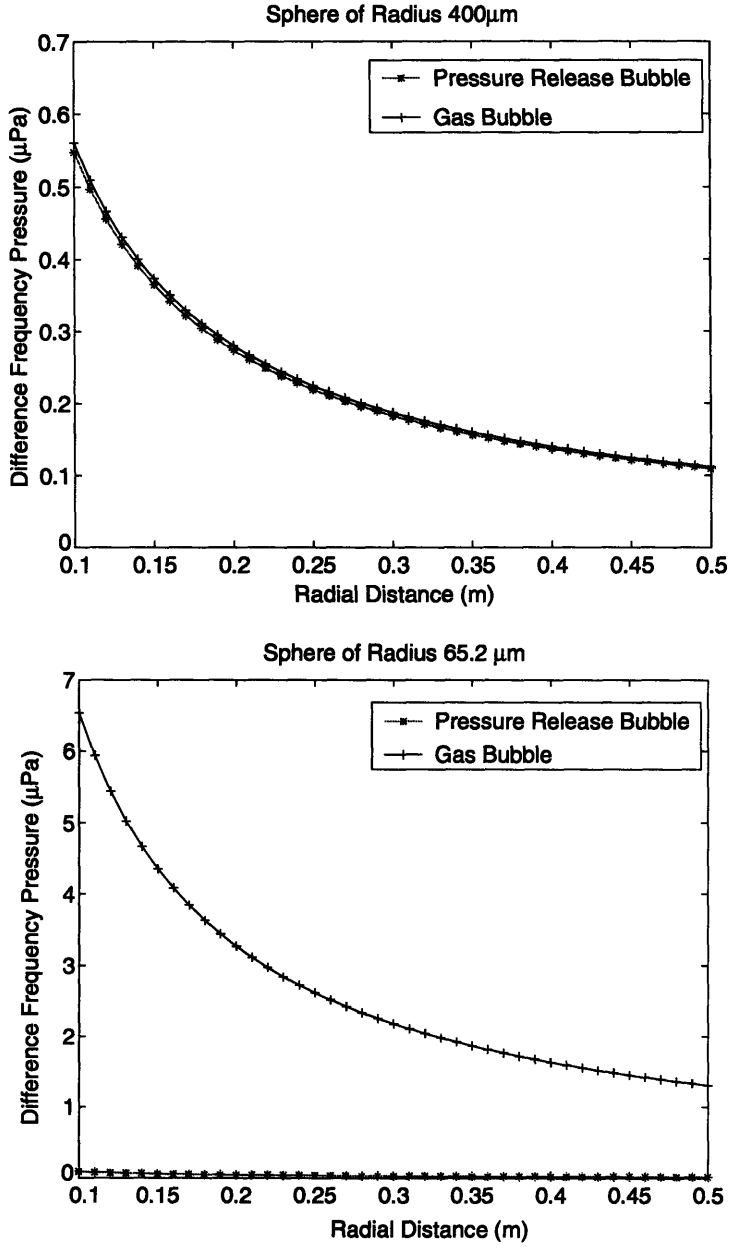


**Figure 4-10:** Simulated difference frequency pressure after the scattering of a local difference frequency field from a small object. The result is plotted as a function of distance from the interaction region. The simulation for a 400 μm spherical scatterer is plotted on top. The simulation for a resonant spherical scatterer (65.2 μm) is plotted on bottom.

The simulations results reveal a small difference frequency signal reaching a maximum of 6.5 μPa for the case of the resonant bubble at 10 cm from the interaction region. This pressure level is well below the noise floor of .1 Pa for the experimental system. For the case of the 400 μm

spherical target, the response of the air-filled bubble and the pressure release sphere are nearly the same amplitude. For the case of scattering from a resonant bubble or a pressure release sphere of the same diameter, the difference frequency amplitude scattered from the pressure release sphere is on the order of $1e^{-7}Pa$, which is several orders of magnitude below the response from the resonant air-bubble (6.5 μPa).

Next, we simulate the planar reflection of the incident difference frequency field (Figure 4-11). Two cases are considered for the planar target. First, we simulate the reflection of the incident difference frequency field from a planar target of the silicone gel tissue phantom material ($\rho = 1000kg/m^3, c = 1050m/s$). The result of the reflected difference frequency field is used to benchmark the values from experiments with the silicone gel. Then, we simulate the difference frequency due to the reflection from a perfectly reflecting plate ($R = 1$), in an effort to establish an upper bound on the magnitude of the difference frequency field scattered from the interaction zone.

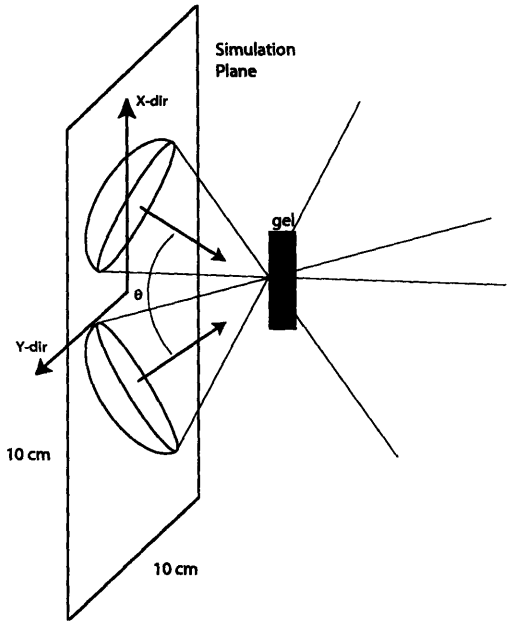


**Figure 4-11:** Diagram of the simulated reflection of an incident difference frequency field from a planar target.

We use the same solution for the incident field at the difference frequency as used for the scattering from spheres. The planar interface of the silicone gel or perfect reflector is located at the focal plane of the two sources. The resulting difference frequency field is numerically solved at a plane 10 cm from the interaction region. This distance represents the closest measurement position used in experiments. We did not simulate the result over planes farther than 10 cm from the source, because we want to calculate a maximum value of the reflected field and would expect even smaller

difference frequency levels farther away. The simulation results, plotted in Figure 4-12, show the difference frequency field after reflection from the silicone gel tissue phantom. The reflected difference frequency field reaches a maximum of approximately 20 μPa for this simulation. This maximum pressure value is well below the noise floor of .1 Pa for the experimental system.

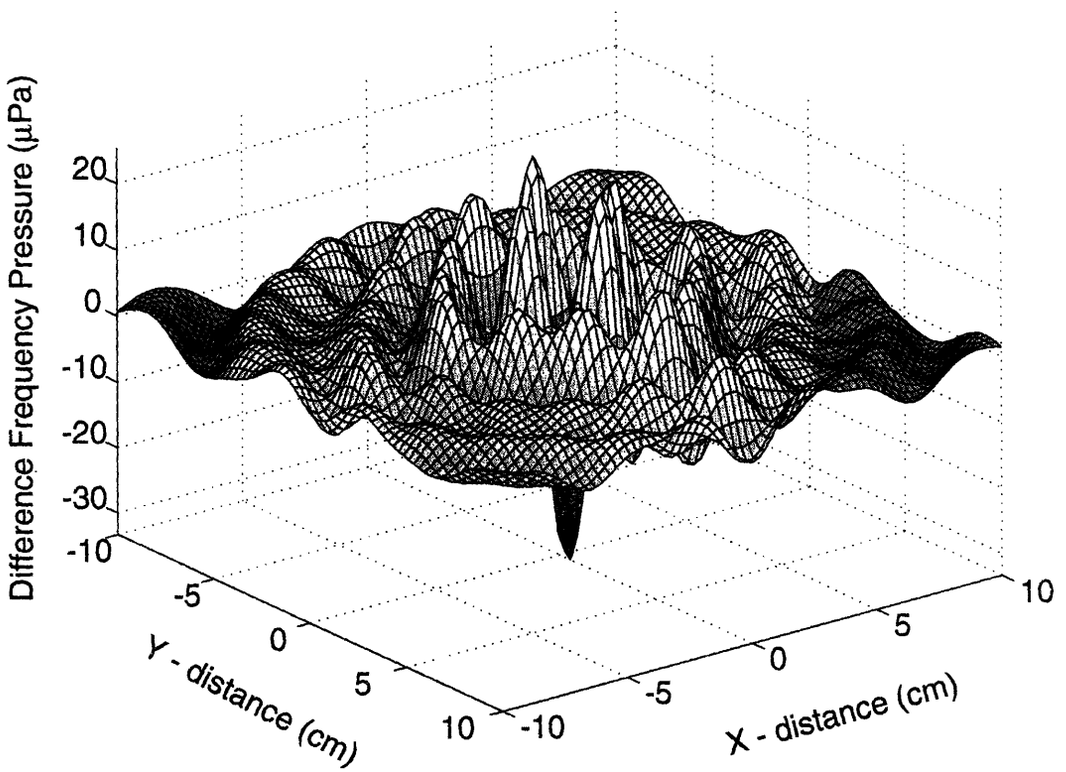


**Figure 4-12:** Simulated difference frequency field at a plane 10 cm from the silicone gel target. This field results from the scattering of a local difference frequency pressure field from a silicone gel tissue phantom.

The simulation result for the reflection of the incident difference frequency field from the perfect planar reflector is plotted in Figure 4-13. This result demonstrates a reflected difference frequency pressure that is more sharply focused as compared to the reflected field from the soft silicone gel tissue phantom. The improvement in focusing is most likely due to the lack of multiple reflections, which occur within the horizontally stratified silicone gel model. Instead, for the perfectly reflecting plate, all of the incident energy is reflected from the front interface of the planar target producing a modest focusing effect. Despite this focusing effect, the peak pressure at the difference frequency is only slightly larger for the perfect reflector (approximately 30 μPa) as compared to the silicone gel target (approximately 20 μPa). However, in both cases, the difference

frequency peak is many orders of magnitude below the amplitude of the system noise (.05 Pa) and would not be detectable experimentally.

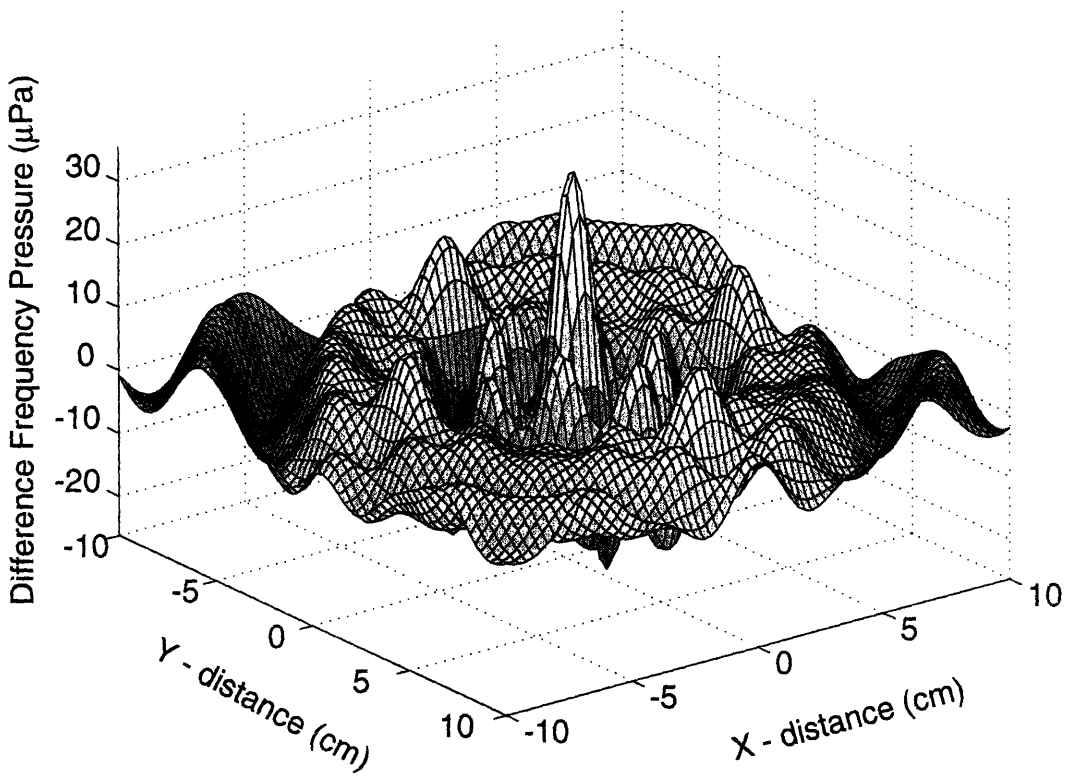


**Figure 4-13:** Simulated difference frequency field at a plane 10 cm from the perfectly reflecting planar target. This field results from the scattering of a local difference frequency pressure field from a perfectly reflecting plate.

*Local Displacement at the Difference Frequency*

In addition to scattering from the target, the incident difference frequency field may cause displacements at the target interface. The magnitude of the displacement depends on the relative mechanical modulus of the target. We use the equations of continuity of pressure and conservation of momentum,

$$P_i + P_R = P_T$$

$$\frac{1}{\rho_1}\frac{\partial}{\partial r}(P_i + P_R) = \frac{1}{\rho_2}\frac{\partial}{\partial r}(P_T) \tag{0.60}$$

with the mechanical/acoustical properties of the target in order to calculate the displacement of the interface.. If we substitute the expressions for the incident pressure, $P_i = P_-$, the reflected pressure, $P_R = R \cdot P_i$, and the transmitted pressure, $P_T = T \cdot P_i$, (where $P_-$ is the local pressure at the difference frequency due to the interaction of the primary fields) into (0.60), we can solve for the reflection and transmission coefficients,

$$R = \frac{\rho_2/\rho_1 - c_1/c_2}{\rho_2/\rho_1 + c_1/c_2}$$
$$T = \frac{2 \cdot \rho_2/\rho_1}{\rho_2/\rho_1 + c_1/c_2} \tag{0.61}$$

where $\rho_1, c_1$ are the density and speed of sound for the medium and $\rho_1, c_1$ are the density and speed of sound for the object. The reflection and transmission coefficients given by (0.61) are used to determine the net pressure on the interface, which is given by $P = (1+R)P_-$. Then, we can apply Newton's Second Law to calculate the magnitude of the local velocity of the interface,

$$-\nabla P = \rho \frac{\partial \mathbf{V}}{\partial t}$$
$$j\mathbf{k}_- P = j\rho\omega_- \mathbf{V} \tag{0.62}$$
$$|\mathbf{V}| = \frac{P}{\rho c} = \frac{(1+R)P_-}{\rho c}$$

where $P = P_0 e^{j\mathbf{k}_- \cdot \mathbf{r}}$ is the local pressure at position $\mathbf{r}$ on the interface and $\mathbf{V}_- = V_0 e^{-j\omega_- t}$ is the local velocity at the interface. Finally, we can solve for the local displacement, $\mathbf{D}_-(t)$, using the expression for the velocity by means of the relation,

$$\frac{d\mathbf{D}(t)}{dt} = \mathbf{V}$$
$$|\mathbf{D}(t)| = -\frac{|\mathbf{V}|}{j\omega_-} = \frac{jP}{\rho c \omega_-} = \frac{j(1+R)P_-}{\rho c \omega_-} \tag{0.63}$$

The amplitude of the resulting local displacement is proportional to the difference frequency pressure by the constant of proportionality, $\frac{1}{\omega_-}$, so that at greater difference frequencies the amplitude of the displacement decreases.

In practice, the local displacement of an object in an ultrasound field is a result of linear interaction of the incident difference frequency waves with the object and nonlinear interaction between acoustic waves and the boundary. We will consider the first effect here. The latter effect is a current topic of investigation. The analysis of all modes of nonlinear interaction between waves and boundaries is beyond the scope of this thesis. However, we made empirical measurements in experiments using pulse echo ultrasound techniques with a standard cross-correlation algorithm[133], to detect the local displacement of a silicone gel phantom when high intensity AM modulated ultrasound is applied. Colleagues in our laboratory recorded the results presented in Figure 4-14. To displace the silicone gel, we used an AM modulated signal at 3.75 MHz from a function generator (HP 33120A, Palo Alto, CA) driving two transducers positioned at 45 degrees to each other (4 cm diameter, 10 cm radius of curvature) fabricated in house from PZT4 and operating at 19 W electrical each, corresponding to a peak pressure of 3 MPa at the focus of each the primary field. For the pulse-echo detection system, we used a 1.2 MHz composite transducer triggered by a send/receive pulser (Panametrics, Waltham, MA) at a pulse repetition rate of 2.5kHz. The minimum detectable displacement for this system is 8 μm based on the acquisition sample rate of the echo ultrasound measurement system. We plot the experimentally measured displacement of the silicone gel interface as a function of frequency of modulation in Figure 4-14 (experimental values indicated by *). We also plot the simulated displacement (solid line in Figure 4-14) using equation (0.63) and normalizing the peak to the experimental data. The plots demonstrate a $\frac{1}{\omega}$ relationship for the experimentally measured displacement.

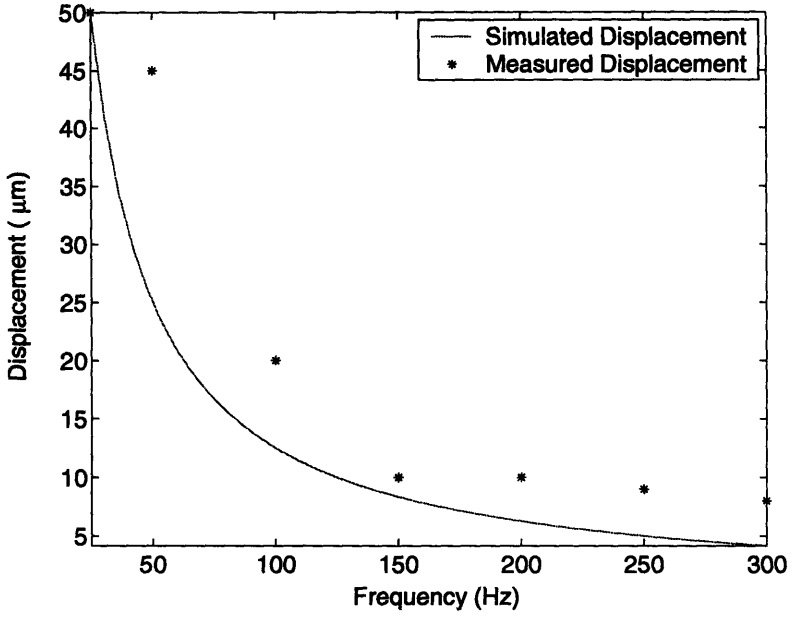


**Figure 4-14:** Experimentally measured displacement of a silicone gel interface as a function of difference frequency. The result is plotted together with a simulation of the displacement using equation (0.63), which is normalized to the experimental results. The simulation illustrates frequency dependence of experimental data.

Greenleaf's group reports similar displacements, as large as 50μm, of stainless steel spheres embedded in a gel and positioned at the focus of a dual-frequency system[119]. In addition to pulse-echo ultrasound, they use a laser vibrometry detection method to measure the displacement. Although these disturbances seem relatively large on an acoustics scale, we show below that they are insufficient to produce a measurable signal at the difference frequency.

In equations (0.62) and (0.63), we estimate the displacement at the interface caused by scattering from a planar target. Alternatively, we can consider the radiation from a moving target and calculate the displacement of the target interface necessary to produce a measurable field at a given frequency. From the scattering point of view, this approach is equivalent to calculating the reflection from an infinitely soft interface (a pressure release surface)[xviii]. We use the simple model of a baffled planar disc radiator of dimensions equal to the focal dimensions of the primary field to estimate the displacement necessary to produce a difference frequency signal just above the amplitude of the system noise. This model uses the equation for on-axis pressure due to the harmonic motion of a baffled disc radiator[78,128],

[xviii] We note that a rigid target also generates a scattered field even though the interface does not move.

$$P(r) = \tfrac{1}{2}\rho_0 c U \tfrac{a}{r} ka \tag{0.64}$$

where $\rho_0 = 998 kg/m^3$ is the ambient density of the medium, $c = 1500 m/s$ is the speed of sound of the medium, $a = .5mm$ is the radius of the disc, $k = \frac{\omega}{c}$ is the magnitude of the wave vector, and $r$ is the distance from the radiator in meters. Equation (0.64) is valid in the far field for $\frac{r}{a} \gg 1$ and $\frac{r}{a} \gg ka$.

We use (0.64) to calculate the displacement as a function of difference frequency necessary to produce a sound pressure $P(\mathbf{r}) = .1\,Pa$ at $|\mathbf{r}| = 10\,cm$ from the moving disc. The pressure of .1 Pa is the minimum pressure amplitude detectable, because it is just above the amplitude of the noise for the system. The result, plotted in Figure 4-15 for the same range of frequencies at which the displacement was measured in Figure 4-14, demonstrates that a displacement on the order of 500 μm is required to produce a difference frequency sound at 150 Hz which can be detected. In the high power, low frequency experiment of Figure 4-14, the motion is approximately 50 times too small to generate (or be the result of) a detectable sound field.

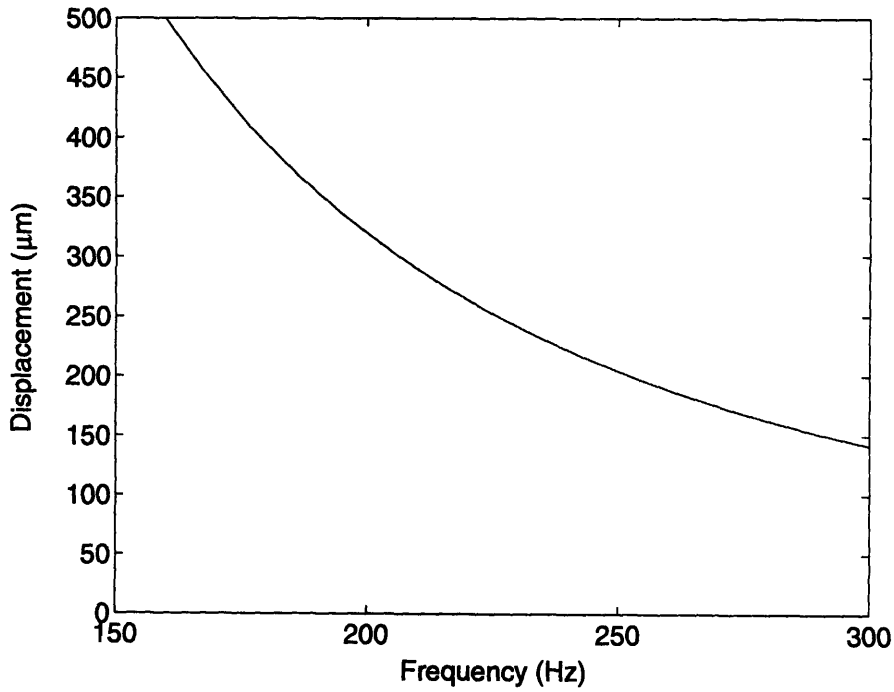


**Figure 4-15:** Simulated displacement as a function of frequency of a 1mm diameter disc radiator. The plot illustrates the displacement needed in order to generate a measurable difference frequency sound level of .1 Pa at 10 cm from the source.

The results of the simulations in this chapter for the incident difference frequency field scattered from small spherical targets and planar reflectors (Figure 4-10 through Figure 4-13) reveal scattered pressure levels in the μPa range and lower. Given the noise amplitude for the experimental set-up, provided in Table 1-1 (noise amplitude = .1 Pa), and the sensitivity of the measuring equipment, signals this small would not be detectable in experiments designed to isolate this mode of difference frequency sound generation. For the case of spherical scatterers, the field can be observed to decay like $\frac{1}{r}$ as the distance $r$ from the scatterer increases due to the divergence the pressure field as it spreads. For the planar reflectors considered, the reflected difference frequency signal is larger than the scattered field from the spherical targets, but it still does not reach a measurable level.

## 4.3 Experiments

We experimentally measured the difference frequency sound due to the reflection of two primary fields from the surface of an object and the subsequent scattering of this difference frequency field. Multiple measurements were made of the response from the center and surface of silicone gel tissue phantoms and compared to the response from the interaction of the primary fields without a target in the field. We conducted the experiments at the highest possible powers while still avoiding cavitation and also with very short pulse bursts to prevent the interaction of reflected waves with the transducers (a topic called the parametric effect as discussed in chapter 3). The experimental results confirm the conclusions from simulations in section 4.2 that no difference frequency signal is detectable.

### *Direct Local Force Measurements*

Before measuring the difference frequency sound generated by the reflection from the target, we performed a preliminary experiment to study the local force on objects. For this experiment, we placed a pin at the focus of the concentric element system driven at several very low difference frequencies and recorded the force on the pin (Figure 4-16). In similar experiments, McNamara and Beyer reported measuring the "time varying" radiation pressure from a single element modulated sinusoidally (a parametric array) using a condenser microphone for the receiver.[134] However, we are not aware of any previous direct measurements of the time varying force from two separate elements interacting on a target.

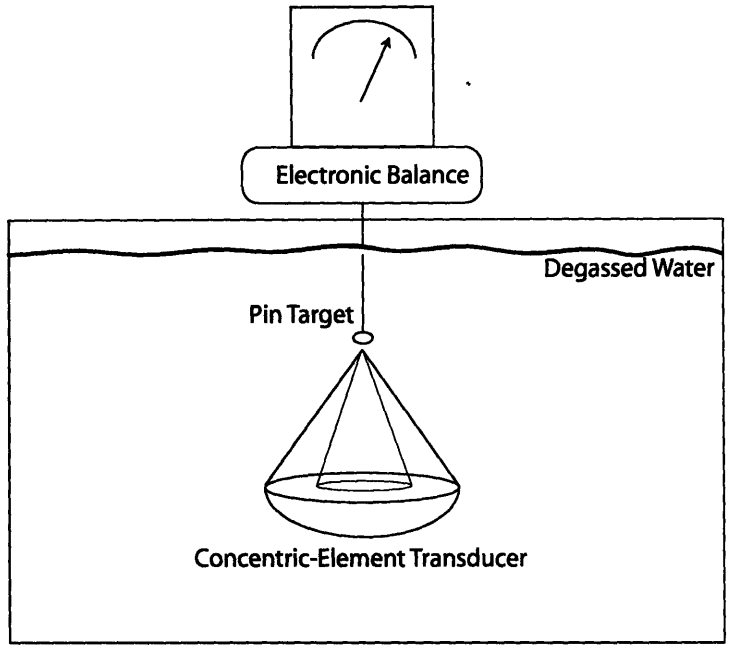


**Figure 4-16:** Diagram of the experimental set-up used for the direct measurement of an oscillating force created by a dual-frequency pressure field incident on the 1mm diameter head of a steel pin.

A 14 element concentric ring transducer was used in which rings 2 through 8 were driven together at (1.54 + Δf) MHz while rings 9 through 14 were driven together at 1.54 MHz (ring 1 was not powered). This transducer was used because it has minimal mechanical coupling between the elements as compared to the two-element concentric ring transducer described earlier. Eliminating the coupling ensures that the elements do not drive one another, creating a parametric array which might result in an incident difference frequency that could cause the cyclical forces. For the experiments measuring the oscillatory force at the difference frequency, the transducer was positioned under the water surface and pointed upwards at a small steel target (1 mm diameter pinhead) secured to a computer controlled electronic balance (Metler Toledo PR2003, Columbus, OH). The continuous wave (CW) driving signals were obtained from two function generators (HP 3120A, Palo Alto, CA) each driving an amplifier providing 50 dB gain (ENI 1200L and ENI 3100L, Rochester, NY). The output power was 20 W electrical per element, corresponding to a peak pressure of 5.7 MPa at the focus of each primary field. In order to direct the acoustic waves away from the water surface and thereby to eliminate standing waves, a cone-shaped reflector surrounded by an angled pad of absorbing rubber were positioned around the 1mm target so that the 1mm target could swing freely while surrounded by the absorption apparatus. We recorded force measurements as a function of time with the two elements driven at slightly different frequencies.

The experiment was conducted at very small difference frequencies due to the slow response time of the scale and was repeated for several values of the difference frequency, Δf.

This results of this initial experiment, plotted in Figure 4-17, demonstrate the oscillating force measured by the electronic scale as a function of time at a difference frequency of Δf = .067 Hz, .17 Hz, .23 Hz, and .31 Hz respectively. Note that the amplitude of the force increases slightly with decreasing difference frequency. This may be attributed to the very low natural frequency of the scale and associated electronics, which do not update quickly enough to follow even these slowly changing forces. There are several competing theoretical explanations of this relatively large oscillating force and a thorough investigation of these mechanisms is beyond the scope of this thesis. However, the results of the experiment are included to report this nonlinear effect on the target we measured empirically. Regardless of the mechanism responsible for this measured force, the simple simulation above of a disc radiator the size of the pinhead illustrates that forces of this magnitude (or the corresponding displacements in the medium cause by forces of this magnitude) are insufficient to account for a measurable difference frequency field in the tank.

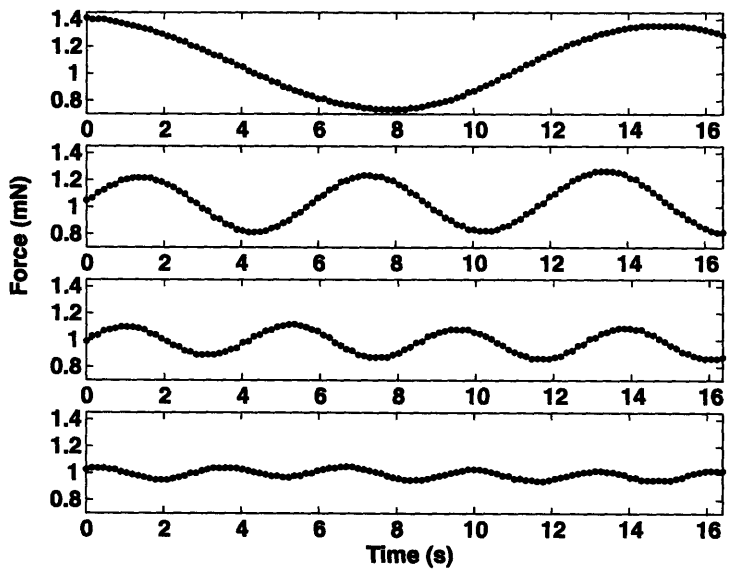


**Figure 4-17:** Experimentally measured force vs. time result from sonicating a 1mm target at a difference frequency of .067 Hz (top), .17 Hz (2nd row), .23 Hz (3rd row), and .31 Hz (bottom).

*Experiments to Validate Simulated Interaction of Primary Fields*

Before performing experiments to measure the difference frequency response of the silicone gel targets, we measured the field resulting from the interaction of the two primary beams in order to check the simulations of these primary fields. This is an important first step because the

reliability of the above simulations which predict an immeasurable difference frequency sound for all cases of local interaction with a target are contingent upon the accuracy of the simulated primary fields. For these experiments, a .075mm PVDF needle hydrophone (Precision Acoustics, Dorchester, UK) was scanned through the focal plane of the field created by the concentric element transducer. The measured signal was registered to a digital oscilloscope (Yokogawa DL7100, Japan) and recorded to a personal computer via a GPIB IEEE-488 connection. The hydrophone was positioned by means three-dimensional positioning system (Velmex Unislide NF90, Bloomfield, NY), which was controlled by the same computer via an RS-232 connection to the serial port. The experiment was repeated for the separate-element system with the transducers positioned at both 25 degrees and 50 degrees between centers.

The result of the simulation of the combined linear pressure field due to ultrasound radiation from an inner and outer transducer is a time-dependant pressure field given by the sum of the fields from the two separate elements. The pressure field varies in time due to the summation of the two fields according to the relation given in equation (58) above. Column A of Figure 4-18 shows the amplitude of the simulated combined pressure field in the focal plane at 0 degrees and 180 degrees relative phase. The field varies in time from the normal Gaussian-shaped focus of a spherical-cap transducer to a pattern of concentric rings of pressure. In the center point of the focal plane, the fields from the two elements cancel when the two fields are at 180 relative phase.

In column B of Figure 4-18, the amplitude of the experimentally measured pressure field from a concentric element transducer with the same geometry as the one simulated is displayed at the same 2 time points. The geometries of the simulated and experimentally measured fields agree relatively well. For this transducer, the distance between concentric rings of peak pressure in the simulation is 1 mm (1.15*$\lambda$), which is nearly the same as the measured distance between concentric rings of peak pressure in the experimental data.

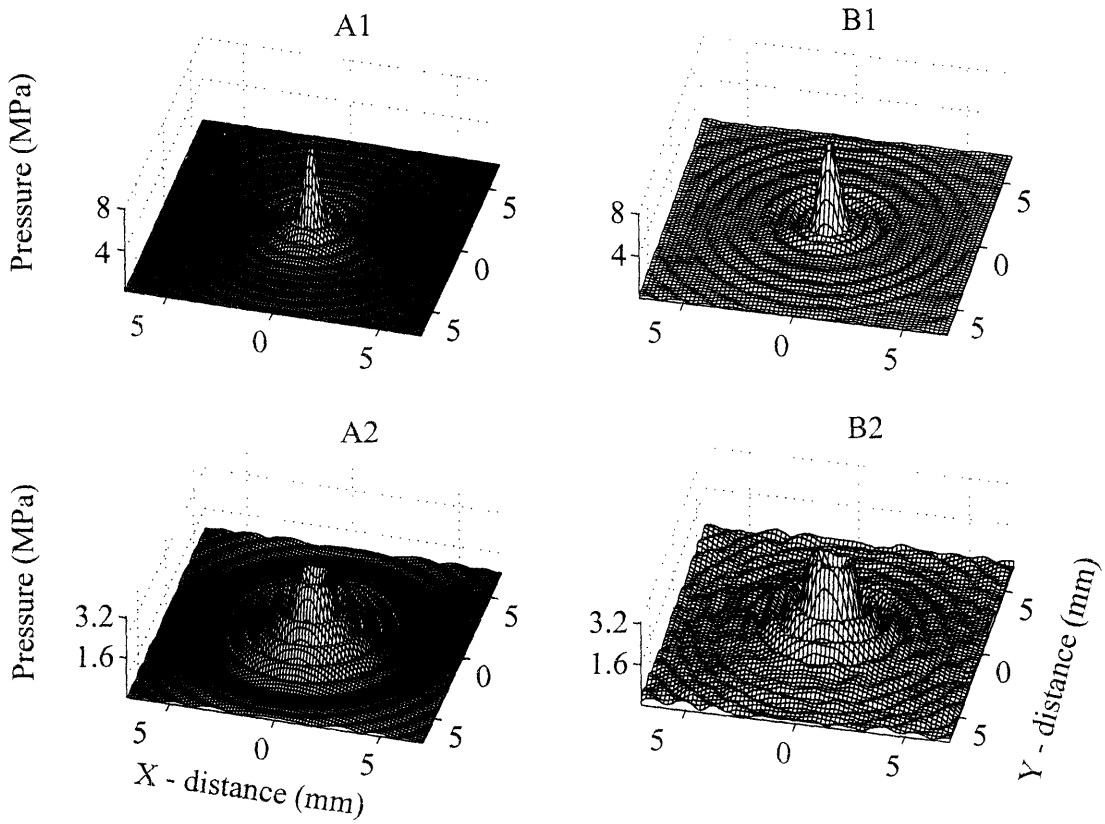


**Figure 4-18:** Simulation and experiment of the combined pressure field generated by a concentric element transducer with F-num = .8. The figure shows the result of the simulation (column A) and experiment (column B) at 0 relative phase (row 1) and 180 relative phase (row2) of the two primary fields.

The combined pressure field from two separate elements varies in time in a similar manner as the concentric ring transducer. In this case, the pressure field in the focal plane forms a pattern of vertical stripes of alternating peak and zero pressure. This grading lobe pattern from two focused elements is demonstrated in the results for the simulation of $P_T$ (Figure 4-2). This plot represents the amplitude of the total pressure field in the focal plane at time points corresponding to 0 degrees and 180 degrees relative phase of the two elements. The elements are positioned at an angle of 50 degrees between the two element centers.

In Figure 4-19, the amplitude of the experimentally measured linear summed pressure field from a separate element system with the same geometry as the one simulated in Figure 4-4 is displayed at the same two time points. This field represents the source term driving the second order wave equation. There is good agreement between the geometry of the simulated and experimentally measured fields. For this transducer and separation angle of 25 degrees, the distance between vertical lines of peak pressure in the simulation and experiment is .67 mm (1.18*$\lambda$).

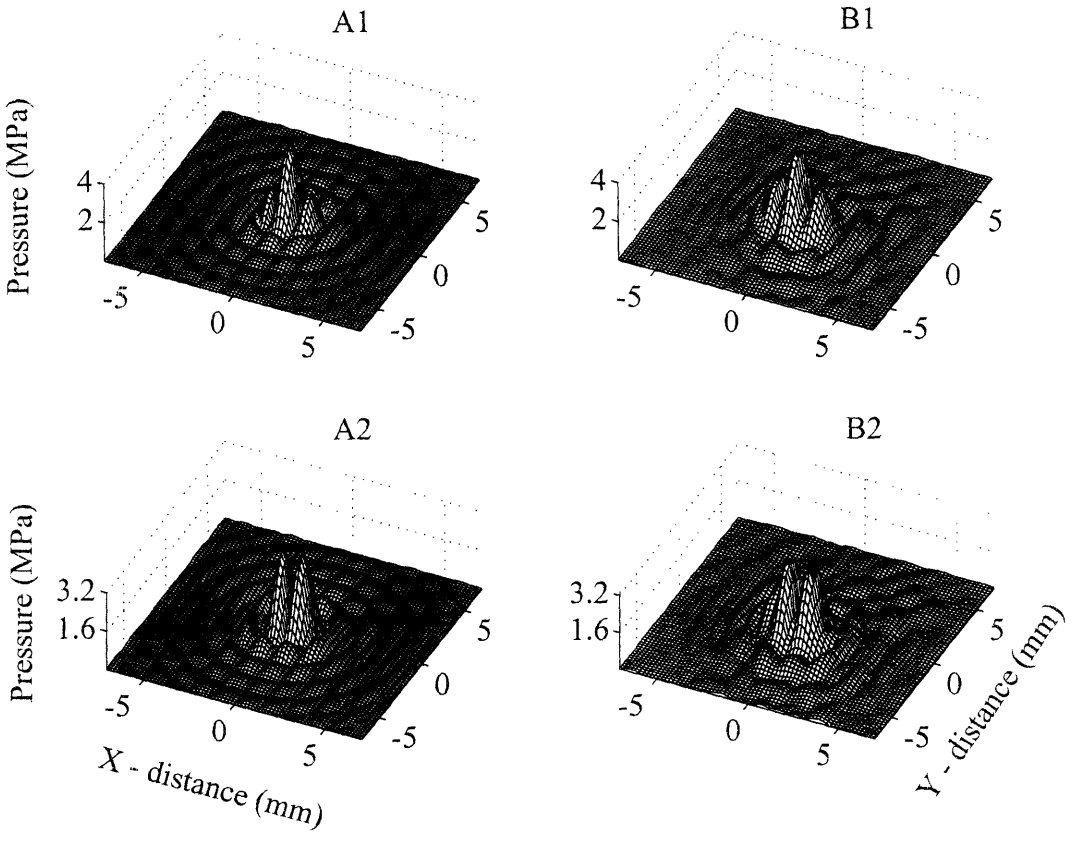


**Figure 4-19:** Simulation and experiment of the combined pressure field generated by separate elements angled at 25 degrees. The figure shows the result of the simulation (column A) and experiment (column B) at 0 relative phase (row 1) and 180 relative phase (row2) of the two primary fields.

The same type of simulation and experiment are repeated for the two elements positioned at 50 degrees between centers in Figure 4-20. Again, the correlation between simulated and experimentally measured linear summed fields is reasonable, both indicating the characteristic striping pattern of the pressure field due to the interference of the two primary fields. The interference pattern for an angle of 50 degrees contains a greater number of stripes of in-phase pressure with a finer spacing between them.

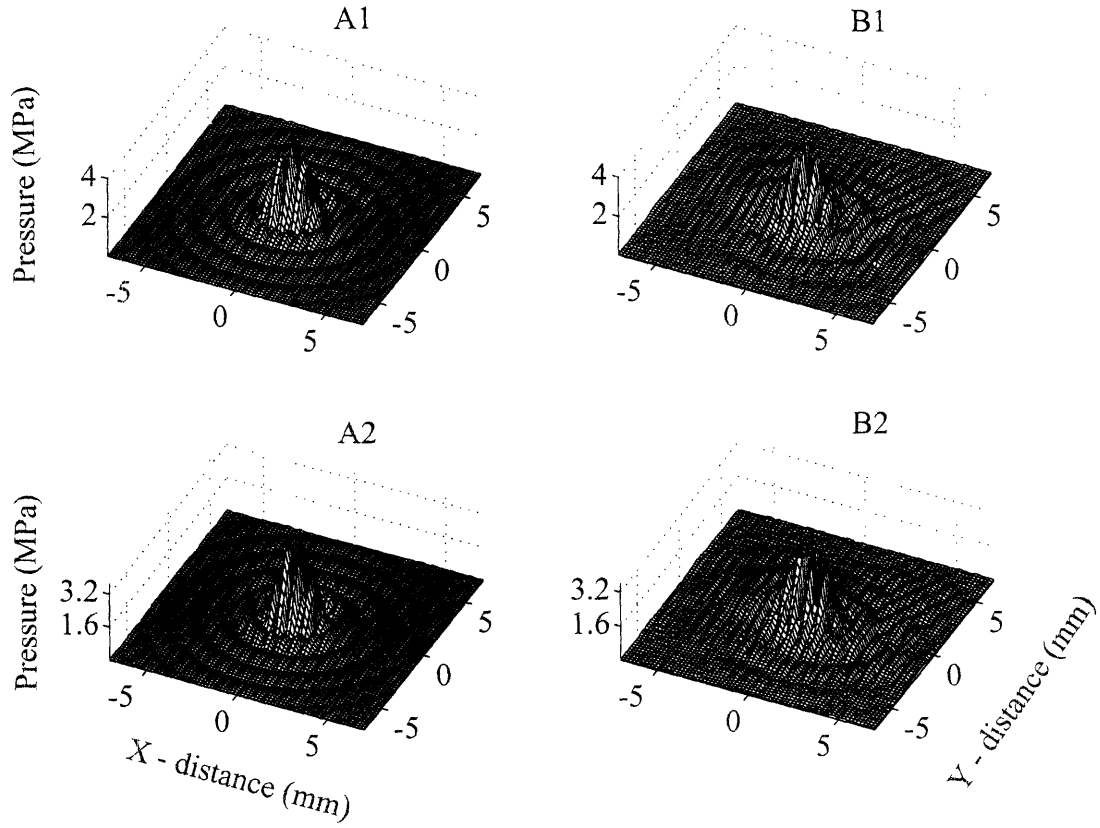


**Figure 4-20:** Simulation and experiment of the combined pressure field generated by separate elements angled at 50 degrees. The figure shows the result of the simulation (column A) and experiment (column B) at 0 relative phase (row 1) and 180 relative phase (row2) of the two primary fields.

Figure 4-21 is a photograph taken of the displacement due to the two separate elements intersecting at the air-water interface. This photograph is presented to visualize the vertical lines of pressure. Of course, due to water surface tension, the displacement does not return to zero between the pressure peaks at the lines of zero pressure. The result for the air-water interface is a smoother version of the ridges of in-phase pressure presented in the above simulations and direct pressure measurements.

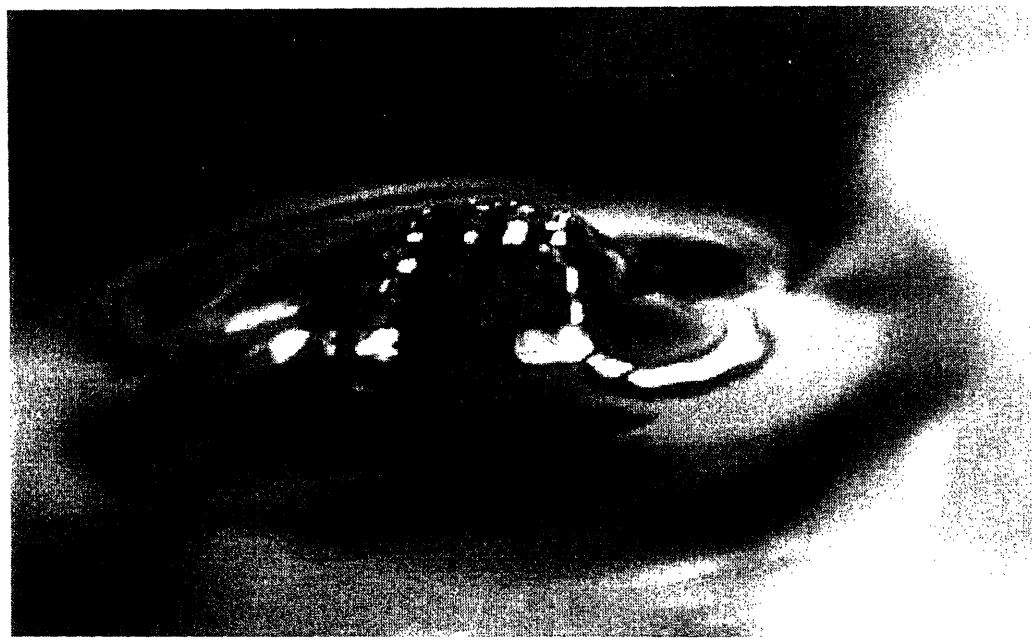

**Figure 4-21:** Photograph of the displacement at the water surface caused by the combined acoustic fields from two separate elements.

*Gel center vs. Outside Gel experiments at 3$^{rd}$ harmonic and 5$^{th}$ harmonic*

In order to compare the signal from the center of the gel to that of no target at all in a rigorous manner, we conducted a series of experiments in which 100 measurements were acquired with the intersecting foci positioned at the gel center and 100 measurements were acquired with the intersecting foci positioned the same distance in front of the gel surface as it had been behind the gel surface (see Figure 4-22). We position the focus equidistance behind and in front of the front surface of the gel for the respective experiments in order to control for the scattering of waves from the gel surface. The geometry of the pressure field produced by a focused transducer is similar just before and just after the focal plane. Therefore, some slight interference effects of the pressure field with the gel interface could be controlled by positioning the focus equidistance in front of and behind the gel interface.

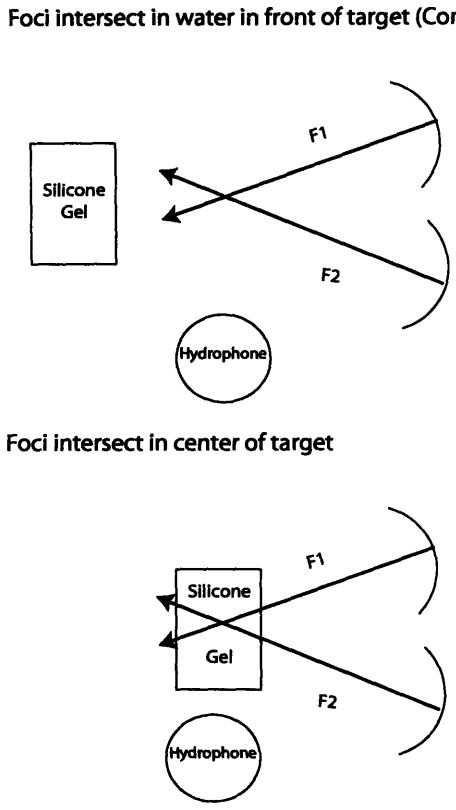


**Figure 4-22:** Diagram of the experimental set-up used for detecting the generation of a difference frequency response from the center of a silicone gel tissue phantom.

We took steps to try to maximize any possible signal originating from the gel center caused by a local difference frequency pressure effect. We conducted the experiment at the third harmonic (1.624 MHz) of the transducer with a pulse period of 880 msec, duty cycle of 10%, and power of 16 W electrical per element, corresponding to a peak pressure of 2.7 MPa for each primary field. This power represented the greatest amplitude possible before thermal effects occurred in the target silicone gel. The measurements were made for a difference frequency of 100, 300, 500, 700, and 900 Hz. The dual channel filter was set to allow the frequencies from 80 Hz – 20 kHz to pass through.

We repeated the experiment at the 5$^{th}$ harmonic of the transducers (2.74 MHz) in order to obtain a tighter focus, greater absorption coefficient, and a reduced threshold for cavitation. At this frequency, the period remained the same, but the duty cycle was decreased to 2% (five times smaller than previously) so that the power could be increased to 29 Watts electrical per element (corresponding to a peak pressure of 3.5 MPa for each primary field) without thermal exposure effects in the gel. The dual channel filter was more tightly tuned in this series of experiments at the 5$^{th}$ harmonic to allow frequencies between 85 Hz and 2 kHz to pass through. Similar to the 3$^{rd}$

harmonic experiments, the measurements at the 5th harmonic were repeated for difference frequencies of 100, 300, 500, 700, and 900 Hz. For the experiments at the 5th harmonic, the forward and reflected power signals were detected by the dual-directional coupler. We monitored this signal to ensure that there was no transducer-to-transducer interaction present.

In the first experiment, the response from the gel center was compared to control (the water in front of the gel) at various difference frequencies. The results, plotted in Figure 4-23, show nearly identical amplitudes of the response from the gel center and control. In particular, the response is very small and is below the noise floor for the system. If the local difference frequency pressure were the cause of this small difference frequency response, we would expect the response from the gel center to be much greater than that from no target at all (control). However, we see in this experiment, that the gel and control measurements are nearly the same amplitude and in particular are within one standard deviation of the measured system noise amplitude as indicated in Table 1-1.

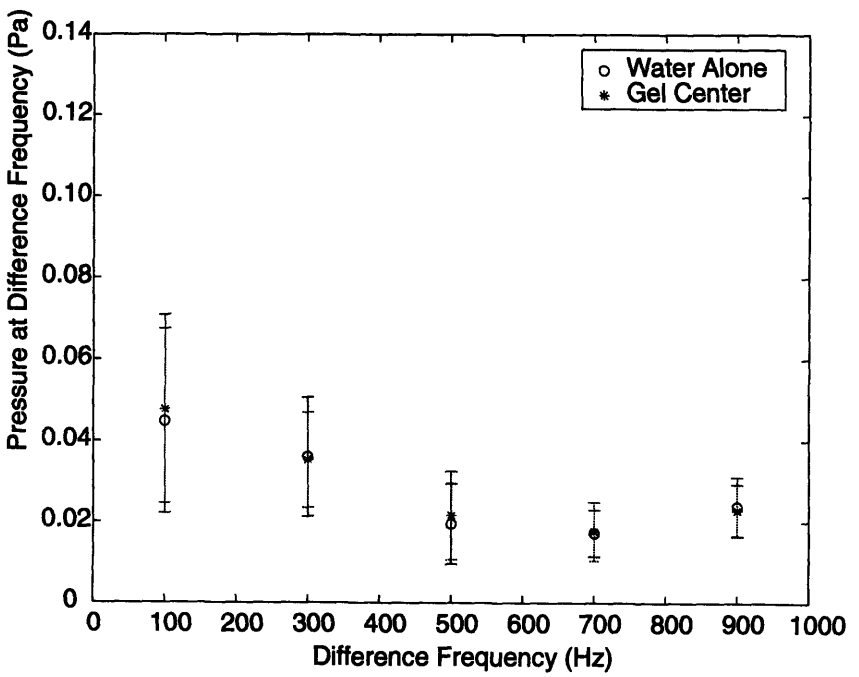


**Figure 4-23:** Experimentally measured difference frequency generated from the gel center vs. control for scans at the 3rd harmonic. The plot shows the mean and standard deviation of the measurement at each frequency.

The experiment testing for difference frequency response was repeated at even higher power levels by using the 5th harmonic of the primaries, which allows for a greater cavitation threshold. The results of the 5th harmonic experiment, plotted in Figure 4-24, and the results of the 3rd harmonic case lead to the same conclusion: the signal is the same as the control. Even with conditions optimized for difference frequency sound generation including the use of 29 W per

element electrical power for the primary beams (corresponding to a peak pressure of 3.5 MPa for each primary field), the recorded signal is still with-in the standard deviation of the noise as measured for this system in Table 1-1.

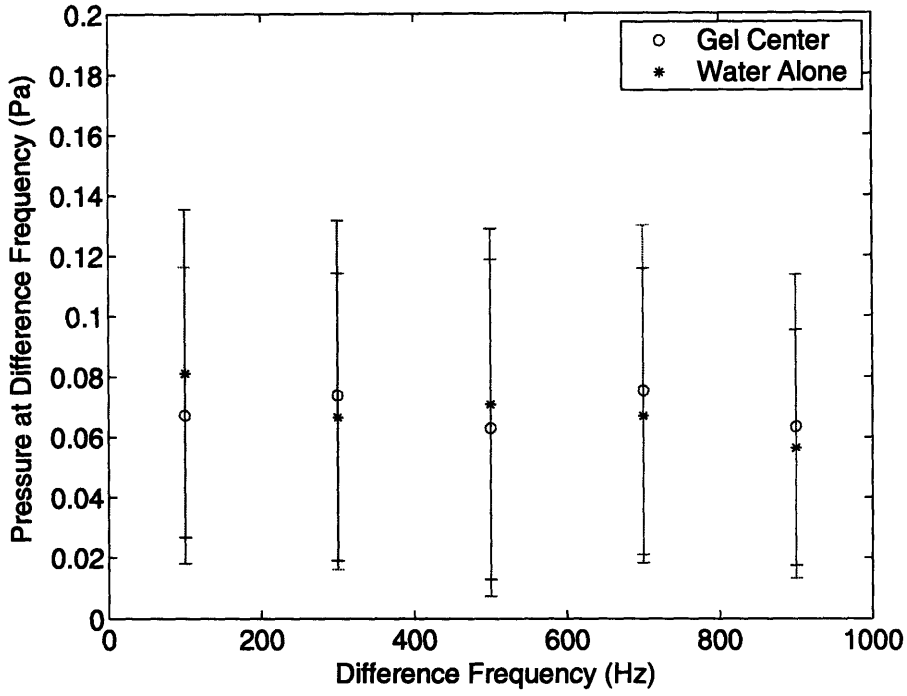


**Figure 4-24:** Experimentally measured difference frequency generated from the gel center vs. control for scans at the 5$^{th}$ harmonic. The plot shows the mean and standard deviation of the measurement at each frequency.

### *Interface of Polyethylene Plate and Silicone Gel Phantom*

We conducted experiments to determine if local pressure at the difference frequency could reflect from a silicone gel or a polyethylene plate to produce detectable signals at the difference frequency. The experiments were simulated in the first part of this chapter (see Figure 4-12 and Figure 4-13). In these experiments, the interface of a planar target was oriented to eliminate any interaction of the reflected beam with the transducers themselves to avoid their collinear interaction as discussed in chapter 3. We used separate transducers operating at 2.74 MHz and positioned at an angle of 60 degrees to each other. The two transducers pulsed at a power of 10 W electrical per element (corresponding to a peak pressure of 2 MPa for each primary field) and at a difference frequency of 30 kHz with a period of 75 msec and a duty cycle of 20%. The acoustic response was recorded by the low frequency hydrophone (International Transducer Corporation ITC-6050C, Santa Barbara, CA) and the signal was captured and digitized by the oscilloscope (Yokogawa

DL7100, Japan). The measurements were repeated for a total of ten pulses at each position as the planar target was rotated through several angles ranging from 101 degrees to 110 degrees (Figure 4-25).

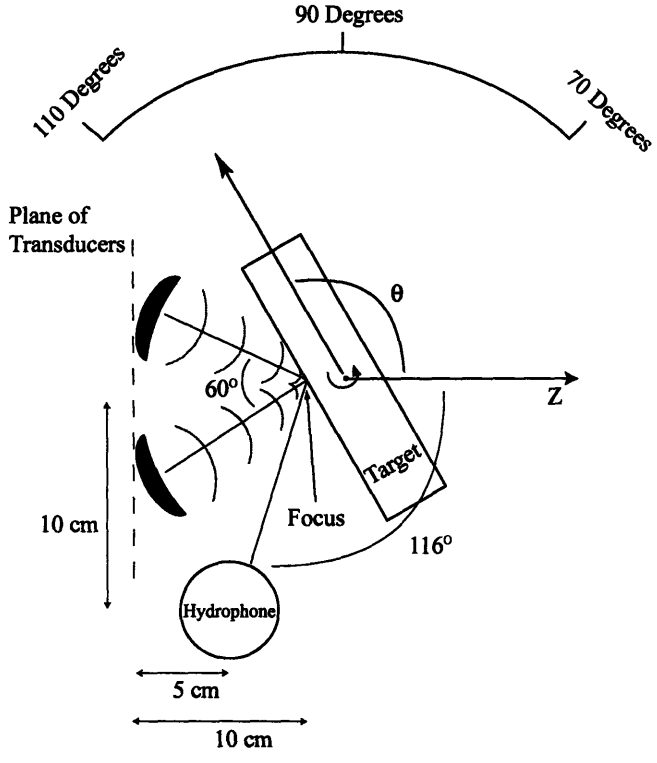


**Figure 4-25:** Diagram of experimental set-up used to measure the reflected difference frequency field from the interface of a planar target.

The result of the reflection of the incident field from the interface of the polyethylene plate is plotted in Figure 4-26. The result shows that the recorded difference frequency signal is well below the noise floor for the system at all angles of the interface. The background noise is lower in this case since the filtering of signals below 1kHz allows for more sensitive measurements to be made and eliminates many common laboratory noises. Despite this decreased system noise amplitude, the signal from the polyethylene plate is still undetectable for this experiment.

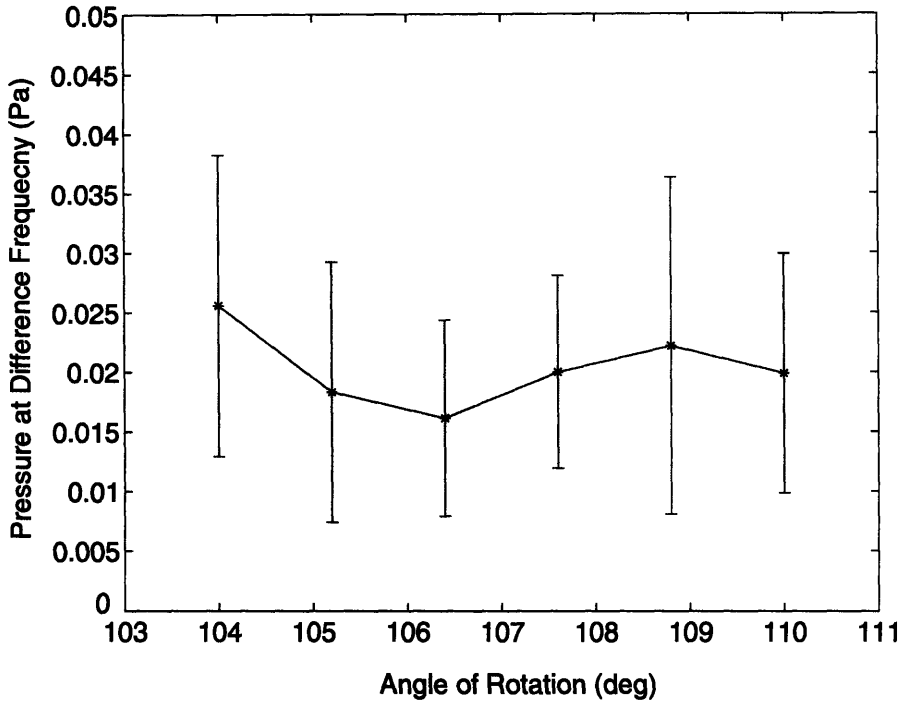


**Figure 4-26:** Experimentally measured difference frequency from a water-polyethylene interface. The plot shows the mean and standard deviation of the measurement at each frequency.

Finally, we plot the results from measurements of the difference frequency pressure due to the interaction of the two primary beams from separate elements on the interface of the silicone gel in Figure 4-27. Again, the pressure amplitude is at the noise amplitude and cannot be distinguished from system noise.

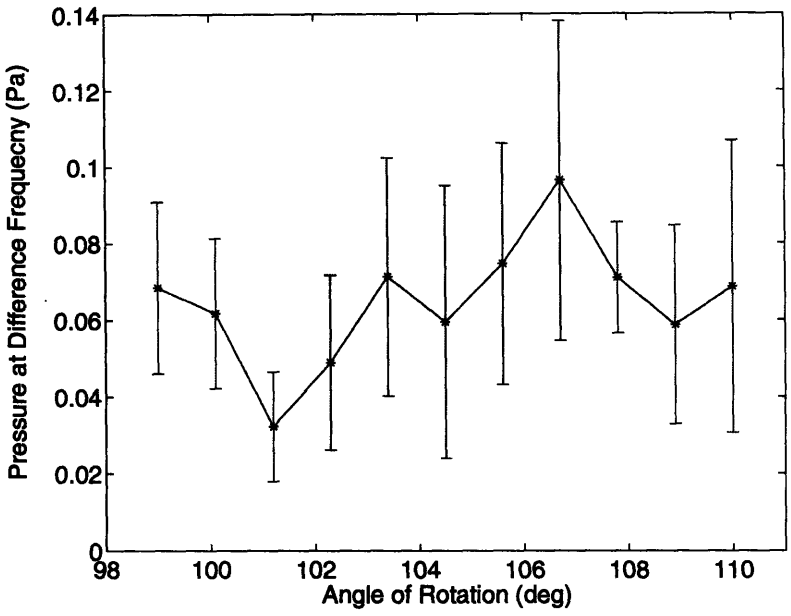


**Figure 4-27:** Experimentally measured difference frequency from a water-silicone gel interface. The plot shows the mean and standard deviation of the measurement at each frequency.

## 4.4 Conclusions

Simulations and experiments in this chapter suggest that the generation of difference frequency sound due to the scattering of a local difference frequency field from various targets is not readily detectable given the sensitivity of experimental equipment used in this thesis. We performed simulations to estimate the sound generation at the difference frequency using the second order wave equation together with linear scattering theory. The calculated levels of difference frequency sound ranged from $1 \times 10^{-8} Pa$ for the case of the single pressure release sphere to $30 \times 10^{-6} Pa$ for the silicone gel tissue phantom. Experimental results demonstrate that although small displacements on the order of $50 \mu m$ were detected at the interface of the silicone gel tissue phantom, these displacements did not lead to a measurable difference frequency field at 10 cm from the target.

The main reason for the undetectable radiated difference frequency field is the localization of the nonlinear sound generation to the small region before the interface of the target. In contrast to the parametric effect described previously in chapter 3, for the local interaction effect described here, the primary fields do not propagate collinearly. Therefore the difference frequency sound does not continue to grow with propagation distance. Instead, the difference frequency sound generated in the limited interaction region of the two primary beams leaves the interaction region

and promptly decays at an exponential rate as it diverges in space. This effect can be understood in terms of the second order wave equation in that the source terms on the right hand side of this equation exist only over a very limited volume in space because the interaction region of the two beams at the focus is on the size scale of the primary wavelengths. This creates a collection of sources radiating at the difference frequency and contained within a volume much smaller than the difference frequency wavelength. This can be seen as a compact source for the difference frequency field. As a result, the pressure will fall at $\frac{1}{r}$ as the observer moves away from the source. Further, as the simulations and experiments of the linear summed fields demonstrate, there are many phase reversals of the primary field and the difference frequency field over the small interaction region. The phase reversals over a region much smaller than a single difference frequency wavelength may cause cancellation of pressure at the interaction region, resulting in even less propagating sound.

The experiments and simulations performed in this chapter do not rule out the possibility of generating difference frequency from the local interaction of difference frequency pressures with an object. In contrast, nonlinear boundary interactions not simulated in this thesis may cause measurable difference frequency radiation[94]. However, the experiments confirm that for transducer geometries, target materials, and power levels used in this thesis, no difference frequency sound was detected from the interaction of the incident difference frequency pressure field with the target.

# 5 Nonlinear Interaction of Linearly Scattered Waves

Makris *et al.* analytically studied the effect of difference frequency sound generation from linearly scattered primary waves for non-collinear plane waves incident on a target as a potential mechanism for the generation of difference frequency sound in USVA.[94] This study prompted our exploration of the nonlinear interaction of primary waves, which are first linearly scattered from small gas bubbles or pressure release spheres located at the focus of the primary fields[xix]. In this chapter, we follow a similar analytical approach at the difference frequency but consider incident focused ultrasound beams rather than plane waves.

This thesis explores the nonlinear production of difference frequency sound in a dual-frequency imaging system for monitoring thermal surgery. Although cavitation has recently been explored as a method to enhance heating for thermal surgery[135,136], for this thesis we typically used power levels below the cavitation threshold in order to avoid the difficulties in controlling the temperature during cavitation events. However, in a few instances, cavitation did occur while creating lesions during our imaging experiments, as indicated by broadband noise received by the hydrophone. During experiments in which cavitation occurred, we observed a large difference frequency response from the tissue of up to 30 Pa. Small air bubbles, which may arise during cavitation, are potential scatterers of the incident beams and may explain the observation of large difference frequency sound generation in the presence of cavitation if considered in the context of the nonlinear interaction of linearly scattered waves.

In this chapter, we first present experimental images created using the difference frequency signal after cavitation has occurred while making a thermal lesion in *ex vivo* rabbit liver. Then, we review the theory of difference frequency sound generation due to the nonlinear interaction of linearly scattered waves. Finally, we calculate the difference frequency field for the case of a single

---

[xix] Other researchers including Jones, Bellin and Beyer[137] [58,142] as well as Roy[56] published theoretical and experimental results for the generation of a signal at the sum frequency due to the nonlinear interaction of linearly scattered waves. In general, signals generated at the difference frequency are more difficult to measure in experiments. This is due to the increased system noise at these relatively low frequencies (kHz range), as well as the fact that the nonlinear signal is smaller at the difference frequency since it is proportional to the wave number $k_{\pm} = \frac{\omega_{\pm}}{c}$, which is smaller for the difference frequency than the sum frequency.

pressure release sphere and an air-filled bubble. The experimental results demonstrate rather large difference frequency responses (as high as 30 Pa) from the tissue when imaging a thermal lesion after cavitation has occurred. The simulation results rely on a model for scattering from a single bubble and demonstrate a small but measurable signal at the difference frequency (as high as .2 Pa). In simulations, we demonstrate that the efficiency of the difference frequency response is especially large if the diameter of the spherical target is the resonant size corresponding to the primary field.

## 5.1 Initial Experiments

In this section, we present our initial *ex vivo* tissue experiments. These experiments reveal a measurable difference frequency response from imaging *ex vivo* rabbit liver in the presence of cavitation.

### *5.1.1 Imaging Thermal Lesions in Ex Vivo Rabbit Liver*

An image of a 10mm by 10mm area of fresh, *ex vivo* rabbit liver was created by recording the response at the difference frequency while scanning the focus of a concentric-element, dual-frequency system across a plane of the tissue sample at a depth of approximately 5 cm in the tissue. The transducers operated at $1.624 MHz \pm 5 kHz$ and were driven at a power of 10 W electrical per element to create a peak pressure at the focus of approximately 2 MPa for each primary field. The focal plane was scanned in a raster pattern, which was created by mechanically stepping the focus of the two transducers through a 10mm x 10mm grid with a step size of .5mm (Figure 5-1). The positioning system (Velmex Unislide NF90, Bloomfield, NY) was operated by computer control via a IEEE-488 GPIB interface and the response signal was recorded with a low frequency hydrophone (International Transducer Corporation ITC-6080C, Santa Barbara, CA) located approximately 10 cm away from the focus. The response signal was then registered to an oscilloscope (Tektronix TD210, Beaverton, OR) and recorded by a personal computer via a IEEE-488 GPIB computer interface.

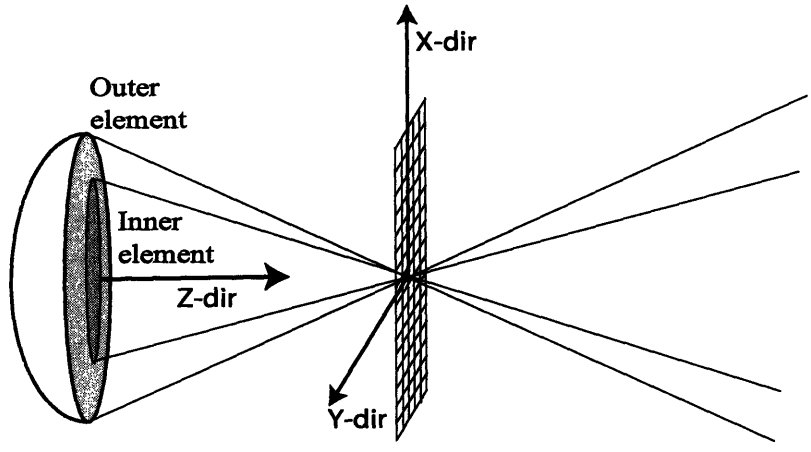


**Figure 5-1:** Diagram of the experimental set-up used for the raster scan of *ex vivo* rabbit liver.

In this experiment, we imaged the liver with the dual-frequency system, created a lesion of thermal ablation, allowed the sample time to cool, and finally re-scanned the liver with the imaging system. The results of the pre-sonication and post-sonication scans are plotted in Figure 5-2. The image created from scanning the tissue before the lesion of coagulative necrosis was formed (top, right-hand plot of Figure 5-2) demonstrates a homogenous difference frequency response at relatively small pressure amplitude. After this preliminary scan, we created a lesion by sonicating at the center of the scanned area with 40 W electrical power (generating approximately 8 MPa of peak pressure at the focus) for 20 seconds. During the formation of the lesion, we detected a broadband frequency response as measured by the hydrophone in the tank. This broadband signal indicates that cavitation was most likely occurring during the formation of the lesion[129]. Finally, after forming the lesion, we re-scanned the tissue in the same manner as before. The result of the scan created after the lesion had been formed (lower right-hand plot of Figure 5-2) reveals a much larger difference frequency response (up to 9 Pa) as compared to the pre-lesion image (top, right-hand plot of Figure 5-2). The larger difference frequency response of the second scan is received while scanning a region of the liver that corresponds reasonably well to the geometry of the thermal lesion that was created. Figure 5-2 displays photographs of the healthy liver (top) and necrosed liver (bottom) that were taken after the liver was dissected to expose the focal plane of the dual-frequency system.

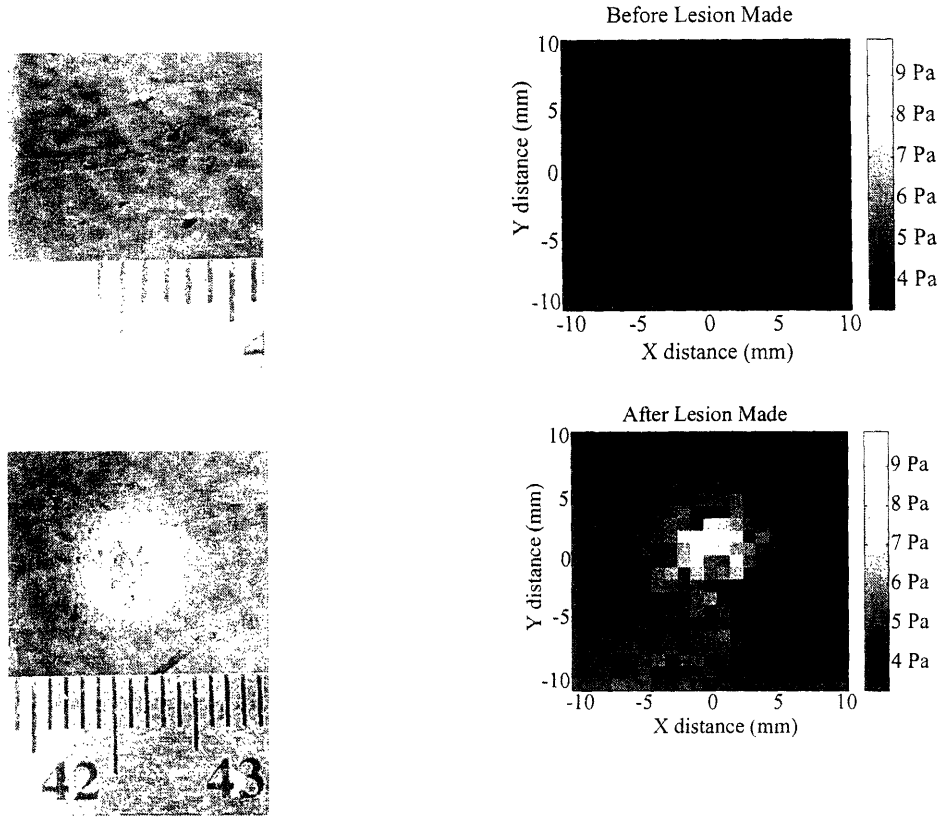


**Figure 5-2:** Experimentally measured difference frequency generated during an x-y scan of fresh *ex vivo* rabbit liver before (top) and after (bottom) the tissue was necrosed with high-powered focused ultrasound.

These experimental results reveal a measurable difference frequency signal that corresponds to the area of the thermal lesion, as observed visually in the photographs of the lesion. The response at the difference frequency reached a peak level of 9 Pa, which is readily detectable given the amplitude of the system noise and the sensitivity of the measuring equipment. We hypothesize that this difference frequency signal is due to the presence of the gas bubbles from cavitation, and that the mechanism of generating the response signal is related to the nonlinear interaction of linearly scattered waves from these gas bubbles as described in the theory section below. More thorough experimental investigation is required to confirm our hypothesis.

Next, we present a second example of imaging with the dual-frequency system after causing cavitation while creating a thermal lesion. In this example, we scanned an area of 30mm by 30mm in fresh rabbit liver after forming a pattern of necrosis using high power sonication (40 W electrical, 8 MPa peak pressure) to the tissue. This liver sample was taken from a different animal than the liver used in the above example. In this case, we created two large bands of necrosis and

two point lesions in the liver by moving the transducer slowly while sonicating at high power, in order to necrose the tissue. Again, we observed broadband signals indicative of cavitation on the oscilloscope during the formation of the lesions. The step size of the area scan was .5 mm in each direction. In this case, we recorded multiple measurements at each position of the imaging system focus in order to use the average over multiple response signals to refine the image.

Figure 5-3 displays the result of the scan after the formation of the pattern of lesions. The right-hand image is formed by plotting the amplitude of the difference frequency signal averaged over 4 consecutive measurements for each location in the liver sample. The peak difference frequency pressure measured is approximately 30 Pa. The left-hand image is a photograph of the pattern of tissue necrosis from the liver after the liver has been dissected to expose the focal plane of the dual-frequency system. The geometry of the pattern of responses at the difference frequency correlates reasonably well with the actual pattern of tissue necrosis as indicated by the photograph.

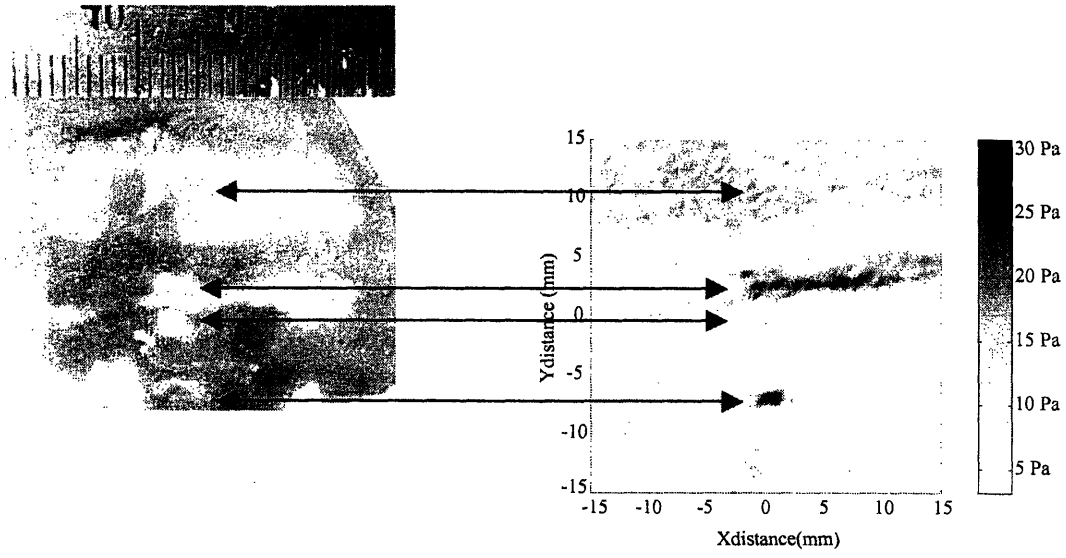


**Figure 5-3:** Experimentally measured difference frequency generated during a scan of thermal lesions created in fresh *ex vivo* rabbit liver. A photograph of the necrosis pattern is displayed (left) next to the image formed by plotting the difference frequency response as a function of position (right).

## 5.2 Theory

The second-order nonlinear wave equation discussed in chapter 2 has been solved by several researchers for canonical sources in a variety of coordinate systems. In particular, the solutions for planar, cylindrical, and spherical waves have been derived in the literature.[52,62,114] We employ the spherical wave solution to the second-order nonlinear wave equation in this chapter to

estimate the difference frequency field produced by linearly scattered waves from a pressure release sphere and a small air-bubble. Dean addressed the topic of spherical sources of nonlinear wave interaction in his 1962 paper.[52] Given spherical waves $P_a$ and $P_b$ radiating at frequencies $\omega_a$ and $\omega_b$ from the same source point, the difference frequency field $P_-(r)$ at radial distance $r$ from the source point is given by Dean[52],

$$P_-(r) = \mathrm{Re}\frac{1-\Gamma}{\rho_0 c_0^2} k_- P_a P_b \cdot e^{j(k_- r - \omega_- t)} \cdot \frac{1}{r}\left[\ln\frac{r}{a} - e^{-j\phi(r)}\right]$$
$$\text{where } \phi(r) = 2k_- r\int_a^r \frac{e^{2jk_- r}}{r} dr \tag{0.65}$$

for a small radiating sphere of diameter $a$, with difference frequency wave number $k_- = \frac{|\omega_a - \omega_b|}{c}$, and ambient density and speed of sound $\rho_0$ and $c_0$ respectively.[52]

In this chapter, the target is not considered a source, rather it acts to scatter the primary fields, which then interact with one another nonlinearly. For air bubbles and pressure release spheres that are small ($ka \ll 1$) relative to the scattered wavelength (in this case, the wavelength of the high frequency primary field), the approximation of spherical spreading is valid even relatively close to the target. This fact was demonstrated by Jones in experiments involving scattering from 35 μm air bubbles[137]. Therefore, we consider the spherical pressure wave resulting from the linear scattering of each focused beam. Then, we employ equation (0.65) to solve for the difference frequency field generated by the interaction of the resulting spherically spreading waves at the two primary frequencies.

First, we consider the linear scattering problem separately for each focused field incident on the target (see Figure 5-4). The incident field from each focused transducer, $P_{ai}(x,y,z)$ and $P_{bi}(x,y,z)$, is decomposed into the local plane wave spectrum using the two-dimensional Fourier transform evaluated at the plane intersecting the center of the target $z_0$,

$$P_{ai}(k_{ax},k_{ay};z_0) = \int_{-\infty}^{\infty}\int_{-\infty}^{\infty} P_{ai}(x,y,z_0)e^{-j(k_{ax}x+k_{ay}y)}dxdy$$
$$P_{bi}(k_{bx},k_{by};z_0) = \int_{-\infty}^{\infty}\int_{-\infty}^{\infty} P_{bi}(x,y,z_0)e^{-j(k_{bx}x+k_{by}y)}dxdy \tag{0.66}$$

Next, we scatter each plane wave component individually from the center of the small scatterer out to the radius of the scatterer at $r = a$ by substituting the expression for the incident plane wave

components given by equation (0.66) into the approximation for plane wave scattering from an omni-directional scatterer given by equation (0.52). The result of this substitution is the expression,

$$\begin{aligned}\tilde{P}_{as}(r) &\approx P_{ai}(\mathbf{k}_{ai};z_0)\cdot\frac{S(k_{ai})}{k_a r}e^{j(k_a r)}\\ \tilde{P}_{bs}(r) &\approx P_{bi}(\mathbf{k}_{bi};z_0)\cdot\frac{S(k_{bi})}{k_b r}e^{j(k_b r)}\end{aligned} \tag{0.67}$$

where $S(k_{ai})$ is the appropriate scatter function for the object considered given an incident wave number $k_{ai}=k_a=\frac{\omega_a}{c}$ corresponding to frequency $\omega_a$ (likewise for frequency $\omega_b$). We use a scatter function, $S(k_{ai})$, which is independent of the incident and outgoing wave vector directions for the two omni-directional cases we consider in this chapter. To obtain the total spherical pressure wave, $P_a(r=a)$ and $P_b(r=a)$, scattered to the surface of the target ($r=a$) from each focused transducer, we take the inverse Fourier transform over all wave numbers for each focused beam,

$$\begin{aligned}P_a(r=a) &= \frac{1}{(2\pi)^2}\int_{-\infty}^{\infty}\int_{-\infty}^{\infty}P_{ai}(\mathbf{k}_{ai};z_0)\cdot\frac{S(k_{ai})}{k_a a}e^{j(k_a a)}e^{j(k_{ax}x+k_{ay}y)}dk_{ax}dk_{ay}\\ P_b(r=a) &= \frac{1}{(2\pi)^2}\int_{-\infty}^{\infty}\int_{-\infty}^{\infty}P_{bi}(\mathbf{k}_{bi};z_0)\cdot\frac{S(k_{bi})}{k_b a}e^{j(k_b a)}e^{j(k_{bx}x+k_{by}y)}dk_{bx}dk_{by}\end{aligned} \tag{0.68}$$

Finally, we substitute the solution for the spherical waves originating at $r=a$ and at frequencies $\omega_a$ and $\omega_b$ given by equation (0.68) into Dean's solution for the generation of difference frequency pressure from spherical waves (0.65). The final expression for the difference frequency field generated from the nonlinear interaction of scattered waves from two focused transducers sonicating a small spherical target is given by,

$$\begin{aligned}&P_{-}(r)=\mathrm{Re}\frac{1-\Gamma}{\rho_0 c_0^2}k_{-}P_a(r=a)P_b(r=a)\cdot e^{j(k_{-}r-\omega_{-}t)}\cdot\frac{1}{r}\left[\ln\frac{r}{a}-e^{-j\phi(r)}\right]\\ &\text{where } \phi(r)=2k_{-}r\int_a^r\frac{e^{2jk_{-}r}}{r}dr\end{aligned} \tag{0.69}$$

given the difference frequency wavenumber $k_- = \frac{|\omega_a - \omega_b|}{c}$, the expressions for $P_a(r=a)$ and $P_a(r=a)$ in (0.68), and the particular scatter functions provided below for the two targets we consider.

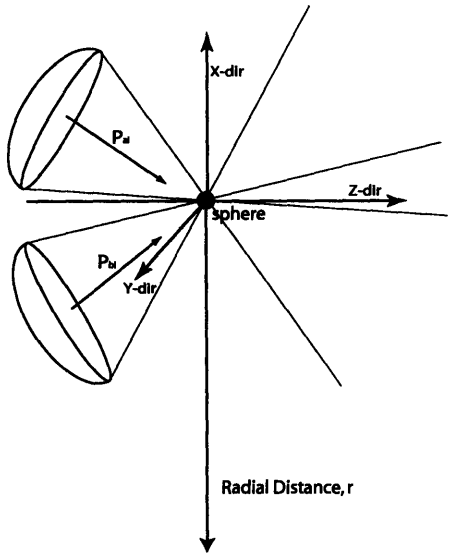


**Figure 5-4:** Diagram of scattering problem for two focused acoustic fields incident on a small spherical scatterer.

## *5.2.1 The Small Pressure Release and Gas Bubble Scatterer*

We consider the small pressure release and gas bubble scatterers because they lead to omni-directional scattered waves such that incident planar waves propagating at any angle will scatter in the form of spherically spreading waves (Figure 5-5). Therefore, these targets lead to relatively straightforward mathematical expressions for use in the model. Jones considered the sum frequency field generated using the more complicated scattering function of a rigid spherical scatterer, which is not omni-directional.[137] Makris *et al.* considered arbitrary scatterers but for non-collinear plane waves rather than focused beams.[94] For the pressure release sphere and gas bubble insonified by focused beams considered in this chapter, the scattered wave can be assumed to be spherically symmetric, provided $ka \ll 1$ and the receiver is in the far field of the target.

The scatter function for an air-filled bubble (0.70) and a pressure release sphere (0.71) are provided in section 4.1 and repeated here,

$$S = \frac{ka}{\frac{(3\gamma P_0/\rho)}{(2\pi a f)^2} - 1 - ika} \tag{0.70}$$

$$S = ka \tag{0.71}$$

where $\gamma = 1.4$ is the ratio of specific heats for air, $\rho = 1000\ \text{kg}/m^3$ is the water density, $P_0 = 100$ kPa is the ambient pressure, $f$ is the frequency of the primary field, $k = \frac{2\pi}{\lambda}$ is the wave number, and $a$ is the bubble radius in meters. In this chapter, we note that the omni-directional scatter functions used do not depend on the incident wave vector $\mathbf{k}_i$ or the outward wave vector $\mathbf{k}_o$.

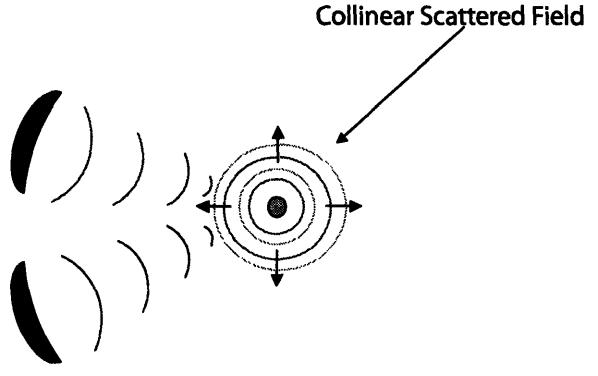


**Figure 5-5:** Diagram of the collinear interaction of two spherically scattered fields.

## 5.3 Numerical Implementation of Theory

The simulation was written in the Matlab® programming environment to estimate the difference frequency pressure at a distance $r$ from the center of the scatterer using equations (0.68) and (0.69) together with the scatter functions of (0.70) and (0.71). We model each transducer as having a diameter of 4 cm and a focal distance of 10 cm, operating at $2.74MHz \pm 25kHz$ and driven at 10 W electrical power. This power resulted in a peak pressure at the focus of 2.1 MPa for each primary field. The resulting difference frequency field radiating from the object is calculated as a function of radial distance from the scatterer (see Figure 5-4). We computed the difference frequency pressure after scattering from spherical targets of varying diameter to determine the relationship between object size and the generation of difference frequency sound.

The results of the simulation for a 20 μm spherical scatterer are plotted in Figure 5-6.

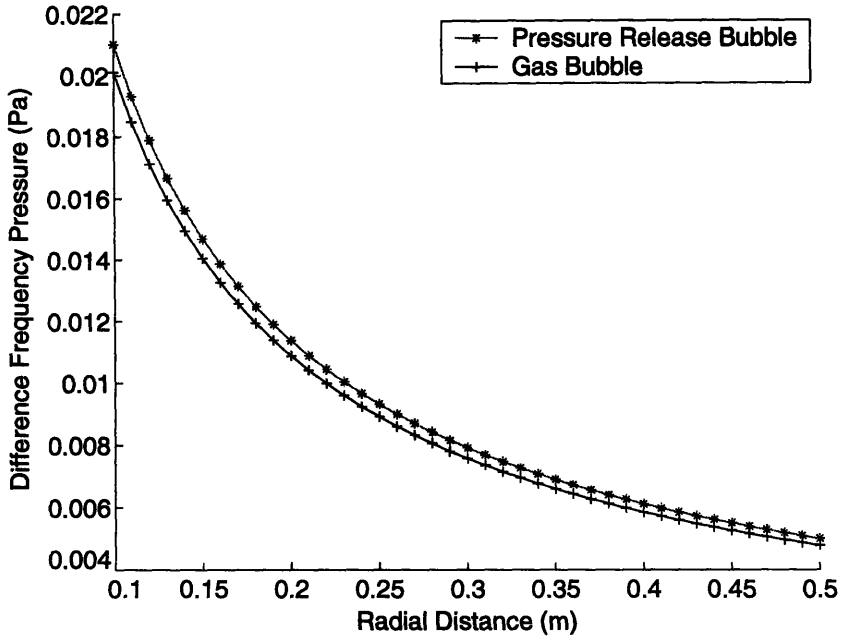


**Figure 5-6:** Simulation of the difference frequency field generated by the interference of linearly scattered primary frequency fields. In this simulation, the primary fields have been scattered from a pressure release spherical scatterer and an air-filled gas bubble with a radius of 20 μm. The primary fields incident on the scatterers are driven at a frequency of $2.74MHz \pm 25kHz$ and at 10W electrical power to obtain a peak pressure at the focus of 2.1 MPa for each primary field.

The result of the simulation demonstrates several important features of the nonlinear interaction of scattered waves. First, the result indicates a decay of the difference frequency field that falls off as $\frac{\ln r}{r}$ as the distance $r$ from the scatterer to the receiver increases. This decay rate is smaller than the $\frac{1}{r}$ decay rate of the primary scattered field. The reduced decay rate contributes to the appreciable propagation of the difference frequency field even as the primary field diverges. The simulation also reveals the relative importance of the two types of scatterers for producing a difference frequency field. For the parameters simulated, the difference frequency produced after scattering from the pressure release bubble is only slightly greater than that produced after scattering from the air-bubble.

The primary difference between the linear scattering of the primary waves which we calculate in this chapter and the linear scattering of the incident difference frequency field addressed in chapter 4 is that here, the primary field scatters at the primary wave-number $k_{a,b}$ rather than the difference frequency wave-number $k_-$, which is much smaller. The larger wave number used here for scattering of the primaries and the larger incident pressure achieved by the primary fields, results in much larger amplitudes for the calculated difference frequency levels in this case compared with the results of simulations as plotted in Figure 4-10.

Bubble resonance in the case of the air-filled bubble is an additional important consideration. The resonant frequency of the bubble is given by[131],

$$f_{resonant} = \frac{\sqrt{3\gamma P_0 / \rho}}{2\pi a} \text{ Hz} \tag{0.72}$$

where $\gamma$ is the ratio of specific heats the gas (in this case $\gamma = 1.4$ for air), $\rho = 1000 \text{ kg}/m^3$ is the water density, $P_0 = 100$ kPa is the ambient pressure, and $a$ is the bubble radius in meters. The resonance relationship for an air bubble in water is shown in Figure 5-7.

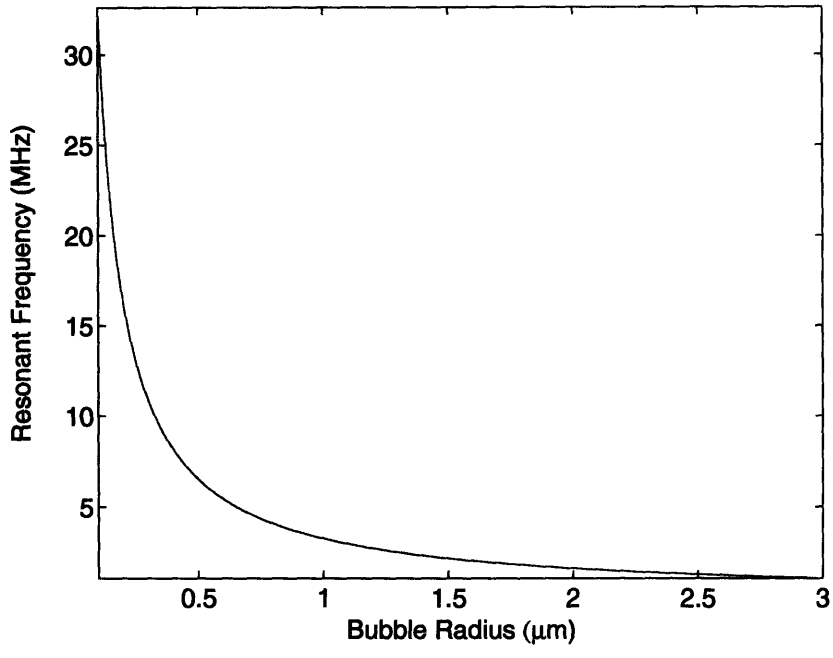


**Figure 5-7:** Calculated resonance curve for an air-filled bubble plotted as a function of bubble radius.

This resonance curve demonstrates that for the range of primary frequencies used in this thesis (1-3 MHz), the resonant bubble radius is less than 3 μm in size. In particular, at a primary frequency of 2.7 MHz, the resonant bubble radius is approximately 1.2 μm. It is well-known that at resonance, the ratio of the scattering cross-section to the geometric cross-section reaches a peak, indicating the greatly increased efficiency of scattering for a resonant bubble compared to a bubble off-resonance.[131] Figure 5-8 shows the resulting generation of difference frequency sound for a single resonant air bubble.

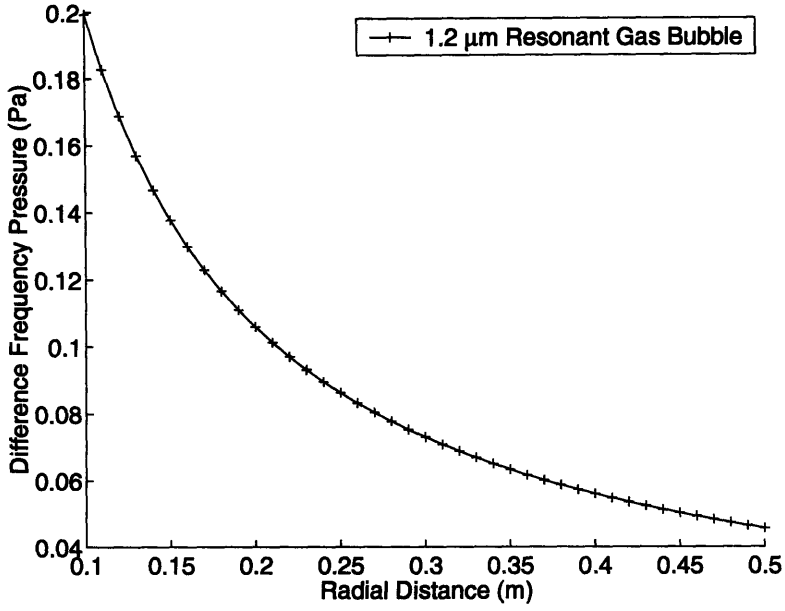


**Figure 5-8:** Simulation of the difference frequency generated by the nonlinear interaction of waves which are first linearly scattered from a single resonant gas bubble.

The difference frequency sound level is at .2 Pa for a single resonant gas bubble. This difference frequency sound generation is approximately 4 times greater than for the 20 μm target, despite the fact that the bubble is almost 17 times smaller in this case. The increased difference frequency response in spite of the great reduction in the size of the scatterer can be attributed to the enormous gain from bubble resonance. A more involved study, which is beyond the scope of this thesis, is required to analyze clouds of bubble scatterers.

## 5.4 Conclusions

In this chapter, we presented images made of rabbit liver after the formation of lesions with high-powered ultrasound (40 W electrical, 8 MPa peak pressure). The results suggest that bubble scattering, particularly due to cavitation events, may lead to signals on the order of 5-30 Pa at the difference frequency. For the theoretical section of this chapter, we employed an approach following the difference frequency work Makris *et al.*, which is similar to that of Jones, Bellin and Beyer in their studies of the generation of sum frequency sound fields[58,94,137]. Our theoretical model of the nonlinear interaction of linearly scattered waves from a single bubble or pressure release sphere illustrated that a measurable difference frequency signal may be generated even from a single bubble. In particular, as illustrated in Figure 5-8, the nonlinear generation of the difference

frequency sound was greatest for bubbles of resonant size (1.2 μm in this case) due to the increased efficiency of linear scattering at the resonant size.

Because the two experiments presented in this chapter were conducted in fresh tissue, several factors must be considered to fully understand the nature of the difference frequency response. These include the nonlinear parameter of the tissue and the gas bubble content of the sample. Further, it is possible that the bubble response is due to the reflection of the incident difference frequency field from a bubble as examined in chapter 4 or due to a large reflected signal from the bubble creating a parametric effect as described in chapter 3. However, for the case of reflection of the incident difference frequency field from a bubble, we would expect the difference frequency signal generated to be much smaller than the nonlinear interaction of scattered waves considered here as illustrated by the results plotted in Figure 4-10. The theoretical and experimental results for the linear scattering effect considered in this chapter suggest that a single bubble or bubble clouds may create a measurable signal for imaging tissue necrosis where cavitation has occurred.

This effect may lead to a potential imaging application of the nonlinear interference of linearly scattered waves with advantages over traditional echo ultrasound imaging technology. While traditional echo ultrasound systems can also detect small scatterers at a resolution approaching the primary frequency wavelength, these systems suffer from attenuation of the scattered signal as it returns to the receiver. This signal attenuation is due to the relatively high acoustical attenuation of the primary field wave as well as a $\frac{1}{r}$ divergence of the scattered field from each scatterer present. In addition, the scattered primary waves in traditional echo ultrasound systems will suffer from multiple scattering from other scatterers in the tissue as the return signal travels out to the receiver. All of these effects on the high frequency scattered signal will tend to reduce the signal to noise ratio in traditional echo ultrasound systems.

In contrast, the difference frequency response produced from the interaction of the scattered primary frequencies will not suffer from the large acoustical attenuation like the primary waveforms and will not decay at $\frac{1}{r}$, instead decaying at $\frac{\ln r}{r}$. In addition, the difference frequency signal will suffer less from multiple scattering off of small scatterers encountered in the return path than the primary signal because the difference frequency wavelength is often much larger than the typical scatterers in tissue. For these reasons, a difference frequency imaging system utilizing the scattering of primary fields to produce a difference frequency response may produce images with the resolution of traditional ultrasound echo systems. Such a system may also achieve better signal to noise ratios. The use of contrast agents containing micro-bubbles for imaging with a dual-frequency system has been explored by Belohlavek[4] and is most likely a fruitful area for future investigation.

# 6 Conclusion

This thesis addresses three mechanisms for the generation of difference frequency sound from a dual frequency imaging system, in an effort to further explain and understand the physics underlying the imaging results previously reported in the literature using similar systems. Previously reported experimental work shows correlations between difference frequency signal generation with a dual-frequency imaging system and biological tissue parameters, including temperature, necrosis, and pathology (in the case of calcifications)[24,26,28,29,122,138]. However, to date, the literature has not undertaken a comparison of the relative significance of 1) the parametric effect, 2) linear reflection of the local difference frequency field, and 3) nonlinear interaction of linearly scattered waves. This thesis explores these three mechanisms and compares the relative magnitude of these effects to one another.

## 6.1 Summary of Theoretical and Experimental Findings

In Figure 6-1, we plot in broad fashion the relative orders of magnitude of the difference frequency sound generated by the mechanisms studied in this thesis. The diagram illustrates the range of responses for the three effects relative to the amplitude of the system noise. Although the powers varied from experiment to experiment, the overall difference in magnitude of each effect is greater than can explained by these relatively small variations in powers.

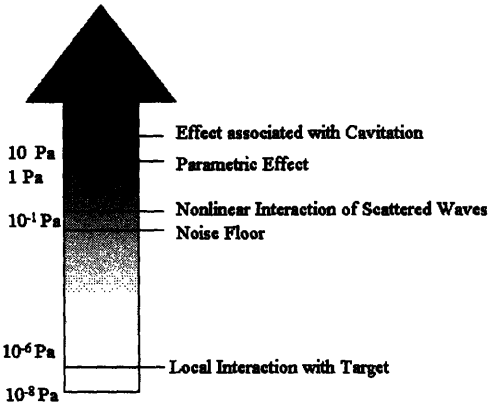


**Figure 6-1:** Diagram summarizing the results of the thesis in broad fashion. The diagram shows the pressure amplitude of difference frequency sound generated by the various effects considered, illustrating the relative magnitude of each.

Chapter 3 explored the parametric effect for generating difference frequency sound. In chapter 3, we first explained the parametric array and formulated an approximate solution for the propagating difference frequency field. This approximate solution correlated reasonably well with the Green's Function volume integral solution to the wave equation, as well as with experimental measurements of the difference frequency field. In chapter 3, we then described a model to simulate the parametric generation of difference frequency sound in the dual-frequency system. Levels predicted by the model correlated reasonably well with experimental measurements. The results of this chapter suggested that the parametric effect is most likely the source of difference frequency sound generation where there are planar boundaries with large dimensions compared to the focal diameter of the primary field, and where the planar boundaries are positioned specularly to the two ultrasound sources.

Chapter 4 addressed the local interaction of two pressure fields on a target. The results of experiments in chapter 4 demonstrated an appreciable displacement and force at the difference frequency when the interface of a target was positioned in the focus of the primary fields. However, the simulation of the incident difference frequency waves, using the volume integral/Green's Function method for solving the second order wave equation in free space, predicted immeasurable scattered waves. Careful experiments confirmed that difference frequency sound is undetected above the system noise if this effect is isolated from the other two effects.

Chapter 5 examined the nonlinear interaction of scattered waves from small targets. In chapter 5, we first reported the results of two *ex vivo* tissue experiments in which cavitation was

observed, to suggest the importance of air-bubbles produced during cavitation in generating difference frequency sound. We then formulated a mathematical expression for the difference frequency field produced from the nonlinear interaction of acoustic waves originating from focused beams which have been linearly scattered from a single pressure release sphere or air-bubble. Finally, we simulated the levels for the difference frequency sound generated by a single scatterer. The simulation results indicated that the nonlinear interaction of linearly scattered waves may produce a small but measurable signal from even one small scatterer, especially if the scatterer is of the resonant diameter.

## 6.2 Application of Findings

The results of simulations and experiments illustrate the relative importance of the three considered mechanisms for the generation of difference frequency sound. The thesis compared the previously described parametric effect to the nonlinear interaction of scattered waves and the scattering of an incident difference frequency field for the first time in the context of the dual-frequency imaging system[52,58,77,102]. We conclude that the former two effects appear to be more significant sources of difference frequency sound generation than the scattering of incident difference frequency waves from a target.

This suggests the possibility of new modes of imaging with a dual frequency system that rely upon the nonlinear interaction of scattered waves and the large response from sites of cavitation. The resulting imaging modalities may include standard ultrasound echo imaging with increased signal-to-noise ratio resulting from the nonlinear interaction of scattered waves, tissue perfusion imaging by means of injectable contrast agents containing micro-bubbles, or monitoring thermal surgery by first creating a localized nucleus of cavitation and then using the magnitude of the response from the bubbles generated to correlate with the degree cavitation and subsequent thermal ablation at the site. Even molecular trafficking by means of tagged contrast agents may be possible with the nonlinear interaction of scattered waves. As an alternate to difference frequency imaging, the effect of local displacement, as measured by means of a pulsed echo ultrasound device or a laser vibrometry device, may be useful for imaging the mechanical response of tissues in a method similar to that employed in the growing field of elastography imaging.

The dual-frequency imaging system may have promising applications for imaging modalities in the medical and/or biological fields. As with most research, the questions raised as a result of this work greatly outnumber the questions answered. In order to utilize USVA as a successful imaging tool, one must take measures to avoid the signal from the parametric effect, which can be considered an imaging artifact. Additionally, it may be possible to use nonlinear

scattering to form images that rely on the presence of small scatterers; a technique that may be enhanced with the use of *in vivo* contrast agents containing small scattering micro-bubbles.

# Appendix A

## Co-axial Transducer

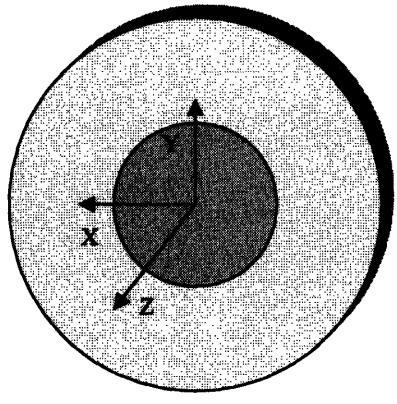


**Figure A-1:** Diagram of the inner/outer elements of a concentric element array.

*Efficiencies*

### *Inner Ring Element*

| Electric Input (VPP) | Average Electric Power (W) | Average Acoustic Power (W) | Standard Error of Measurement | Efficiency (%) |
|---|---|---|---|---|
| 0.03 | 2.49E-01 | 1.96E-01 | 2.63E-03 | 78.84 |
| 0.05 | 6.88E-01 | 5.51E-01 | 3.46E-03 | 80.07 |
| 0.07 | 1.34E+00 | 1.07E+00 | 2.88E-03 | 79.97 |
| 0.09 | 2.18E+00 | 1.74E+00 | 2.36E-03 | 79.94 |
| 0.11 | 3.25E+00 | 2.61E+00 | 1.03E-02 | 80.17 |
| 0.13 | 4.56E+00 | 3.66E+00 | 1.21E-02 | 80.25 |
| 0.15 | 6.06E+00 | 4.84E+00 | 1.33E-02 | 79.95 |
| 0.17 | 7.80E+00 | 6.25E+00 | 1.45E-02 | 80.13 |
| 0.19 | 9.74E+00 | 7.80E+00 | 1.99E-02 | 80.03 |
| 0.21 | 1.19E+01 | 9.55E+00 | 3.95E-02 | 80.12 |
| 0.23 | 1.43E+01 | 1.14E+01 | 2.31E-02 | 79.93 |
| 0.25 | 1.69E+01 | 1.35E+01 | 7.82E-03 | 80.04 |
| 0.27 | 1.97E+01 | 1.58E+01 | 8.27E-03 | 80.03 |
| 0.29 | 2.28E+01 | 1.82E+01 | 2.99E-02 | 79.68 |

**Table A-0-1:** Efficiencies at various powers for inner element of co-axial array.

*Outer Ring Element*

| Electric Input (VPP) | Average Electric Power (W) | Average Acoustic Power (W) | Standard Error of Measurement | Efficiency (%) |
|---|---|---|---|---|
| 0.03 | 2.41E-01 | 1.58E-01 | 8.78E-03 | 65.7 |
| 0.05 | 6.63E-01 | 4.21E-01 | 3.25E-03 | 63.41 |
| 0.07 | 1.30E+00 | 8.28E-01 | 1.24E-03 | 63.91 |
| 0.09 | 2.13E+00 | 1.37E+00 | 4.19E-03 | 64.15 |
| 0.11 | 3.18E+00 | 2.06E+00 | 1.86E-03 | 64.63 |
| 0.13 | 4.44E+00 | 2.86E+00 | 8.80E-03 | 64.46 |
| 0.15 | 5.90E+00 | 3.77E+00 | 3.13E-02 | 63.92 |
| 0.17 | 7.59E+00 | 4.90E+00 | 2.11E-02 | 64.56 |
| 0.19 | 9.50E+00 | 6.16E+00 | 1.26E-02 | 64.79 |
| 0.21 | 1.16E+01 | 7.48E+00 | 1.46E-02 | 64.34 |
| 0.23 | 1.39E+01 | 8.97E+00 | 3.98E-02 | 64.49 |
| 0.25 | 1.65E+01 | 1.06E+01 | 7.31E-03 | 64.48 |
| 0.27 | 1.92E+01 | 1.24E+01 | 1.93E-02 | 64.61 |
| 0.29 | 2.22E+01 | 1.43E+01 | 1.72E-02 | 64.42 |

**Table A-0-2:** Efficiencies at various powers for outer element of co-axial array.

*Pressure Fields*

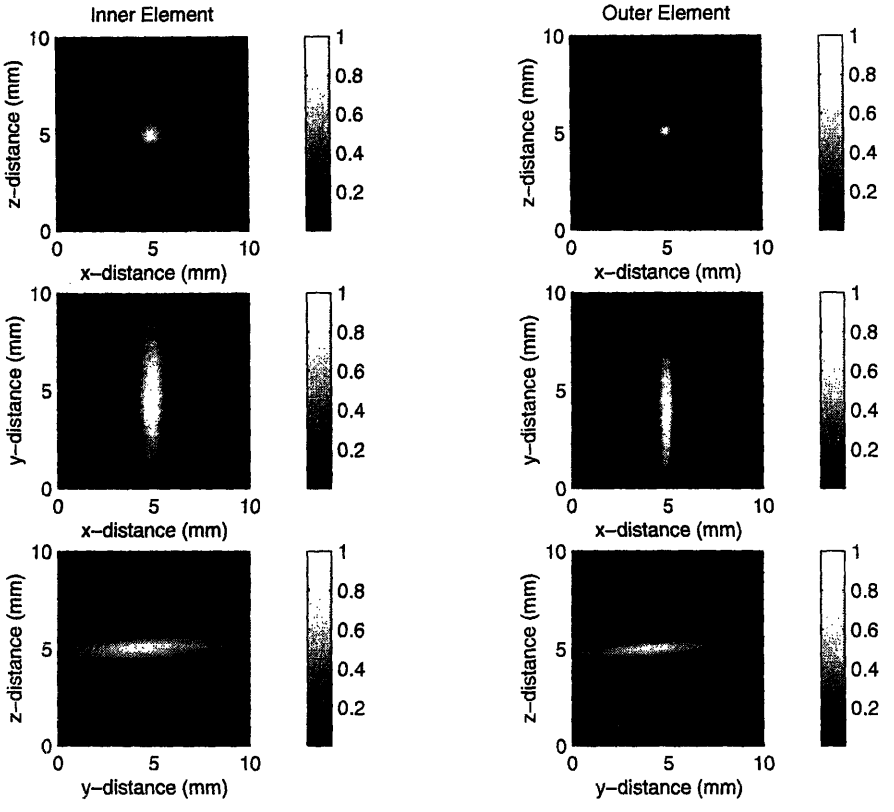


**Figure A-2:** Simulation of the normalized pressure fields of the inner element (left column) and outer element (right column) of a concentric element array. The figure shows the simulation results plotted in the XZ, XY, and YZ planes through the focus.

# Appendix B

*Spatial Nyquist Limit*

Similar to the frequency Nyquist limit, in spatial transforms, there is a maximum spatial frequency that can be resolved given a certain sample rate in the spatial domain. This Nyquist limit is determined by ½ the spatial sample rate. So, suppose we have a spatial sample rate d = x pts/meter. Then, the limit for the maximum spatial frequency which can be resolved, $k_{lim}/2\pi$ is d/2:

$$d = \frac{\#pts}{distance}$$

$$\frac{k_{lim}}{2\pi} = \frac{d}{2} = \frac{\#pts}{2 \cdot distance}$$

$$k_{lim} = \frac{\#pts \cdot \pi}{distance}$$

Note: we must divide k by $2\pi$ since the Nyquist limit applies to frequency and k is the equivalent of "angular frequency" ($\omega$ in the time domain).

In our simulations, we want to allow K to span the range of all possible propagating directions given the wavelength $\lambda$ of the incident wave. Therefore $K = \pm\frac{2\pi}{\lambda}$. In this case, there must be enough points in space such that $k_{lim} = K$. If $k_{lim} < K$, then there will be aliasing in space when the inverse transform is performed. In order to prevent aliasing, we may increase the number of points artificially by zero padding the spatial field with 0's outside of the region analyzed. This is equivalent to simply adding more points in the discretization of the vector $K$ since the number of points in the $K$ vector is assumed to be the same as the number in the spatial domain. So, in order to force $k_{lim}$ to equal $K$, we require that:

$$K = \frac{\#pts \cdot \pi}{distance}$$

from which we can determine either the number of points to specify in the K-vector for a given distance spanned in space or the maximum distance in space that can be spanned without aliasing given a set number of points for the K-vector.

# Appendix C

*Relationship Between Mechanical and Acoustical Parameters*

The acoustical parameters of sound speed and density can be related to the mechanical properties of bulk modulus and Young's modulus as illustrated in the exercise that follows. This exercise was reviewed in the notes of the MIT acoustics course number 13.851.[78]

For an isotropic material, the bulk modulus $\beta$ (also known as the modulus of compression) is a measure of the resistance to a change in volume when the material is subjected to a hydrostatic load. In this way, it can be understood as a three-dimensional Hooke's Law relationship whereby the stiffness of the material is characterized by the bulk modulus and the compressibility of the material is defined as $\mathrm{K} = \frac{1}{\beta}$. Specifically, the bulk modulus is defined as the ratio of the pressure change required to cause a given volume strain,

$$dP = -\beta \frac{dV}{V} \tag{0.73}$$

where $V$ is the volume of the material and $P$ is the pressure on the material.

If we consider a material constrained in its cross-sectional area $A$ then the volume $V = A \cdot l$ where $l$ is the length of the container. Further, if the material is compressed along the dimension of $l$, then the volume strain $\frac{dV}{V}$ can be expressed as $\nabla l$. In addition, the differential $dP$ can be expressed to first order as $P - P_0 \simeq P_1$. The result of these two expressions can be applied to equation (0.73) to give the result,

$$P_1 \simeq -\beta \nabla \cdot l \tag{0.74}$$

Now, the substitution for the first order pressure term in equation (0.74) can be made using the equation of state $P_1 = \rho_1 c^2$ (where $\rho_1$ is the first order density of the material and $c$ is the speed of sound in the material). The result is,

$$\rho_1 c^2 \simeq -\beta \nabla \cdot l$$

Taking the derivative in time of both sides gives,

$$c^2 \frac{\partial \rho_1}{\partial t} \simeq -\beta \nabla \cdot \frac{\partial l}{\partial t} = -\beta \nabla \cdot \mathbf{V} \tag{0.75}$$

Finally, using the conservation of mass equation $\frac{\partial \rho_1}{\partial t} = -\rho_0 \nabla \cdot \mathbf{V}$ in equation (0.75) (where $\rho_0$ is the resting density of the material and $\mathbf{V}$ is the velocity of compression in the $l$ direction), the equation becomes,

$$\beta = c^2 \rho_0$$

The final result relates the bulk modulus of the material to the speed of sound and density at rest. This relationship can be written as,

$$c = \sqrt{\frac{\beta}{\rho_0}} \tag{0.76}$$

The result illustrates the interconnection between mechanical and acoustical properties of materials, which can be expected since acoustical waves are simply mechanical compressions of the medium in which they travel. For fluids, the bulk modulus completely describes the material stress-strain relationship. However, elastic solids are more complex because the axial strain ($\varepsilon_{xx}$) and lateral strain ($\varepsilon_{yy}$) are coupled by the Poisson's ratio $\nu = -\frac{\varepsilon_{yy}}{\varepsilon_{xx}}$. This implies that the axial stress-strain relationship may not be the same as the three-dimensional stress-strain relationship characterized by the bulk modulus. The axial stress/strain relationship is characterized by the Young's Modulus, E, where the Young's Modulus is related to the Bulk Modulus through the Poisson's ratio by[139],

$$\beta = \frac{\mathrm{E}}{3(1-2\nu)} \tag{0.77}$$

This fundamental difference between fluids and elastic solids raises an important exception to the general rule that the mechanical properties are equivalently expressed by the acoustical

properties of a material. In the case where the Poison's ratio $\nu$ is difference for two different materials, they may have very different Young's modulus, $E$, but still have the same bulk modulus, $\beta$. Therefore, these two materials may have the same volumetric response to an imposed pressure and hence the same acoustical properties $\rho$ and $c$ as defined in equation(0.76). The identical acoustical properties but difference in mechanical properties of the Young's modulus is possible if the Poisson's ratio is such that the two materials have the same bulk modulus. This occurs for example with the silicone gels used in this thesis whereby the cross-linkage of proteins can be altered by the mix ratio of the gel parts A and B. In this example, the young's modulus is changed dramatically although the measured density and speed of sound remains the same as measured in preliminary experiments in preparation for this thesis (Table 1-2).

Reference List


1. Fatemi,M. & Greenleaf,J.F. Ultrasound-stimulated vibro-acoustic spectrography. *Science* **280**, 82-85 (1998).

2. Thierman,J., McDannold,N., Konofagou,E. & Hynynen,K. New Directions in US and MRI thermal monitoring. Proc.of the 48th Meeting of the RRS/19th Meeting of the NAHS, San Juan, Puerto Rico, 76. 2001.

3. Thierman J. Ultrasound Stimulated Acoustic Emission for Monitoring Thermal Surgery. Massachusetts Institute of Technology. Master's Thesis . 2001. Cambridge, MA.

4. Belohlavek,M., Asanuma,T., Kinnick,R.R. & Greenleaf,J.F. Vibro-acoustography: quantification of flow with highly-localized low-frequency acoustic force. *Ultrason. Imaging* **23**, 249-256 (2001).

5. Fry,F.J. & Johnson,L.K. Tumor irradiation with intense ultrasound. *Ultrasound. Med. Biol.* **4**, 337-341 (1978).

6. Lele,P.P. Induction of deep, local hyperthermia by ultrasound and electromagnetic fields: problems and choices. *Radiat. Environ. Biophys.* **17**, 205-217 (1980).

7. Cain,C.A. & Umemura,S. Annular and sector phased array applicators for ultrasound hyperthermia. Proceedings of the Ultrasonics Symposium , 936. 1985.

8. Lee,C.S. & Frizzell,L.A. Exposure levels for ultrasonic cavitation in the mouse neonate. *Ultrasound. Med. Biol.* **14**, 735-742 (1988).

9. Gee,W., Lee,S.W., Mittra,R., Cain,C.A. & Magin,R. Focused array hyperthermia applicator: theory and experiment. *1983 International Symposium Digest, Antennas and Propagation* 261 (1983).

10. Diederich,C.J. & Hynynen,K. Induction of hyperthermia using an intracavitary ultrasonic applicator. Proceedings of the Ultrasonics Symposium , 871. 1987.

11. Diederich,C.J., Duponchelle,I.M., Buchanan,M.T. & Hynynen,K. Evaluation of intracavitary ultrasound arrays for hyperthermia. Proceedings of the Ultrasonics Symposium , 1657. 1990.

12. Hynynen,K., Watmough,D.J. & Mallard,J.R. Design of ultrasonic transducers for local hyperthermia. *Ultrasound. Med. Biol.* **7**, 397-402 (1981).

13. Damianou,C. & Hynynen,K. Focal spacing and near-field heating during pulsed high temperature ultrasound therapy. *Ultrasound. Med. Biol.* **19**, 777-787 (1993).

14. Hynynen,K. *et al.* On-line MRI monitored noninvasive ultrasound surgery. Proceedings of the 14th annual EMB Society Meeting , 350-351. 1992.

15. Darkazanli,A., Hynynen,K., Unger,E.C. & Schenck,J.F. On-line monitoring of ultrasonic surgery with MR imaging. *J. Magn. Reson. Imaging* **3**, 509-514 (1993).

16. Hynynen,K. *et al.* A clinical, noninvasive, MR imaging-monitored ultrasound surgery method. *Radiographics* **16**, 185-195 (1996).

17. McDannold,N.J., Hynynen,K., Wolf,D., Wolf,G. & Jolesz,F.A. MRI evaluation of thermal ablation of tumors with focused ultrasound. *J. Magn. Reson. Imaging* **8**, 91-100 (1998).

18. Jolesz,F.A. *et al.* MR imaging of laser-tissue interactions. *Radiology* **168**, 249-253 (1988).

19. McDannold,N.J., Jolesz,F.A. & Hynynen,K. The use of MRI in vivo to monitor thermal build-up druing focused ultrasound surgery. Proceedings of the Sixth Meeting of the International Society for Magnetic Resonance in Medicine.Sydney, Australia . 1998.

20. Seip,R., Ebbini,E.S., O'Donnell,M. & Cain,C.A. Non-invasive detection of thermal effects due to highly focused ultrasonic fields. Proceedings of the Ultrasonics Symposium , 1229. 1993.

21. Ebbini,E.S., Ibbini,M.S. & Cain,C.A. An inverse method for hyperthermia phased-array pattern synthesis. Proceedings of the Ultrasonics Symposium , 947. 1988.

22. Jenne,J. *et al.* Temperature mapping for high energy US-therapy. Proceedings of the Ultrasonics Symposium , 1879. 1994.

23. Jenne,J.W. *et al.* CT on-line monitoring of HIFU therapy. Proceedings of the Ultrasonics Symposium , 1377. 1997.

24. Fatemi,M. & Greenleaf,J.F. Ultrasound-stimulated vibro-acoustic spectrography. *Science* **280**, 82-85 (1998).

25. Fatemi,M. & Greenleaf,J.F. Application of radiation force in noncontact measurement of the elastic parameters. *Ultrason. Imaging* **21**, 147-154 (1999).

26. Konofagou,E., Thierman,J. & Hynynen,K. Ultrasound surgery monitoring using ultrasound-stimulated acoustic emission: simulations and experimental results. Proceedings of the Ultrasonics Symposium . 2000.

27. Konofagou,E., Thierman,J. & Hynynen,K. A focused ultrasound method for simultaneous diagnostic and therapeutic applications--a simulation study. *Phys. Med. Biol.* **46** , 2967-2984 (2001).

28. Konofagou,E.E., Thierman,J., Karjalainen,T. & Hynynen,K. The temperature dependence of ultrasound-stimulated acoustic emission. *Ultrasound Med. Biol.* **28**, 331-338 (2002).

29. Konofagou,E., Thierman,J. & Hynynen,K. The use of ultrasound-stimulated acoustic emission in the monitoring of modulus changes with temperature. *Ultrasonics* **41**, 337-345 (2003).

30. Fatemi,M., Wold,L.E., Alizad,A. & Greenleaf,J.F. Vibro-acoustic tissue mammography. *IEEE Trans. Med. Imaging* **21**, 1-8 (2002).

31. Fatemi,M. & Greenleaf,J.F. Probing the dynamics of tissue at low frequencies with the radiation force of ultrasound. *Phys. Med. Biol.* **45**, 1449-1464 (2000).

32. Morse,P.M. & Ingard,U. Theoretical Acoustics. 1968. Princeton, New Jersey, Princeton University Press.

33. Nightingale,K.R., Nightingale,R.W., Palmeri,M.L. & Trahey,G.E. A finite element model of remote palpation of breast lesions using radiation force: factors affecting tissue displacement. *Ultrason. Imaging* **22**, 35-54 (2000).

34. Nightingale,K.R., Palmeri,M.L., Nightingale,R.W. & Trahey,G.E. On the feasibility of remote palpation using acoustic radiation force. *J. Acoust. Soc. Am.* **110**, 625-634 (2001).

35. Sugimoto,T., Ueha,S. & Itoh,K. Tissue hardness measurement using the radiation force of focused ultrasound. 1377-1380. 1990. Honolulu, HI, USA, IEEE. IEEE 1990 Ultrasonics Symposium Proceedings.

36. Walker,W.F. *et al.* Imaging the stiffness of the vitreous body with acoustic radiation force. vol.2, 1635-1639. 1999. Caesars Tahoe, NV, USA, IEEE. 1999 IEEE Ultrasonics Symposium. Proceedings. International Symposium.

37. Lizzi,F.L. *et al.* Radiation-force technique to monitor lesions during ultrasonic therapy. *Ultrasound Med. Biol.* **29**, 1593-1605 (2003).

38. Krouskop,T.A., Younes,P.S., Srinivasan,S., Wheeler,T. & Ophir,J. Differences in the compressive stress-strain response of infiltrating ductal carcinomas with and without lobular features - implications for mammography and elastography. *Ultrasonic Imaging* **25**, 162-170 (2003).

39. Krouskop,T.A., Wheeler,T.M., Kallel,F., Garra,B.S. & Hall,T. Elastic moduli of breast and prostate tissues under compression. *Ultrasonic Imaging* **20**, 260-274 (1998).

40. Fatemi,M. & Greenleaf,J.F. Vibro-acoustography: An imaging modality based on ultrasound-stimulated acoustic emission. *Proc. Natl. Acad. Sci. U. S. A* **96**, 6603-6608 (1999).

41. Alizad,A. *et al.* Detection of calcium deposits on heart valve leaflets by vibro-acoustography: an in vitro study. *J. Am. Soc. Echocardiogr.* **15**, 1391-1395 (2002).

42. Calle,S., Remenieras,J.P., Bou,M.O. & Patat,F. Presence of nonlinear interference effects as a source of low frequency excitation force in vibro-acoustography. *Ultrasonics* **40**, 873-878 (2002).

43. Mitri,F.G., Trompette,P. & Chapelon,J.Y. Detection of object resonances by vibro-acoustography and numerical vibrational mode identification. *J. Acoust. Soc. Am.* **114**, 2648-2653 (2003).

44. Mitri,F.G., Trompette,P. & Chapelon,J.Y. Improving the Use of Vibro-Acoustography for Brachytherapy Metal Seed Imaging: A Feasibility Study. *IEEE Trans. Med. Imaging* **23**, 1-6 (2004).

45. Calle,S., Remenieras,J.P., Bou,M.O., Defontaine,M. & Patat,F. Application of nonlinear phenomena induced by focused ultrasound to bone imaging. *Ultrasound Med. Biol.* **29**, 465-472 (2003).

46. Ingard,U. & Pridmore-Brown,D.C. Scattering of sound by sound. *Acoustical Society of America -- Journal* **28**, 367-369 (1956).

47. Westervelt,P.J. Scattering of sound by sound. *Acoustical Society of America -- Journal* **29**, (1957).

48. Westervelt,P.J. Absorption of sound by sound. 112. 1972. Miami Beach, FL, USA, Acoust. Soc. America. Program of the 84th Meeting of the Acoustical Society of America. (Abstracts only).

49. Woodsum,H.C. & Westervelt,P.J. A general theory for the scattering of sound by sound. *Journal of Sound and Vibration* **76**, 179-186 (1981).

50. Westervelt,P.J. Recent advances in the theory of the nonscattering of sound by sound. 117-120. 1984. Kobe, Japan, Osaka Univ. Proceedings of the 10th International Symposium on Nonlinear Acoustics.

51. Jones,J.P. & Beyer,R.T. Scattering of sound by sound. *Journal of the Acoustical Society of America* **48**, 398-402 (1970).

52. Dean,I.I.I. Interactions between sound waves. *Acoustical Society of America -- Journal* **34**, 1039-1044 (1962).

53. Garrett,G.S., Tjotta,J.N. & Tjotta,S. Nearfield of a large acoustic transducer. II. Parametric radiation. *Journal of the Acoustical Society of America* **74**, 1013-1020 (1983).

54. Hamilton,M.F. Effects of noncollinear interaction on parametric acoustic arrays in dispersive fluids. *Journal of the Acoustical Society of America* **76**, 1493-1504 (1984).

55. Tjotta,J.N. & Tjotta,S. Nonlinear interaction of two collinear, spherically spreading sound beams. *J. Acoust. Soc. Am.* **67**, 484-490 (1980).

56. Roy,R.A. & Wu,J. An Experimental Investigation of the Interaction of Two Non-Collinear Beams of Sound. Proceedings of the 13th International Symposium on Nonlinear Acoustics . 1993. London, Elsevier Science Ltd.

57. Korman,M.S. & Beyer,R.T. The scattering of sound by turbulence in water. *Journal of the Acoustical Society of America* **67**, 1980-1987 (1980).

58. Bellin,J.L.S. & Beyer,R.T. Scattering of sound by sound. *Acoustical Society of America -- Journal* **32**, 339-341 (1960).

59. Kun,H.F., Zarembo,L.K. & Krasil'Nikov,V.A. Experimental investigation of mixing scattering of sound by sound in solids
Eksperimental'noe issledovanie kombinatsionnogo rasseyaniya zvuka na zvuke v tverdykh telakh. *Soviet Physics -- JETP* **21**, 1073-1077 (1965).

60. Berktay,H.O. & Al Temimi,C.A. Scattering of sound by sound. **50**, 181-187 (1971).

61. Rudenko,O.V. & Soluyan,S.I. Scattering of soud by sound. *Soviet Physics, Acoustics* **18**, 352-355 (1973).

62. Thuras,A.L., Jenkins,R.T. & O'Neil,H.T. Extraneous frequencies generated in air carrying intense sound waves. *Acoustical Society of America -- Journal* **6**, 173-180 (1935).

63. Ingard,U. & Pridmore-Brown,D.C. Scattering of sound by sound. *Acoustical Society of America -- Journal* **28**, 367-369 (1956).

64. Westervelt,P.J. Scattering of sound by sound. *Acoustical Society of America -- Journal* **29**, (1957).

65. Westervelt,P.J. Parametric acoustic array. *Acoustical Society of America -- Journal* **35**, 535-537 (1963).

66. TenCate,J.A. Scattering of Sound by Sound: Nonlinear Interaction of Collinear and Noncollinear Sound Beams. University of Texas at Austin. Doctoral Thesis. 1992.

67. Mujica,N., Wunenburger,R. & Fauve,S. Scattering of sound by sound in the vicinity of the liquid-vapor critical point. *Physical Review Letters* **90**, 234301 (2003).

68. Trivett,D.H. & Peter,H.R. Criticism of experiments on the scattering of sound by sound. *The Journal of the Acoustical Society of America* **96**, 3320 (1994).

69. Westervelt,P.J. Erratum. Nonscattering of sound by sound. Exact second-order transient solutions [J. Acoust. Soc. Am. 94, 1774 (A) (1993)]. *Journal of the Acoustical Society of America* **95**, 3669 (1994).

70. Roy,R.A., Madanshetty,S.I. & Apfel,R.E. An acoustic backscattering technique for the detection of transient cavitation produced by microsecond pulses of ultrasound. *J. Acoust. Soc. Am.* **87**, 2451-2458 (1990).

71. Westervelt,P.J. Recent advances in the theory of the nonscattering of sound by sound. 117-120. 1984. Kobe, Japan, Osaka Univ. Proceedings of the 10th International Symposium on Nonlinear Acoustics.

72. Korman,M.S. & Beyer,R.T. Scattering of sound by turbulence in water. *J. Acoust. Soc. Am.* **67**, 1980-1987 (1980).

73. Westervelt,P.J. Absorption of sound by sound. *Journal of the Acoustical Society of America* **59**, 760-764 (1976).

74. Westervelt,P.J. Scattering of sound by sound with applications. 111-118. 1974. Copenhagen, Denmark, IPC Sci & Technol. Press. Proceedings of the 1973 Symposium on Finite-Amplitude Wave Effects in Fluids.

75. Jones,J.P. & Beyer,R.T. Scattering of sound by sound. *J. Acoust. Soc. Am.* **48**, 398-402 (1970).

76. Beyer,R.T. Nonlinear Acoustics. Acoustical Society of America, New York (1997).

77. Beyer,R.T. & Jones,J.P. The interaction of sound with sound in water in the presence of a physical object. Vol IV, 629-632. 1971. Budapest, Hungary, Akademiai Kiado. Proceedings of the 7th international congress on acoustics.

78. Makris,N.C. & Dyer,I. MIT Course Notes, Course 13.851: Fundamentals and Applications of Underwater Sound. 2002.

79. Thierman,J.S., Makris,N.C., Ratilal,P. & Hynynen,K. Simulation and experiment of nonlinar scattering mechanisms producing difference frequencies from two distinct primary frequencies incident on a target. 113(4), 2324. 2003. 145th Meeting of the Acoustical Society of America. 5-2-2003.

80. Westervelt,P.J. Parametric acoustic array. *Acoustical Society of America -- Journal* **35**, 535-537 (1963).

81. Ottensmeyer,M.P. & Salisbury,J. In-vivo mechanical tissue property measurement for improved simulations. *Proc. SPIE. - Int. Soc. Opt. Eng. (USA)* **4037**, 286-293 (2000).

82. Bruyns,C. & Ottensmeyer,M.P. The development of a physically based virtual animal model using soft-tissue parameter testing. 239-243. 2002. Kaua'i, HI, USA, ACTA Press. Proceedings of the Fifth IASTED International Conference Computer Graphics and Imaging.

83. Simpson,R.E. Introductory Electronics for Scientists and Engineers. 341. 1987. New Jersey, Prentice Hall.

84. Wellman,P.S. Tactile Imaging. Harvard University. Doctoral Thesis . 1999.

85. Ottensmeyer,M.P. & Salisbury,J.K.Jr. In Vivo Data Acquisition Instrument For Solid Organ Mechanical Property
Measurement. Proceedings of the Medical Image Computing and Computer-AssistedIntervention 4th International Conference , 975-982. 10-17-2001. Utrecht, The Netherlands.

86. Ottensmeyer,M.P. Minimally Invasive Instrument for In Vivo Measurement of Solid Organ Mechanical Impedance. Massachusetts Institute of Technology. Doctoral Thesis . 2001.

87. Selfridge,A.R. Approximate material properties in isotropic materials. *IEEE Transactions on Sonics and Ultrasonics* **SU-32**, 381-394 (1985).

88. Hynynen,K. Methods of External Hyperthermic Heating. Gautherie,M. (ed.), pp. 61-115 (Springer-Verlag, New York,1990).

89. Chen,E.J., Novakofski,J., Jenkins,W.K. & O'Brien,W.D.J. Young's modulus measurements of soft tissues with application to elasticity imaging. *IEEE Transactions on Ultrasonics, Ferroelectrics, and Frequency Control* **43**, 191-194 (1996).

90. Samani,A., Bishop,J., Luginbuhl,C. & Plewes,D.B. Measuring the elastic modulus of ex vivo small tissue samples. *Phys. Med. Biol.* **48**, 2183-2198 (2003).

91. Yamada,N. Strength of Biological Materials. 1970. Baltimore, The Williams & Wilkins Company.

92. Lamb,H. The Dynamical Theory of Sound. Dover Publications, New York (1925).

93. Westervelt,P.J. Scattering of sound by sound. 301-305. 1990. Austin, TX, USA, Elsevier Applied Science. Frontiers of Nonlinear Acoustics. 12th ISNA.

94. Makris,N.C., Ratilal,P. & Thierman,J.S. Coherent nonlinear scattering mechanisms for ultrasound-stimulated vibro-acoustic spectrography. 112(5), 2405. 2002. 144th Meeting of the Acoustical Society of America. 12-2-2002.

95. Pierce,A.D. Acoustics: An Introduction to its Physical Principles and Applications. 427-428. 1989. Woodbury, NY, Acoustical Society of America.

96. Lighthill,M.J. On Sound Generated Aerodynamically: Part I: General Theory. *Royal Society -- Proceedings Series A* **211**, 564-587 (1952).

97. Lighthill,M.J. On Sound Generated Aerodynamically: Part II: Turbulence as a source of sound. *Royal Society -- Proceedings Series A* **222**, 1-32 (1954).

98. Westervelt,P.J. Absorption of sound by sound. *J. Acoust. Soc. Am.* **59**, 760-764 (1976).

99. Berktay,H.O. Parametric amplification by the use of acoustic non-linearities and some possible applications. *Journal of Sound and Vibration* **2**, 462-470 (1965).

100. Berktay,H.O. & Al Temimi,C.A. Virtual arrays for underwater reception. *Journal of Sound and Vibration* **9**, 295-307 (1969).

101. Al Temimi,C.A. Interaction between two sound fields propagating in different directions. *Journal of Sound and Vibration* **8**, 44-63 (1968).

102. Westervelt,P.J. Scattering of sound by sound. 301-305. 1990. Austin, TX, USA, Elsevier Applied Science. Frontiers of Nonlinear Acoustics. 12th ISNA.

103. Kuznetsov,V.P. Equations of nonlinear acoustics. Soviet Physical Acoustics 16, 467-470. 1971.

104. Zabolotskaya,E.A. & Khokhlov,R.V. Quasi-plane waves in the nonlinear acoustics of confined beams. Soviet Physical Acoustics 15, 35-40. 1969.

105. Garrett,G.S., Tjotta,J.N., Rolleigh,R.L. & Tjotta,S. Reflection of parametric radiation from a finite planar target. *Journal of the Acoustical Society of America* **75**, 1462-1472 (1984).

106. Pompei,F.J. The use of airborne ultrasonics for generating audible sound beams. *Journal of the Audio Engineering Society* **47**, 726-731 (1999).

107. Woodsum,H.C. A General Theory for the Scattering of Sound by Sound with Parametric Array Applications. Brown University. Doctoral Thesis . 1979.

108. Woodsum,H.C. & Westervelt,P.J. Non-contributive virtual sound sources. *Journal of Sound and Vibration* **66**, 9-11 (1979).

109. Hennion,P.Y. & Alais,P. A study of the parametric radiation of focusing transducers [acoustics]. *Revue du Cethedec* **15**, 17-22 (1978).

110. Alais,P. & Hennion,P.Y. A Fourier theory of the nonlinear interaction of acoustical beams in absorbing fluid. The special case of parametric emission. *Acustica. (Germany. )* **43**, 1-11 (1979).

111. Alais,P., Hennion,P.Y. & La Greve,M. Fourier analysis of nonlinear parametric acoustics. *Revue du Cethedec* **15**, 9-16 (1978).

112. Korpel,A. Acouto-optics. Academic Press, New York (1972).

113. Ludwig,A.C. & Wong,W.C. The Handbook of Antenna Design. Rudge,A.W. (ed.)1982).

114. Westervelt,P.J. Scattering of sound by sound. *Acoustical Society of America -- Journal* **29**, (1957).

115. Truchard,J.J. Parametric receiving array and the scattering of sound by sound. *J. Acoust. Soc. Am.* **64**, 280-285 (1978).

116. Korman,M.S. & Beyer,R.T. SCATTERING OF SOUND BY TURBULENCE IN WATER. **67**, 1980-1987 (1980).

117. Westervelt,P.J. Recent advances in the theory of the nonscattering of sound by sound. 117-120. 1984. Kobe, Japan, Osaka Univ. Proceedings of the 10th International Symposium on Nonlinear Acoustics.

118. Fatemi,M. & Greenleaf,J.F. Probing the dynamics of tissue at low frequencies with the radiation force of ultrasound. *Phys. Med. Biol.* **45**, 1449-1464 (2000).

119. Chen,S., Fatemi,M. & Greenleaf,J.F. Remote measurement of material properties from radiation force induced vibration of an embedded sphere. *J. Acoust. Soc. Am.* **112** , 884-889 (2002).

120. Alizad,A. *et al.* Detection of calcium deposits on heart valve leaflets by vibro-acoustography: an in vitro study. *J. Am. Soc. Echocardiogr.* **15**, 1391-1395 (2002).

121. Zhang,X.M., Fatemi,M., Kinnick,R.R. & Greenleaf,J.F. Noncontact ultrasound stimulated optical vibrometry study of coupled vibration of arterial tubes in fluids. *J. Acoust. Soc. Am.* **113**, 1249-1257 (2003).

122. Karjalainen,T., Thierman,J.S. & Hynynen,K. Ultrasound acoustic stimulated emission for controlling thermal surgery. 2, 1397-1400. 1999. Caesars Tahoe, NV, USA, Institute of Electrical and Electronics Engineers Inc., Piscataway, NJ, USA. Proceedings of the IEEE Ultrasonics Symposium.

123. Frisk,G.V. Ocean and Seabed Acoustics: A Theory of Wave Propagation. Prentice Hall, N.J. (1994).

124. Stratton,J.A. Electromagnetic Theory. McGraw-Hill Book Company, Inc., New York (1941).

125. Makris,N.C. Notes on Scattering from Stratified Medium and Spherical Reflector. 6-22-2003. Personal Communication.

126. Fatemi,M., Wold,L.E., Alizad,A. & Greenleaf,J.F. Vibro-acoustic tissue mammography. *IEEE Trans. Med. Imaging* **21**, 1-8 (2002).

127. Kino,G.S. Acoustic Waves: Devices, Imaging, and Analog Signal Processing. Prentice-Hall, Inc., Englewood Cliffs, NJ (1987).

128. Kinsler,L.E. & Fry,A.R. Fundamentals of Acoustics. 1982. New York, John Wiley and Sons.

129. Leighton,T.G. The Acoustic Bubble. Academic Press, London (1994).

130. Duck,F.A., Baker,A.C. & Starritt,H.C. Ultrasound in Medicine. Institute of Physics Publishing, Philadelphia (1998).

131. Brekhovskikh,L.M. & Lysanov,Yu.P. Fundamentals of Ocean Acoustics. 1990. New York, Springer-Verlag.

132. Clement,G.T. & Hynynen,K. Field characterization of therapeutic ultrasound phased arrays through forward and backward planar projection. *J. Acoust. Soc. Am.* **108**, 441-446 (2000).

133. Hein,I.A. & O'Brien,W.D., Jr. Current time-domain methods for assessing tissue motion by analysis from reflected ultrasound echoes-a review. *IEEE Trans. Ultrason. Ferroelectr. Freq. Contr.* **40**, 84-102 (1993).

134. McNamara,F.L. & Beyer,R.T. Variation of radiation pressure method of measuring sound absorption in liquids. *Acoustical Society of America -- Journal* **25**, 259-262 (1953).

135. Sokka,S.D., King,R. & Hynynen,K. MRI-guided gas bubble enchanced ultrasound heating in *in vivo* rabbit thigh. *Phys. Med. Biol.* **48**, 223-241 (2003).

136. Holt,R.G. & Roy,R.A. Measurements of bubble-enhanced heating from focused, MHz-frequency ultrasound in a tissue-mimicking material. *Ultrasound. Med. Biol.* **27**, 1399-1412 (2001).

137. Jones,J.P. 1970. Brown University, Doctorate Thesis.

138. Konofagou,E., Thierman,J. & Hynynen,K. A focused ultrasound method for simultaneous diagnostic and therapeutic applications--a simulation study. *Phys Med. Biol.* **46** , 2967-2984 (2001).

139. Ward,J.P. Solid Mechanics: an introduction. Kluwer Academic Publishers, (1992).

140. Shigao,C., Fatemi,M., Kinnick,R. & Greenleaf,J.F. Comparison of stress field forming methods for vibro-acoustography. *IEEE Trans. Ultrason. Ferroelectr. Freq. Contr.* **51**, 313-321 (2004).

141. Karshner,G.B. Direct method for measuring the speed of sound. *American Journal of Physics* **57**, 920-922 (1989).

142. Beyer,R.T. & Jones,J.P. Seventh International Congress on Acoustics. 629. 1971. Budapest.